Resolution improvement and pattern generator development for the Maskless Micro-ion-beam Reduction Lithography system

by

Ximan Jiang

B.S. (University of Science & Technology of China) 1998
M.S. (University of Science & Technology of China) 2001

A dissertation submitted in partial satisfaction of the

Requirements for the degree of

Doctor of Philosophy

in

Engineering-Nuclear Engineering

in the

GRADUATE DIVISION

of the

UNIVERSITY of CALIFORNIA, BERKELEY

Committee in charge:

Professor Ka-Ngo Leung, Chair
Professor Tsu-Jae King
Professor Edward C. Morse

2006

The dissertation of Ximan Jiang is approved:

_____

Chair Date

_____

Date

_____

Date

University of California, Berkeley

Spring 2006

Abstract

Resolution improvement and pattern generator development for the Maskless Micro-ion-beam Reduction Lithography system

by

Ximan Jiang

Doctor of Philosophy in Nuclear Engineering

University of California, Berkeley

Professor Ka-Ngo Leung, Chair

The shrinking of IC devices has followed the Moore's Law for over three decades, which states that the density of transistors on integrated circuits will double about every two years. This great achievement is obtained via continuous advance in lithography technology. With the adoption of complicated resolution enhancement technologies, such as the phase shifting mask (PSM), the optical proximity correction (OPC), optical lithography with wavelength of 193 nm has enabled 45 nm printing by immersion method. However, this achievement comes together with the skyrocketing cost of masks, which makes the production of low volume application-specific IC (ASIC) impractical.

In order to provide an economical lithography approach for low to medium volume advanced IC fabrication, a maskless ion beam lithography method, called Maskless Micro-ion-beam Reduction Lithography (MMRL), has been developed in the Lawrence Berkeley National Laboratory. The development of the prototype MMRL

system has been described by Dr. Vinh Van Ngo in his Ph.D. thesis. But the resolution realized on the prototype MMRL system was far from the design expectation.

In order to improve the resolution of the MMRL system, the ion optical system has been investigated. By integrating a field-free limiting aperture into the optical column, reducing the electromagnetic interference and cleaning the RF plasma, the resolution has been improved to around 50 nm. Computational analysis indicates that the MMRL system can be operated with an exposure field size of 0.25 mm and a beam half angle of 1.0 mrad on the wafer plane. Ion-ion interactions have been studied with a two-particle physics model. The results are in excellent agreement with those published by the other research groups. The charge-interaction analysis of MMRL shows that the ion-ion interactions must be reduced in order to obtain a throughput higher than 10 wafers per hour on 300-mm wafers. In addition, two different maskless lithography strategies have been studied. The dependence of the throughput with the exposure field size and the speed of the mechanical stage has been investigated.

In order to perform maskless lithography, different micro-fabricated pattern generators have been developed for the MMRL system. Ion beamlet switching has been successfully demonstrated on the MMRL system. A positive bias voltage around 10 volts is sufficient to switch off the ion current on the micro-fabricated pattern generators. Some unexpected problems, such as the high-energy secondary electron radiations, have been discovered during the experimental investigation. Thermal and structural analysis indicates that the aperture displacement error induced by thermal expansion can satisfy

the 3δ CD requirement for lithography nodes down to 25 nm. The cross-talking effect near the surface and inside the apertures of the pattern generator has been simulated in a 3-D ray-tracing code. New pattern generator design has been proposed to reduce the cross-talking effect. In order to eliminate the surface charging effect caused by the secondary electrons, a new beam-switching scheme in which the switching electrodes are immersed in the plasma has been demonstrated on a mechanically fabricated pattern generator.

Professor Ka-Ngo Leung

Nuclear Engineering Department

University of California, Berkeley

Table of Contents

List of figures

ACKNOWLEDGEMENTS

I want to thank all the people who helped me through all the years. In particular, I want to thank my parents, my uncle, my brothers and sister for the constant support and guidance to my life and my study.

To Professor Ka-Ngo Leung, thanks for giving me the opportunity to work on this project, thanks you for all the guidance and teachings. The five years of study under your instructions will be the basis of my future career.

To Professor Tsu-Jae King and Professor Edward Morse, thanks for accepting to read my dissertation and teaching me the knowledge on IC devices and plasma physics.

To Professor Donald Olander for presiding my Ph.D. qualifying exam as the chair of the committee.

To Dr. Qing Ji, thanks to your encouragement, advice and help during my five years of study in US. Thank you for referring me to Professor Leung so that I got the opportunity of studying in UC Berkeley and working in the Plasma and Ion Source Technology at the Lawrence Berkeley National Laboratory.

To Dr. Vinh Van Ngo for teaching me to operate the MMRL system.

I would like to thank Steve Wilde, Tom McVeigh, Paul Wong, Frederic Gicquel and Jerry Fischer for the help on mechanical or electrical design and machining.

To Michael King, thanks for your friendship and thank you for helping me correct the grammar and wording problems in my dissertation.

Thanks to Lili Ji, Ye Chen, Tak Pui Lou, Ying Wu and all the other members of the Plasma and Ion Source Technology Group at the Lawrence Berkeley National Laboratory for the friendship and the help on the experiments.

I also want to thank all the former undergraduate student assistants, Audrey Chang, Bret van den Akker, Dustin Li and Eric Wendel for helping me to do some simulations and writing the Labview control program.

I would like to thank Lisa Zemelman for the instructions and the help to the studying in the Nuclear Engineering Department.

To the members of the Ion Beam Technology Program, the head of the program, Rick Gough, and the administrative coordinators, Darlene Hawkins, Martha Condon and Parish Epps.

I would like to acknowledge the Microfabrication Laboratory at UC-Berkeley and the National Center for Electron Microscopy (NCEM) at the Lawrence Berkeley National Laboratory for providing the facilities to fabricate the pattern generator for my thesis project.

I also would like to acknowledge the support from the Defense Advanced Research Projects Agency (DARPA) and the US Department of Energy through the Lawrence Berkeley National Laboratory under Contract No. DE-AC02-05CH11231.

Chapter 1

Introduction

1.1 Background

Moore's law has continued to push for higher integrated circuit (IC) device densities and lower manufacturing costs. Lithography technology has been the driving force for IC scaling. Conventional optical lithography, based on refractive optics, has enabled sub 65 nm half-pitch technology nodes patterning by using shorter photon wavelengths and complicated resolution enhancement technology (RET), such as off axis illumination (OAI), complementary double exposure (CODE), phase shifting mask (PSM) and optical proximity correction (OPC). Immersion lithography may further extend the limit of conventional optical lithography to 40 nm nodes.

Conventional optical lithography needs to continuously shorten the wavelength of incident light in order to keep printing smaller feature sizes. Up to now, 193 nm deep ultraviolet (DUV) has already been used by the industry. Unfortunately, when the DUV wavelength is further reduced to 157 nm, the interactions of the photons with the conventional lens and mask materials introduce a hurdle to its viable application. Calcium fluoride (CaF_2), one of the only materials that is relatively transparent to 157 nm DUV light, is the major lens material employed for the refractive optics column in conventional optical lithography. But calcium fluoride has intrinsic birefringence and

process-induced birefringence to DUV light, which will diffract photons differently depending on its polarization. The reduction of intrinsic birefringence and process-induced birefringence will greatly increase the cost of the lenses to the point of impracticality.[1] In addition, the current mask blank material (fused silica) and resist are not transparent enough for 157 nm photons.[2] Due to these challenges, diffractive-optics-based conventional optical lithography might eventually be abandoned.

Several next generation lithography (NGL) approaches are being investigated, such as Extreme UltraViolet Lithography (EUVL), electron beam projection lithography (EPL) and ion beam projection lithography (IPL). All the previously mentioned NGLs require expensive masks in order to be successfully implemented. For example, EUVL needs to use defect-free mask blanks, which consist of multilayer molybdenum/silicon coatings. The yield of defect-free mask blanks during ion sputter deposition is currently too low and inefficient for commercial suitability. Membrane masks and stencil masks have been developed for electron projection lithography. Both types are very thin which makes them fragile and difficult to handle. Ion beam projection lithography also uses stencil masks. For a stencil mask, complementary exposures are required to print the designs with isolated unexposed features, such as donut shape,[3] which makes the process even more complicated and costly.

For traditional optical lithography, the implementation of resolution enhancement technologies has significantly increased the cost of the mask. This prohibitively high nonrecurring cost makes the fabrication of low-volume application specific IC (ASIC) unrealistic. In order to eliminate the mask cost for medium to low volume production, maskless lithography techniques, which are also called ML2, are being developed by the

industry. Similar to the next generation projection lithography tools, maskless lithography technologies can also be divided into two major categories, optical maskless lithography (O-ML2) and charged particle maskless lithography (CP-ML2). The following sections will briefly introduce these NGLs and ML2.

1.2 Traditional optical projection lithography

In traditional optical lithography tools, diffractive optic columns are used to image masks onto wafers (fig. 1.1). Unlike charged particle optics, diffractive light optical lenses have a well-defined boundary for each lens element, which makes it much easier to fabricate a light optics column with most aberrations corrected. Consequently, the resolution of the conventional optical lithography system is limited by the diffractive nature of photons.

Figure 1.1. ASML stepper (image courtesy of ASML.)

Based on Rayleigh's Criterion, the resolution determined by diffraction is governed by equation (1.1) when K_1 equals to 0.61. The depth of focus is given by equation (1.2). The most obvious method to improve resolution is to decrease the wavelength λ. The illumination light source has evolved from the mercury lamp 436 nm G-line and 365 nm I-line to 248 nm KrF and 193 nm ArF excimer laser. Further decreasing the wavelength to 157 nm F_2 laser has encountered obstacles in the development of lens, mask blank and photo resist. Increasing the numerical aperture (NA) of the lens can also improve the resolution. However, these two methods will decrease the depth of focus (DOF).

$$\text{Resolution} = K_1 \frac{\lambda}{n \cdot Sin(\theta)} = K_1 \frac{\lambda}{n \cdot NA} \tag{1-1}$$

$$\text{Depth of focus} = \frac{K_2}{2} \frac{\lambda}{n \cdot (1 - Cos(\theta))} = K_2 \frac{\lambda}{n \cdot NA^2} \tag{1-2}$$

Several resolution enhancement techniques (RET) have been developed to improve the printing resolution without decreasing the wavelength. Usually only the zeroth order plus positive and negative first diffraction orders will pass through the lens in high resolution optical steppers. Off-Axis Illumination (OAI) technique tilts the illumination ray away from the normal incidence so that only the zeroth plus positive or negative first diffraction orders pass through the lens. A phase shifting mask (PSM) also works in a similar way. An alternating PSM uses alternative 180 degree phase-shifting features to completely eliminate the zeroth order through destructive diffraction.[4] PSM and OAI techniques allow the diffraction patterns of the high spatial frequency features to pass though the lens so that the resolution and the DOF can both be improved. Optical proximity correction (OPC) technique creates sub-resolution assisting features (SRAF)

around the primary patterns on the mask to generate desired aerial images with sub-wavelength scale in photoresist.[5] Besides the RETs, another trick to extend the life of the conventional optical lithography is the immersion technique. Immersion lithography uses the high refractive index liquid under the projection lens to allow light to arrive at wafers with an even higher angle, which will be internally reflected in dry lens. In the meantime, immersion lithography allows a slower loss of DOF as resolution is improved.[6]

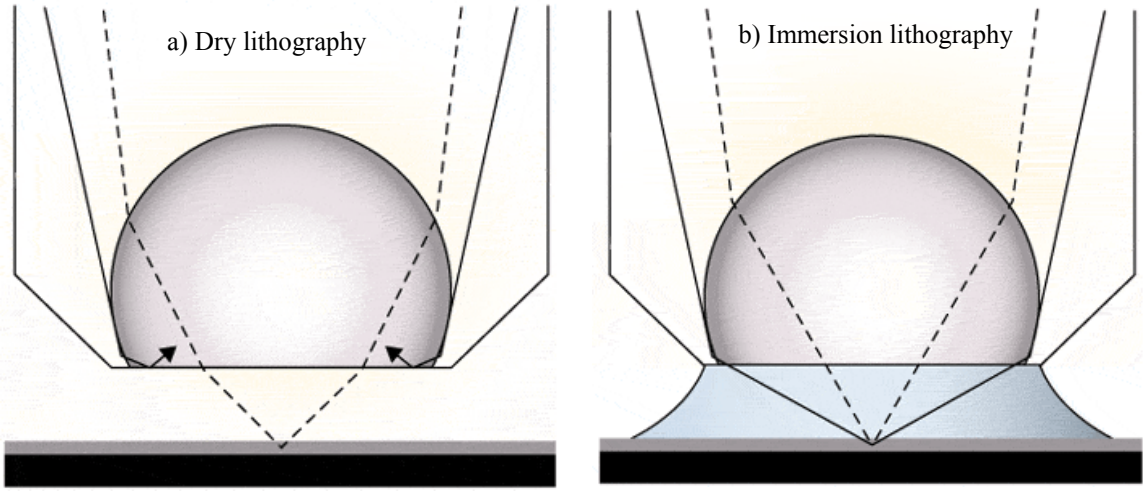

Figure 1.2. The comparison of dry lithography and immersion lithography. Immersion lithography can improve the resolution (solid lines) or increase the DOF while maintaining the resolution (dashed lines).[6]

Even though the resolution enhancement techniques and the immersion lithography can extend the employment of 193 nm DUV down to 45 nm node, it is still inevitable to employ shorter wavelengths to print even smaller features, which might eventually cause the refractive optics based lithography to be abandoned. In addition, the employment of phase-shifting design and OPC features greatly increase the nonrecurring cost on mask fabrication. All these factors ferment the development of the next generation lithography (NGL) and the maskless lithography (ML2).

1.3 Next generation lithography techniques

The diffraction of light limits the resolution capability of the conventional optical lithography stepper. Decreasing the wavelength will enable the printing of even smaller features. But conventional masks and lens materials may not be transparent enough for high-energy photons. This drawback forces optical lithographers to take a large leap by decreasing the wavelength from 193 nm or 157 nm DUV to 13.4 nm (EUV) and adopting the reflective optics design. In the meantime, charged particles regain the favor in the race because they have much smaller wavelengths than photons. IBM already proved the feasibility of electron beam lithography in 1970s.[7] With the decrease of feature size, the exposure time of single beam direct-write systems is too long to economically adopt it for high volume production. Charged particle projection lithography systems, electron/ion beam projection lithography, were and are being developed to overcome the throughput issue of the single beam direct write system. These next generation lithography techniques will be introduced in the following sections.

1.3.1 Extreme Ultraviolet Lithography (EUVL)

EUV lithography, which shares many common aspects with traditional optical lithography, has been considered as the most likely next generation lithography technique to move beyond 193 nm or 157 nm immersion lithography. The origin of EUV lithography can be established in the work of A. M. Hawryluk and L.G. Seppala in 1988.[8] They proposed that optical projection lithography with 13 nm photons could be realized

by using mirrors with high reflectivity for soft x-rays. Since 13 nm EUV is not transmitted by any optical materials, EUV mask and optical lens must be entirely reflective, as shown in fig. 1.3.[9] In order to reduce the absorption by air, EUV system has to work in a vacuum environment as a charged particle lithography technique. The most challenging issues for EUV lithography are the development of the low defect density, ultra-flat EUV mask blanks and an over 100 W EUV light source.[10]

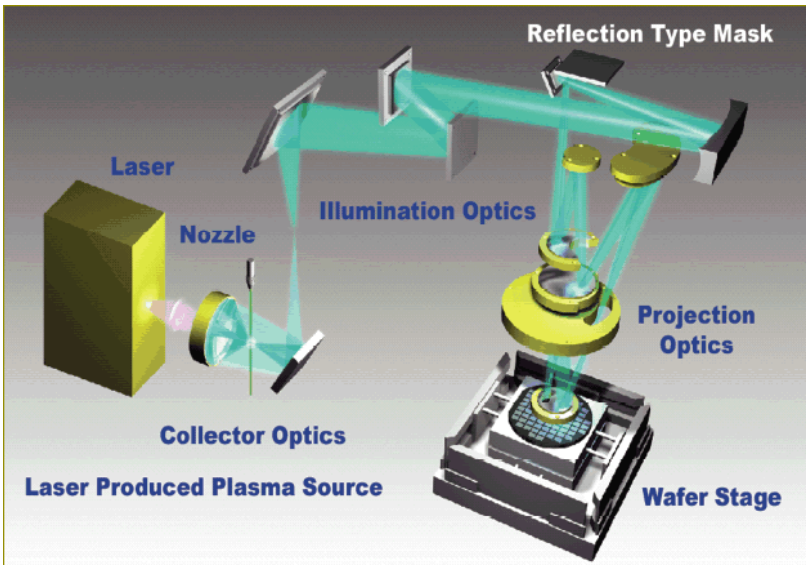

Figure 1.3. The optical layout of an EUV exposure system with laser produced plasma (LPP) source.[9]

The structure of an EUV mask is shown in fig. 1.4.[11] The multi-layer Mo/Si coating reflects EUV light with a peak reflectivity of 65%. The reflectivity needs further improvement because the EUV light is reflected more than 9 times. The defect-sensitive area on EUV mask should not have any defects larger than 50 nm. Because of much

shorter wavelengths, EUV can print a much smaller feature without using complicated phase shifting masks and optical proximity correction features, which may potentially reduce the cost of the mask if the defect-free mask fabrication and handling techniques can be realized at a reasonable cost.

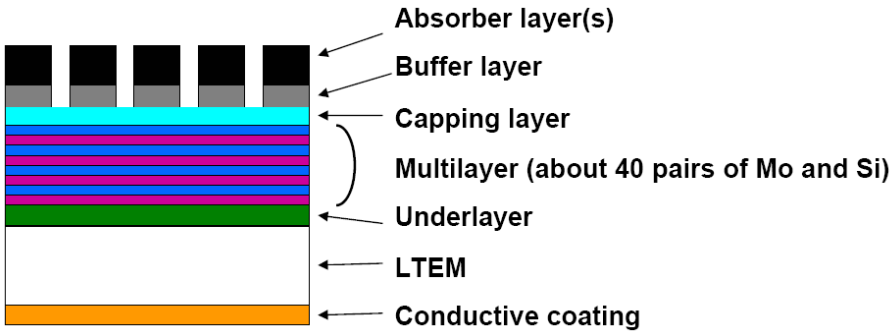

Figure 1.4. Structure of the EUV mask.[11]

EUV laser can be produced either by discharged-produced plasma (DPP) or laser-produced plasma (LPP). EUV sources based on Xe, Sn and Li have been proposed. The remaining challenging issues are continuous improvement of the in-band EUV output power to over 100 watt, mitigation of the debris from the plasma generation materials and plasma erosion to the source body and coating. The initial cost of an LPP EUV source might be as high as 10 to 30 million.[12] Considering the cost of the other critical components on EUV lithography, the cost of ownership for EUVL will be much more expensive than the traditional optical lithography.

1.3.2 Electron Projection Lithography (EPL)

Great advancement in electron beam lithography can be dated back to the 1960s. The early electron beam direct-write lithography machines used a single Gaussian round beam to write one pixel at a time, and are still operated in many research institutes. Later on, IBM adopted shaped beam approach to increase throughput. These systems can expose several hundred pixels per shot. The throughput of the early shaped beam systems was acceptable in the 1980s because of the low device density in the early integrated circuits. By the late 1980s, IBM had installed more than 30 variable-shaped beam systems (EL-3) for its bipolar logic chip design. With the transition from bipolar to CMOS devices and the increasingly higher integration density, the throughput of the early direct-write systems couldn't keep up with the pace of Moore's law,[13,14] which led to the abandonment of the early electron beam maskless lithography from the commercial production line.

Electron beam lithography must adopt more parallel exposure design to meet the requirement on throughput. The two major disadvantages in charged particle lithography that directly limit its throughput are the high off-axis aberration coefficients in charged particle optics and the particle-particle interactions in high current density conditions. Optical lithography can achieve higher throughput because of the following intrinsic characteristics. Light optical lenses can attain full-field (more than 2 cm) exposures, which represents higher parallelism. Another benefit of using photons is that they won't attract or repel each other, which indicates that light flux density can be more scalable than charge particle current density. In order to improve the throughput for charged particle lithography, these issues must be resolved.

The advantages of the charged particle lithography include being diffraction-less and having a larger process window for a higher DOF and resolution capability. With the decrease of feature size, traditional optical lithography has suffered from a continuously shrinking process window and increasingly higher mask cost. As a result, electron projection lithography (EPL) was investigated by IBM with its PREVAIL system and Lucent Technologies with its SCALPEL system as potentially high throughput and high resolution next generation charged particle lithography techniques.

Both systems use telecentric antisymmetric doublets (TADs) design, which has inherently low off-axis shaped-beam aberrations and distortion (as shown in fig. 1.5).[14,15] Consequently, exposure sub-field can be as large as 0.25 mm in both systems. The demagnification ratios are both 4:1. Stencil masks or membrane masks can be used on the PREVAIL system. But the masks need to be divided into 1.0-mm square subfields. Full-field exposure requires beam deflection to illuminate different subfields on the mask and stitching of the demagnified subfields on the wafers. The key feature of PREVAIL is the variable axis lens (VAL). The "Virtual axis" of the VAL is changed electronically to coincide with the deflected electron beams to obtain low off-axis aberrations and distortions. Sub-field resolution and shape integrity can be maintained over a large scanning range by the use of this technique.[14] On the other hand, the SCAPEL system illuminates a stationary 1.0×1.0 mm^2 on-axis mask field. The mask is divided into stripes, which are then moved into the 1.0×1.0 mm^2 on-axis illuminated field with a constant speed. In the mean time, the wafer is scanned with a quarter of the mask speed to synchronize with the mask images.

The key characteristic of SCAPEL is the scattering mask. This scattering mask also acts as a membrane mask. The supporting membrane is made of low atomic number materials, which are virtually transparent to electron beams with energy over 100 keV. But the "dark regions" (patterned scattering layer) on the mask are made of materials with high atomic number, which can scatter the electron beams into a cone of several miliradians. Most of the scattered electrons will be blocked by the downstream contrast aperture. Scattering masks can print donut shapes with a single exposure. Since electrons transmit through the mask with very little energy loss, the heating of the mask at high illumination current is minimized.

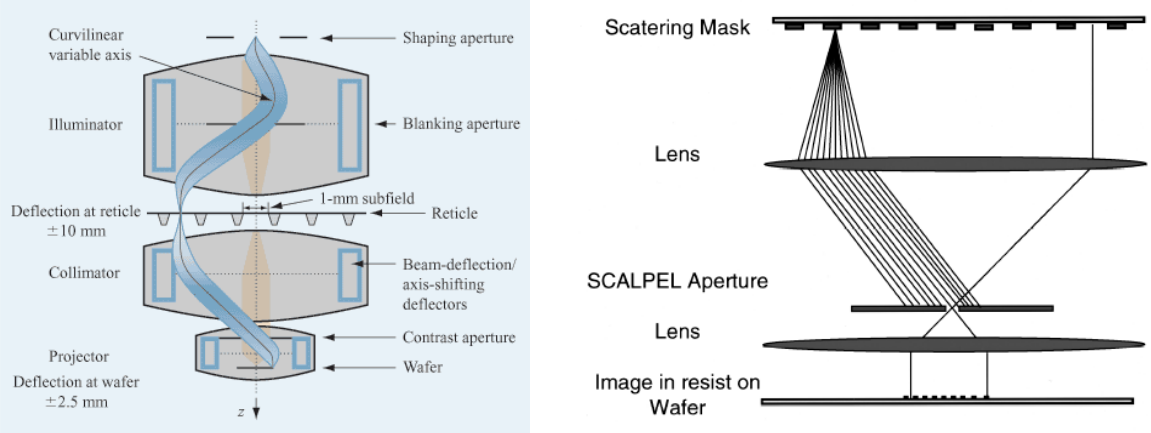

Figure 1.5. Conceptual optics layout for PREVAIL (left side) and SCAPEL (right side). [14,19]

The EPL technology developed at IBM has been transferred to Nikon. The EPL technique might be employed first on contact, via holes and gate layers printing. A throughput of 4 wafer-per-hour (WPH) on 300 mm wafer has been achieved on the NSR-

EB1A system. Further improvement on throughput is possible by increasing the sub-field size (fig. 1.6).[16]

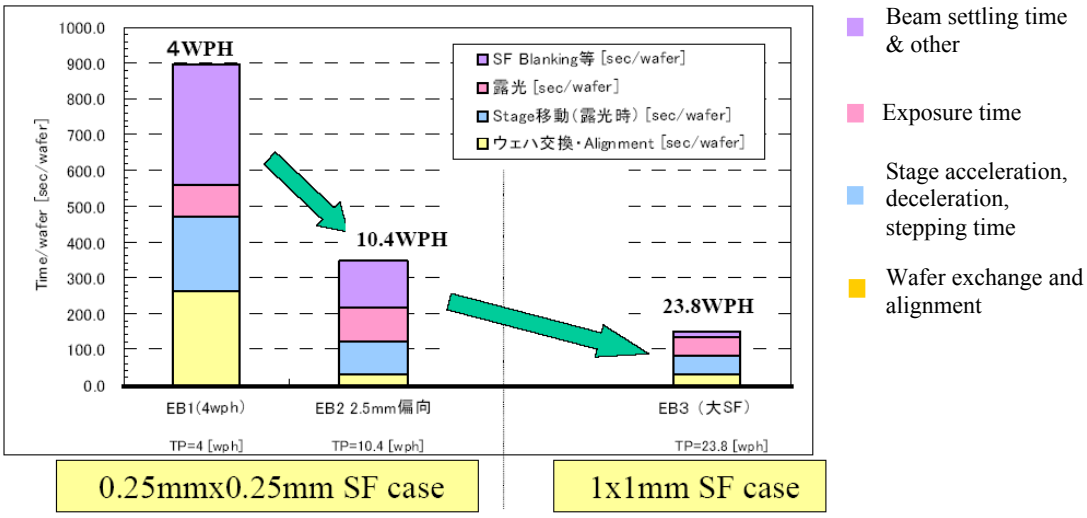

Figure 1.6. Throughput evolution on Nikon EPL tool with new concept electron optics. [16]

1.3.3 Ion projection lithography

Ion projection lithography (IPL) shares many common characteristics with EPL. Due to the large mass to charge ratio, magnetic lenses are usually not suitable to focus ion beams. Therefore, electrostatic lenses are used to accelerate and focus ion beams. An electrostatic optics column for IPL has the potential of obtaining a larger field size than EPL. An exposure field of 12.5 mm has been proposed for the IPL process development tool (PDT) developed by IMS in Vienna of Austria.[17] From the result shown in fig. 1.6, a large exposure field size will greatly reduce the stage moving and beam settling time,

which may help IPL to obtain a higher throughput. An IPL system with a point ion source is shown in fig. 1.7. A filament-driven plasma ion source with an energy spread of 1 eV FWHM, developed by the Plasma and Ion Source Technology Group of the Lawrence Berkeley National Laboratory (LBNL), has reduced the chromatic aberrations of the system.[18] The virtual source with diameter of 10 μm gives a numerical aperture of 10^{-5}, which can greatly increase the depth of focus and reduce the geometrical aberrations. Hydrogen and helium ions have been used on IPL systems because of their low mass and high penetration depth in the resist. Conventional IPL systems also require a stencil mask. The ion beam energy at the mask plane is higher than 10 keV in the traditional IPL system, which may cause possible mask damage.

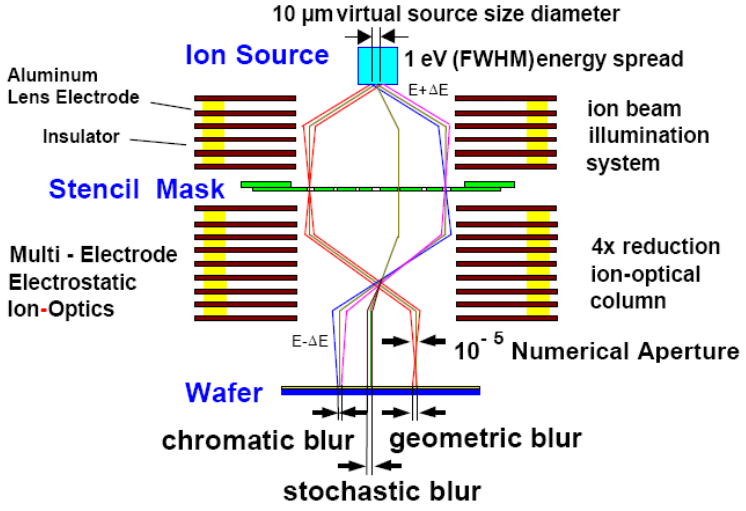

Figure 1.7. Ion projection lithography with a point ion source and beam illumination column built in Vienna Austria.[17]

1.3.4 Nanoimprint Lithography

Nanoimprint lithography (NIL) is an unconventional nanofabrication technique. It has recently been considered as a possible substitutive nanofabrication technique, even

though the traditional embossing imprint technique has been widely used for features larger than several hundreds of microns. The reason for the expectation of NIL for nano-scale range might be the expected high cost of ownership of the NGLs based on projection optics. A number of nanoimprint processes have been developed.[19] All of these processes require a rigid pre-patterned stamp, a soft polymer layer and a flat substrate. The Step and Flash Imprint Lithography (S-FIL™) technique developed at the University of Texas at Austin has been commercialized through Molecular Imprints Inc. The process flow of the S-FIL™ technique is shown in fig. 1.8.

The company Nanonex has achieved line widths as small as 5 nm with pitch of 12 nm through NIL technique. Nanoimprint lithography has entered the International Technology Roadmap for Semiconductors (ITRS) for possible inclusion at 32 nm nodes.[20] Yet, it is still too soon to say whether or not NIL will be used for high volume IC fabrication. But this technique offers a very attractive low cost solution to printing features below 50 nm compared with the NGLs based on reduction projection optics.

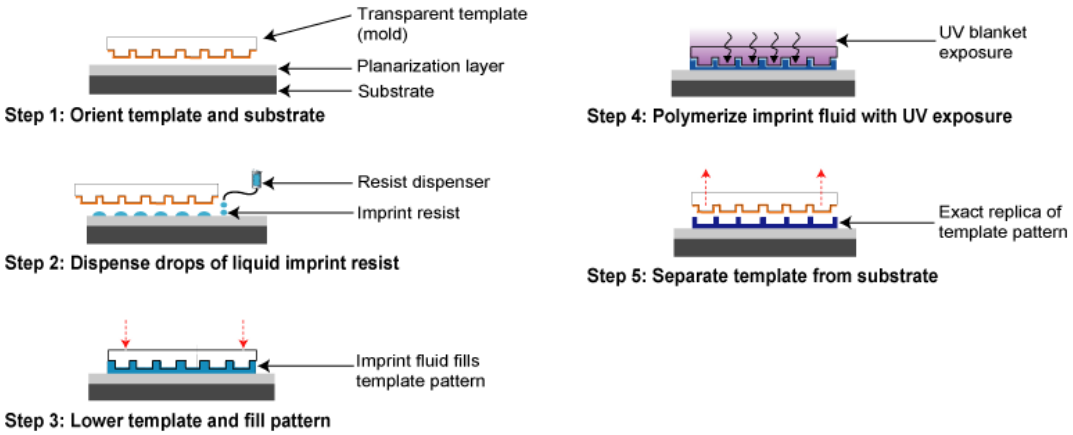

Figure 1.8. Process flow of S-FIL™ technique. (Image courtesy of Molecular Imprints Inc.)

1.4. Maskless lithography

Phase shifting mask (PSM) and optical proximity correction (OPC) have enabled the traditional optical lithography to print features below the limit set by the Rayleigh's Criterion. But this benefit comes with detrimental aspects like the increasingly complex mask design and the skyrocketing mask cost. The cost of a high-end optical mask set for the 90 nm node has exceeded $1.5 million mark. And it may reach $3 to $4 million for 65 nm technology.[21] Regardless of the uncertain future for the next generation lithography (NGL) techniques, the fabrication cost of the masks for all the NGLs could be higher than the traditional binary chrome mask. Masks will be unaffordable for low to medium volume advanced ASIC fabrication. The mask usage data from a commercial foundry is presented in fig. 1.9.[22] 50% of the total masks were only used on 1% of the wafers. And 5% of the wafers used 80% of the masks. Complex mask design also increases the prototype cycle time. Combined with the extremely high prototype cost induced by the mask, it may indirectly halt some of the possible technical innovations in the IC business before the new market is fostered to a level for high volume production. Various maskless lithography (also called ML2) approaches are being developed to offer an economical solution with quicker turnaround time for low to medium volume ASIC fabrication and prototyping. For less than 600~700 wafers per masks, maskless lithography can have lower cost of ownership than mask-based lithography according to the insert picture in fig. 1.9.

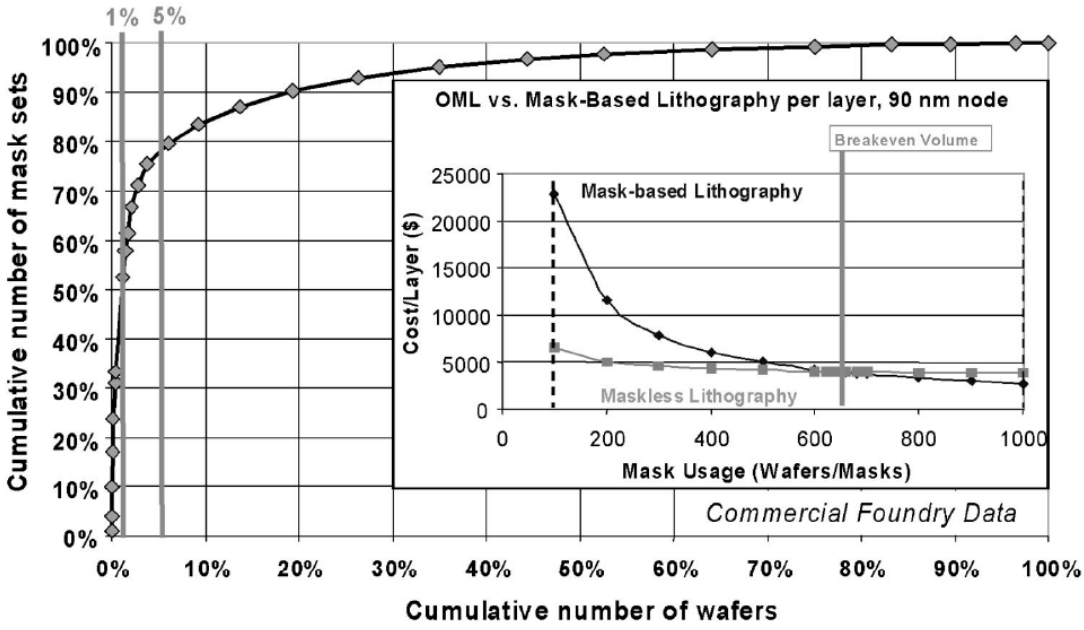

Figure 1.9. Mask usage data from a commercial foundry. Inset shows the estimated cost per layer versus mask usage for maskless lithography and masked lithography.[22]

Maskless lithography has coexisted with the masked lithography for decades. Limited by low throughput, its application was confined mainly to mask manufacturing. Corresponding to the developing NGLs, ML2s can also be categorized into optical systems and charged particle systems. Current laser mask writers offer higher throughput but lower resolution than e-beam mask writers.[23] Many innovative techniques have been proposed to improve the throughput of maskless lithography, so that it can be directly used for advanced IC fabrication and totally eliminate the nonrecurring mask cost. Some of the ML2 technologies for high-end IC fabrication will be briefly introduced in the following sections.

1.4.1 Optical maskless lithography

Optical maskless lithography systems use similar optics column as mask-based projection optical lithography. The key technology is to develop spatial light modulators (SLM) for pattern generation. SLMs based on mirror and zone plate array have been proposed. A mirror based SLM for high end maskless lithography, proposed by Micronic Laser Systems AB (Taby, Sweden) in cooperation with ASML, is based on the extension of their 1-Mpixel micro-mirror SLM technology, which is currently used in Micronic's Sigma mask writers. Fig. 1.10 illustrates the principle of an optical maskless lithography tool with a mirror based SLM. In order to improve the throughput, multiple SLMs may be used in parallel. The pixels from different SLM are stitched together to construct a desired image on the wafers. The loading of the image data into SLMs is synchronized with the motion of the stage and the pulsing of the laser.[22]

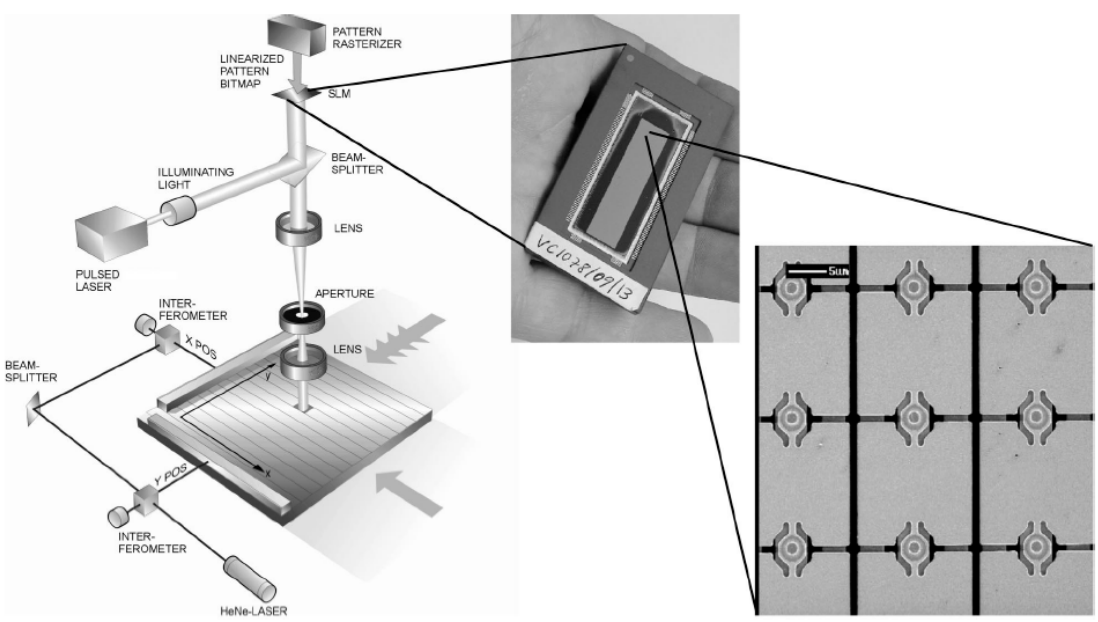

Figure 1.10 Schematic of an optical maskless lithography tool with mirror-based SLM. Two inserts show the SLM chip used in Micronic's Sigma mask writer, which 512x2048 pixels. The size of a single mirror is 16×16 μm^2.[22]

The operation principle of the mirror based SLM is described in fig. 1.11. The pixel size on SLM for optical maskless lithography is 8×8 μm^2. Each pixel cell has a storage capacitor, which can be charged to an analog voltage. The induced electrostatic force can tilt the mirror to different angles, which depend on the voltage on the capacitors and the stiffness of the hinge. A flat mirror surface will act as a clear area on a corresponding mask. A fully tilted mirror will reflect the light outside the stop in the projection optics. The intermediate tilt angles will partially allow the light to be transmitted onto the wafer. Thus, gray-level exposure can be generated by controlling the analog voltage charged on the capacitors. Gray level printing and mirror-tilting with alternative directions between rows is very helpful for CD/overlay control through complicated algorithms, as was discussed in more detail in Hans Martinsson's paper. [22]

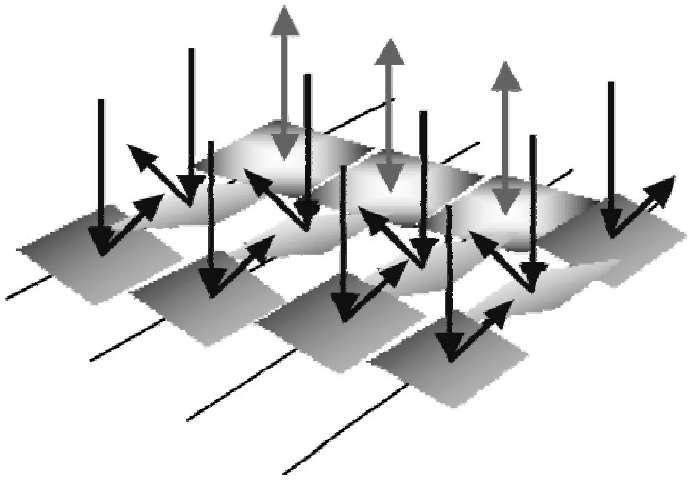

Figure 1.11. Grayscale printing and alternating tilt directions between rows.[22]

Zone plate modulator (ZPM) for pattern generation has been proposed by ZPInnovation Inc. A zone plate modulator consists of a pair of complementary reflective zone plates. When the distance between the two zone plates is $d=1/2m\lambda$, the ZPM acts as a mirror. The illumination light will be reflected back. When $d=(1/2m\pm1/4)\ \lambda$, the ZPM

will diffract the incoming light to form a focal point, as shown in fig. 1.12. By assembling an array of ZPMs together (fig. 1.13), a controllable array of light spot can be generated.[24] Several other optical maskless lithography designs based on the diffraction from 1-D or 2-D SLMs have also been reported in reference 27. [25]

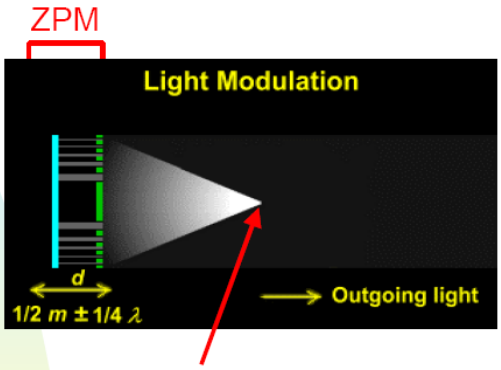

Figure 1.12. ZPM can focus the illumination light to a diffraction limited point spot when the spacing of the two zone plates is =(1/2m±1/4) λ.[24]

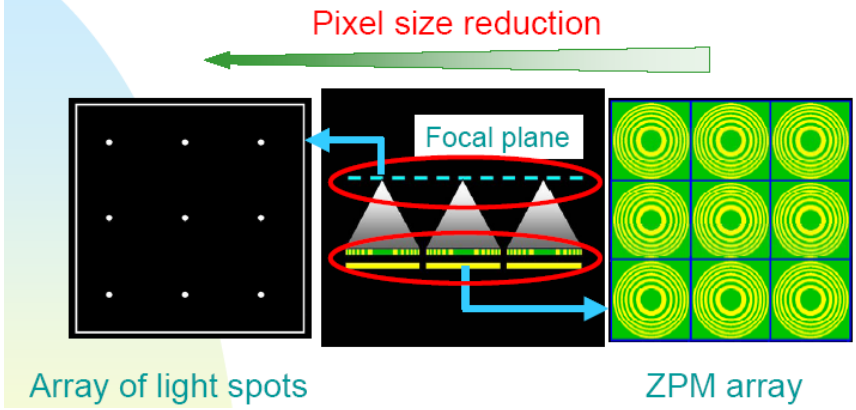

Figure 1.13. An array of zone plate modulators can act as a pattern generator for maskless lithography.[24]

1.4.2 Charged particle maskless lithography

Charged particle lithography has higher resolution than optical lithography, which makes it very appealing for critical layers printing. Charged particle lithography appeared as maskless lithography during the 1960s~1970s. Early direct-write e-beam lithography tools suffered from the low throughput with single Gaussian or shaped beams.[26] IBM had pioneered in the development of early e-beam direct-write systems. Its EL-1 system could write 22 wafers (57mm in diameter) per hour (WPH) in the 1970s. Even though the exposure pixel rate of the EL series shaped e-beam direct-write lithography tools had been increased from 2×10^7 pixel/second in 1975 to 2×10^9 pixel/second in 1993, the exposure pixels per wafer had been increased by three orders of magnitude, which caused the throughput decrease to 1 WPH (fig. 1.14). With an additional decade of development in IC, the throughput of the fastest e-beam direct write system has been decreased to less than 0.1 WPH on 300 mm wafers. Early e-beam direct-write lithography tools failed to keep up with Moore's laws prediction.

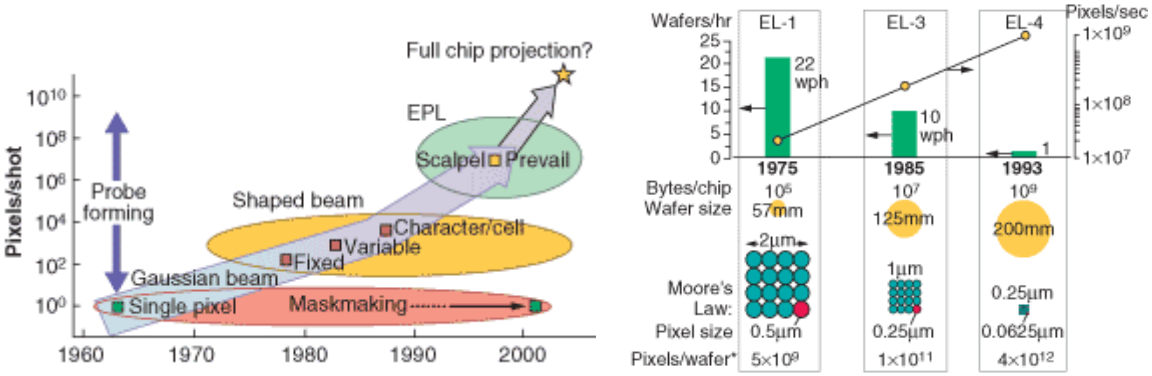

Figure 1.14. Evolution of the e-beam lithography (left side) and the throughput of the electron beam direct-write lithography tools developed by IBM (right side).[26]

Because of the escalating mask costs after the adoption of PSM and OPC, charged particle maskless lithography regained the attention as a potential next generation lithography approach to provide a low cost lithography solution with fast-turn-around-time for low volume production and prototyping, to provide higher print resolution and larger process latitude than the traditional optical lithography. The key to the future success of charged particle maskless lithography is the improvement of throughput by incorporating higher parallelism in exposures. Many innovative designs have been proposed to solve this problem. These throughput-enhancement technologies can be summarized into two major categories. The first type is the multiple beam approach, which includes the different combinations of the single or multiple source design with the single or multiple column design. If a single source is used, the illumination beam will be split into multiple beams through an aperture plate. Multiple column designs are adopted to reduce the coulombic interactions by dividing the beam into multiple paths and eliminating the common cross-over in multi-beam-single-column design. The second category is to use character projection or cell projection (CP) techniques, which increases the number of exposure pixels per shot. The combination of CP technique with multiple beam approach has also been proposed. Based on the classification method talked above, some of the developing CP-ML2 systems are briefly reviewed in table 1-1. The technical characteristics of each system have been explained briefly in the table.

Table 1-1. The currently developing charged particle maskless lithography systems.

Project name	Associated consortiums	Category	Technical characteristics
NEDO Multi-e beam system	Canon & Hitachi High-Technologies	Multiple beam and single column	Single electron source is separated into 32×32 multiple beams through an aperture array plate. After passing through the electrostatic lens array and micro-aligner array, the 1024 beams are focused onto a blanker array. Then the 1024 beams are further focused onto the wafer through a single reduction column.[27]
Multiple Column Cell projection system (MCC)	Advantest	Multiple beam and multiple column	50 keV beam voltage, 4×4 sources and columns in the first generation MCC system. Variable shaped, character projection or variable character projection design in each column. 0.2×0.2 mm major deflection field and 10×10 μm minor deflection field. Challenges lie at the field uniformity of the multiple column array and the interference of the different column.[28]
Low energy electron beam direct write (LEEBDW)	e-BEAM Corporation	Single shaped beam, character projection	5 keV beam energy with 1.0 A/cm^2 current density. Vector scanning with character projection and variable shaped beam method. 2 WPH at 200 mm wafer on all layers. 10 WPH on some layer with best case.[27]
Projection maskless lithography (PML2)	IMS Jenna GmbH, Leica Microsystems Lithography GmbH.	Multiple beam in single column	100 keV final beam energy. Single electron source is split into 290,000 multiple beams through programmable aperture plate (PAS). 5×5 μm^2 aperture size. 200 reduction ratio on projection optics. The PAS system consists of cover plate, blanking plate and aperture plate. 64 grey levels during exposure. Toggle rate 1MHz.[29]
MAPPER	MAPPER Lithography	Multiple beam and multiple column	Single source is used. Multiple beams are generated through an aperture array. Each beam has separate columns. Beam blanking is realized optically through multiple laser beams. Target throughput is 10 WPH.[30]
Distributed Axis Variable Shaping system (DIVA)	Stanford University	Multiple beam and multiple column	Modulated lasers illuminate the photocathodes to generate multiple electron beams. Uniform magnetic field focus the electron beams onto the wafer. An aperture plate is placed in the middle to accelerate the electrons and define the electron beam objects on the source plane.[31]
ETEC multibeam lithography tool	Etec systems (An Applied Materials company)	Multiple beam and single column	Modulated lasers illuminate 32 photocathodes and generate 32 electron beams, which are accelerated to 50 keV. A common electron optics column is used.[32]
Multiple focused ion beam system	Lawrence Berkeley National Lab.	Multiple beam and multiple column	Multiple ion beams are generated when the low energy ions pass through switchable apertures in a pattern generator. Ion beams are accelerated and focused by counter-bored shaped focusing electrode array.[33,34]
Maskless Micro-ion-beam Reduction Lithography (MMRL)	Lawrence Berkeley National Lab.	Multiple beam and single column	A switchable pattern generator, directly facing an rf plasma source, generates multiple ion beams, which can be individually switched on and off using 10 volts of biasing voltage. A large field electrostatic ion optics column accelerates the beam to 75 keV and focus the ion beams by 10 X onto the wafer.[33,35]

1.5 Maskless ion beam lithography research in the Lawrence Berkeley National Laboratory

The heart of a maskless lithography system is the pattern generator. For CP-ML2, the pattern generator allows the generation of individually controllable multiple electron or ion beams. The energy of the ions after passing through a plasma sheath can be a couple of electron volts. If a switching aperture array directly faces a plasma source, ion beamlets can drift out through the patterned apertures, which can be shut-off by applying a couple of volts of retarding voltage on the patterned electrodes on the exit of the apertures.

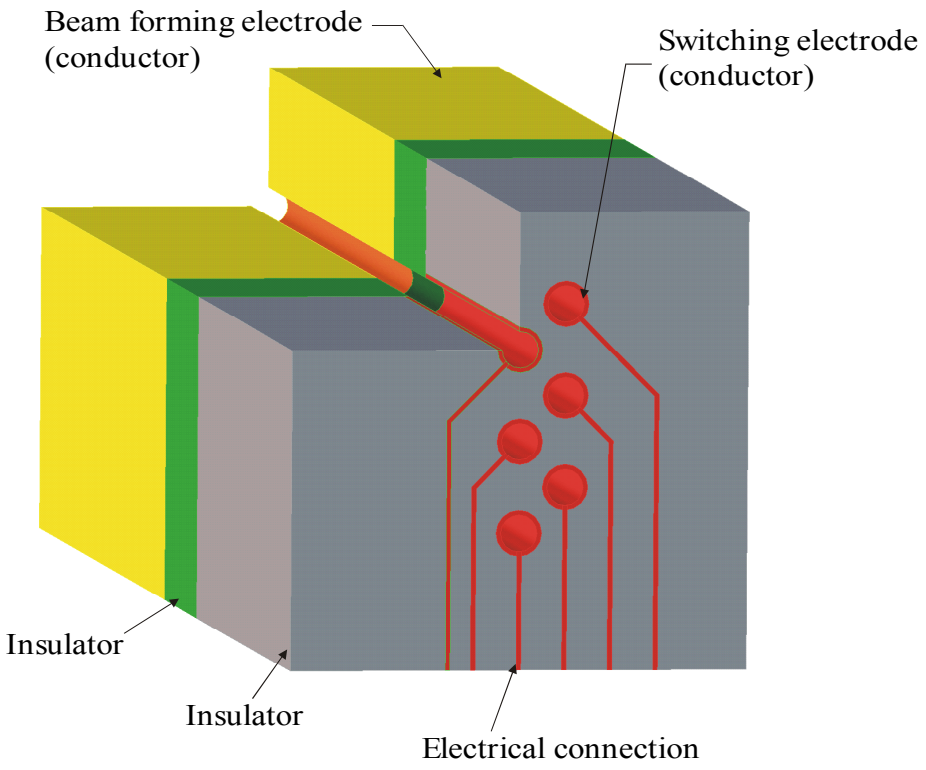

Figure 1.15. One of the switching pattern generator designs for the Maskless Micro-ion Beam Reduction Lithography system.[36]

One of the pattern generator designs is shown in fig. 1.15.[36] The thick beam-forming electrode is conductive and directly faces the plasma sheath. The middle insulator layer separates it from the switching electrodes. Voltage biasing can be individually applied to the switching electrodes with insulating material separating each electrode. Due to the low beam switching voltage, the pattern generator can be fabricated into a thin membrane layer through a self-aligned microfabrication process. Two maskless lithography approaches, multiple focused ion beam system and Maskless Micro-ion-beam Reduction Lithography (MMRL) system, are being developed in LBNL based on this type of pattern generation.[34,35]

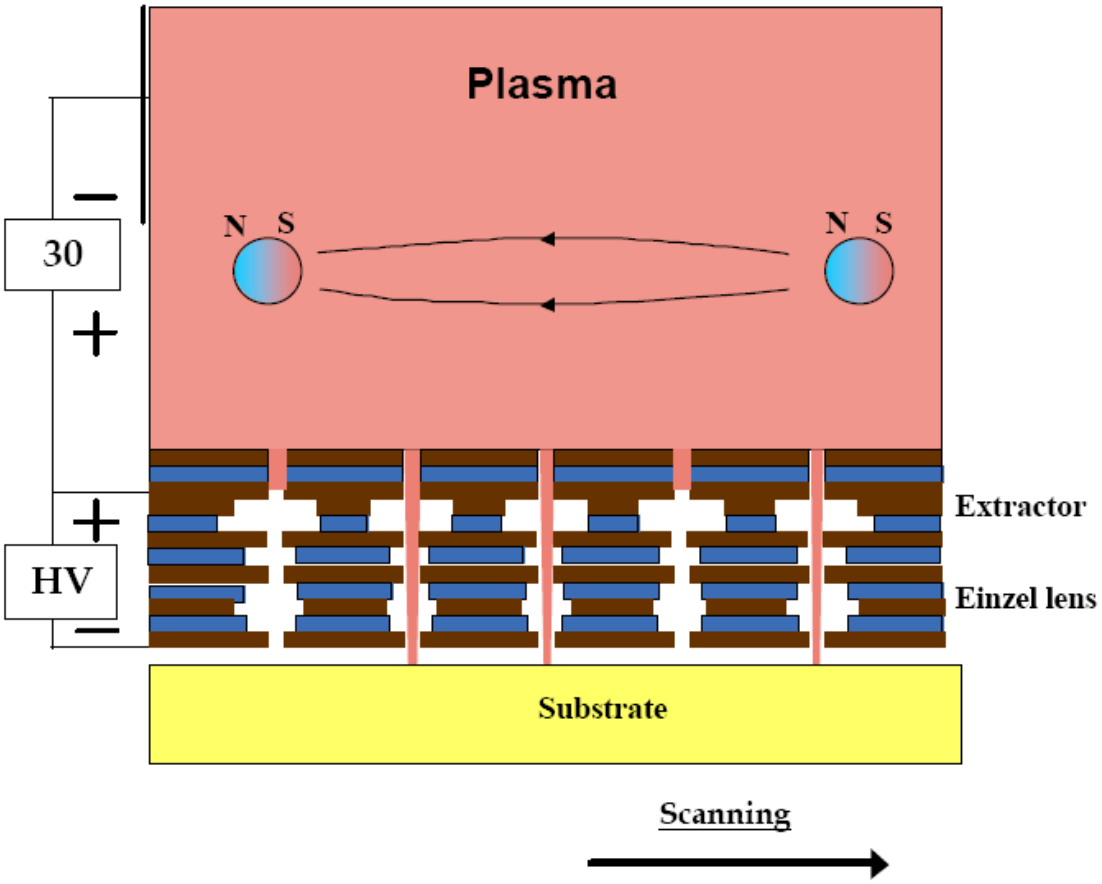

Figure 1.17. Schematic diagram of a multiple focused ion beam system.[34]

The multiple focused ion beam system is a multiple-beam-multiple-column system (fig. 1.17).[34] The counter-bore-shaped extractor design can help to reduce the aberrations caused by the extraction electrodes. An Einzel lens has been used in each column to further reduce the beam size and focus them onto the wafer. Multiple column design and short column lengths will greatly reduce the columbic interactions of the ion beams. In order to achieve 60 second exposure time on a 300 mm wafer, 4 million ion beamlets are required.

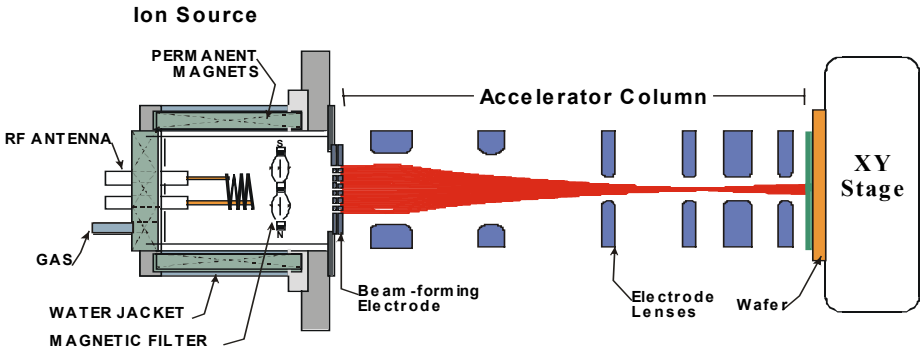

Figure 1.18. Schematic of the Maskless Micro-ion Beam Reduction Lithography sysem.[35]

It's difficult to achieve a high ion energy in the multiple focused ion beam system because of the employment of the compact ion optics column. However, MMRL system has a large and long electrostatic ion optics column, which can accelerate the ions to a final energy of 75 keV and reduce the beam size by 10 times. The schematic diagram of the MMRL system is shown in fig. 1.8.[37] The MMRL system can work both in projection mode and in maskless mode depending on whether a mask or pattern generator is used as the beam-forming electrode. Compared with the traditional IPL system, MMRL totally

eliminates the ion beam illumination column. A large area radio-frequency plasma ion source is directly placed in front of the beam-forming electrode (mask or pattern generator).

The prototype MMRL system is built by V.V. Ngo, a former graduate student in the Plasma and Ion Source technology group of LBL, and his colleagues. The development of the prototype MMRL system has been discussed in his Ph.D. thesis.[35] The work described in this thesis pursues the continuing development of MMRL, focusing on the ion optics analysis and the development of microfabricated pattern generators. The configuration of the MMRL system will be introduced in Chapter 2. The aberrations of the ion optics column will be re-evaluated in Chapter 3. The resolution capability was greatly improved after the installation of a limiting aperture on the cross-over plane of the optics column and the reduction of the electromagnetic interference. The throughput capability will also be investigated by analyzing the charged particle interactions and the requirements on mechanical stages. In order to achieve a sub-100 nm pixel size in maskless mode, a microfabricated pattern generator is required. Several versions of prototype microfabricated pattern generators have been developed. Ion beamlet switching has been successfully demonstrated for the first time with a microfabricated pattern generator. The development of the pattern generator will be presented in Chapter 4.

Reference:

[1] A. K. Bates, M. Rothschild, T. M. Bloomstein et al., "Review of technology for 157 nm lithography", IBM Journal of Research and Development **45** (5), 605 (2001).

[2] Aaron Hand, "157 nm Optics Demand a Bag of Tricks", Semiconductor International (2002).

[3] Katherine Derbyshire, "Next-generation lithography: beyond 100 nm", Semiconductor Magzine **2** (9) (2001).

[4] Chris A. Mack, "The lithography expert: Resolution enhancement technologies", Microlithography World **12** (2) (2003); Chris A. Mack, "The lithography expert: Off-axis illumination", Microlithography World **12** (3) (2003).

[5] Chris A. Mack, "Scattering bars", Microlithography World **12** (4) (2003).

[6] Chris A. Mack, "The lithography expert: Immersion lithography", Microlithography World **13** (2) (2004); M. Switkes, M. Rothschild, R. R. Kunz et al., "Immersion lithography: Beyond the 65 nm node with optics", Microlithography World **12** (2) (2003).

[7] T. H. P. Chang, "Instrumentation for electron-beam lithography", IEEE Transactions on Magnetics **MA10** (3), 883 (1974); T. H. P. Chang, "Proximity effect in electron-beam lithography", Journal of vacuum Science and Technology **12** (6), 1271 (1975); J. L. Mauer, H. C. Pfeiffer, and W. Stickel, "Electron optics of an electron-beam lithography system", IBM Journal of Research and Development **21** (6), 514 (1977).

[8] A. M. Hawryluk and L. G. Seppala, "Soft-X-Ray projection lithography using an x-ray reduction camera", Journal of vacuum Science and Technology B **6** (6), 2162 (1988).

[9] Yasuhiro Horiike and Masashi Ogawa, "Development of Extreme Ultraviolet Lithography in Japan", Future Fab International **18** (19) (2005).

[10] Peter J. Silverman, "Extreme ultraviolet lithography: overview and development status", Journal of Microlithography, Microfabrication, and Microsystems **4** (1), 011006 (2005).

[11] Naoya Hayashi,"Challenges of EUV masks and preliminary evaluation" presented at the SEMATECH international EUV mask workshop(November 1st 2004).

[12] Masaki Yoshioka,"Supplier's perspective on cost of ownership of EUV sources" presented at the SEMATECH internatioinal EUV source workshop(February 27th 2005).

[13] H. C. Pfeiffer, "Variable spot shaping for electron-beam lithography", Journal of vacuum Science and Technology **15** (3), 887 (1978).

[14] R. S. Dhaliwal, W. A. Enichen, and S. D. Golladay, "PREVAIL-Electron projection technology approach for next-generation lithography", IBM Journal of Research and Development **45** (5) (2001).

[15] Lloyd R. Harriott, "Scattering with angular limitation projection electron beam lithography for suboptical lithography", Journal of vacuum Science and Technology B **15** (6), 2130 (1997).

[16] Takaharu Miura, Shintaro Kawata, and Kazunari Hada,"Nikon EPL tool: The latest development status and results" presented at the Proceeding of the SPIE-

microlithography conference, Emerging Lithographic Technologies IX,SPIE,5751,477(2005).

[17] Rainer Kaesmaier and Hans Löschner,"Overview of the Ion Projection Lithography: European MEDEA and International Program" presented at the Proceeding of the SPIE-microlithography conference, Emerging Lithographic Technologies IV3997,19(2000).

[18] Yvette Lee, "Production of Low Axial Energy Spread Ion Beams with Multicusp Sources", University of California, 1998.

[19] Byron D. Gates, Qiaobing Xu, and J. Christopher Love, "Unconventional Nanofabrication", Annual Review of Materials Research 34, 339 (2004).

[20] Aaron Hand, "One on One: A closer look at Nanoimprint", Semiconductor International Septermber (2004).

[21] Hisashi Watanabe and Iwao Higashikawa, "Mask cost and specification", Proceedings of SPIE, 23rd Annual BACUS Symposium on Photomask Technology **5256**, 423 (2003).

[22] Hans Martinsson, Tor Sandstrom, Arno Bleeker et al., "Current status of optical maskless lithography", Journal of Microlithography, Microfabrication, and Microsystems **4** (1), 011003 (2005).

[23] Peter Buck, "Optical lithography: The future of mask manufacturing?" Microlithography World **11** (3) (2002).

[24] Baokang Bi,"High-throughput maskless lithography (HT-MLL) based on Zone Plate Modulator (ZPM)" presented at the Proceeding of the maskless lithography workshop by SEMATECH international (January 17th 2005).

[25] K. F. Chan, Z. Feng, and R. Yang, "High resolution maskless lithography", Journal of Microlithography, Microfabrication, and Microsystems **2** (4), 331 (2003); M. Klosner and K. Jain, "Massive parallel, large-area maskless lithography", Applied Physics Letter **84** (15), 2880 (2004).

[26] Hans C Pfeiffer, "The history and potential of maskless e-beam lithography", Microlithography World **14** (1) (2005).

[27] Shinji Okazaki,"Recent development activities on maskless lithography in Japan" presented at the Proceeding of the maskless lithography workshop by SEMATECH international(January 17th~19th January 17th~19th, 2005).

[28] Akio Yarnada,"Advantest's EBDW System; MCC System with CP" presented at the Proceeding of the maskless lithography workshop by SEMATECH international (January 17th~19th, 2005).

[29] Christoph Brandstätter and Hans-Joachim Döring,"Projection Maskless Lithography (PML2) Technology - Results" presented at the Proceeding of the maskless lithography workshop by SEMATECH international (January 17th~19th, 2005).

[30] Bert Jan Kampherbeek and Guido de Boer,"MAPPER: High throughput maskless lithography" presented at the Proceeding of the maskless lithography workshop by SEMATECH international (January 17th~19th 2005).

[31] Fabian Pease, Daniel Pickard, and Zhi Liu,"Charged particle maskless lithography (CPML2)" presented at the Proceeding of the maskless lithography workshop by SEMATECH international (January 17th~19th, 2005); D. S. Pickard, C. Campbell, and T. Crane, "Distributed axis electron-beam system for lithography and

inspection-preliminary experimental results", Journal of vacuum Science and Technology B **20** (6), 2662 (2002).

[32] S. T. Coyle, B. Shamoun, M. Yu et al., "Progress toward a raster multibeam lithography tool", Journal of vacuum Science and Technology B **22** (2), 501 (2004).

[33] K. N. Leung, Bret V. D. Akker, and Y. Chen,"Maskless Ion Beam Lithography Projects at LBNL" presented at the Proceeding of the maskless lithography workshop by SEMATECH international (January 17th~19th, 2005).

[34] Qing Ji, "Maskless, resistless ion beam lithography processes", Unversity of California-Berkeley, 2003.

[35] V.V. Ngo, "Experimental demonstration of a Prototype Maskless Micro-ion-beam Reduction Lithography System",Ph.D. Thesis, Unversity of California 2005.

[36] Y. Lee, W. A. Barletta, and K. N. Leung, "Multi-aperture extraction system with micro-beamlet switching capability", Nuclear Instruments and Methods in Physics Research A **474**, 86 (2001).

[37] V.V. Ngo, W. Barletta, R. Gough et al., "Maskless Micro-ion-beam reduction lithography", Journal of Vacuum Science and Technology B **17** (6), 2783 (1999).

Chapter 2:

Prototype MMRL system and previous experimental results

The prototype Maskless Micro-ion-beam Reduction Lithography system was developed by Dr. Vinh V. Ngo and his colleagues in the Plasma and Ion Beam Technology Group in LBNL. The initial system design and the resist exposure results have been reported by V. V. Ngo in his Ph.D. thesis.[1] The prototype system design and the previous resist exposure results will be briefly reviewed in this chapter.

MMRL system consists of a vacuum sub-system (including the chamber and the pumping system), a 75 keV electrostatic ion optics column, an rf-driven plasma ion source, a high voltage power supply sub-system and an automation control sub-system. After the prototype MMRL system was developed, Dr. V.V. Ngo tested the resolution capability in the projection mode of operation. The resist exposure results showed that the actual resolution capability is much worse than the simulation result. In addition, beam switching experiment with a mechanically fabricated device was also performed on MMRL, which showed that 2 volt positive voltage can successfully switch off the ion current.

2.1 Mechanical and vacuum sub-systems for MMRL

The mechanical systems on MMRL consists of an rf-driven multi-cusp plasma ion source, a high-vacuum chamber that houses an electrostatic ion optics column, a load-lock chamber to exchange wafers between atmospheric pressure and the vacuum chamber and a high precision three-axis stage to move wafers. The mechanical structure of MMRL is presented in fig. 2.1. The main supporting frame floats on four air legs in order to reduce and dampen the vibrations caused by the cooling water flow, the turbo pump and the trembling of the building infrastructure.

A large pumping pipe connects to the high vacuum chamber through a large quadrate-shaped duct. It also connects to the ion source chamber through a small ceramic tube. High pumping conductance between the main chamber and the pump is required to obtain a low chamber pressure ($<5\times10^{-5}$ Torr for helium) in order to hold the voltages between the electrodes of the electrostatic column. A pressure-activated shutting valve between the ion source and the pumping line can be used to regulate the pumping rate of the ion source. The valve should be open to pump out out-gassing impurities during the initial stage of operation. In the event of high-pressure ion source operation, the valve will close, increasing the pressure difference between the ion source and the main chamber. Valve control is helpful to obtain a high operation pressure in the ion source while maintaining a low vacuum pressure in the main chamber. The other end of the vacuum line is connected to a 1000 litter/s turbo pump, followed in series by a roughing scroll pump.

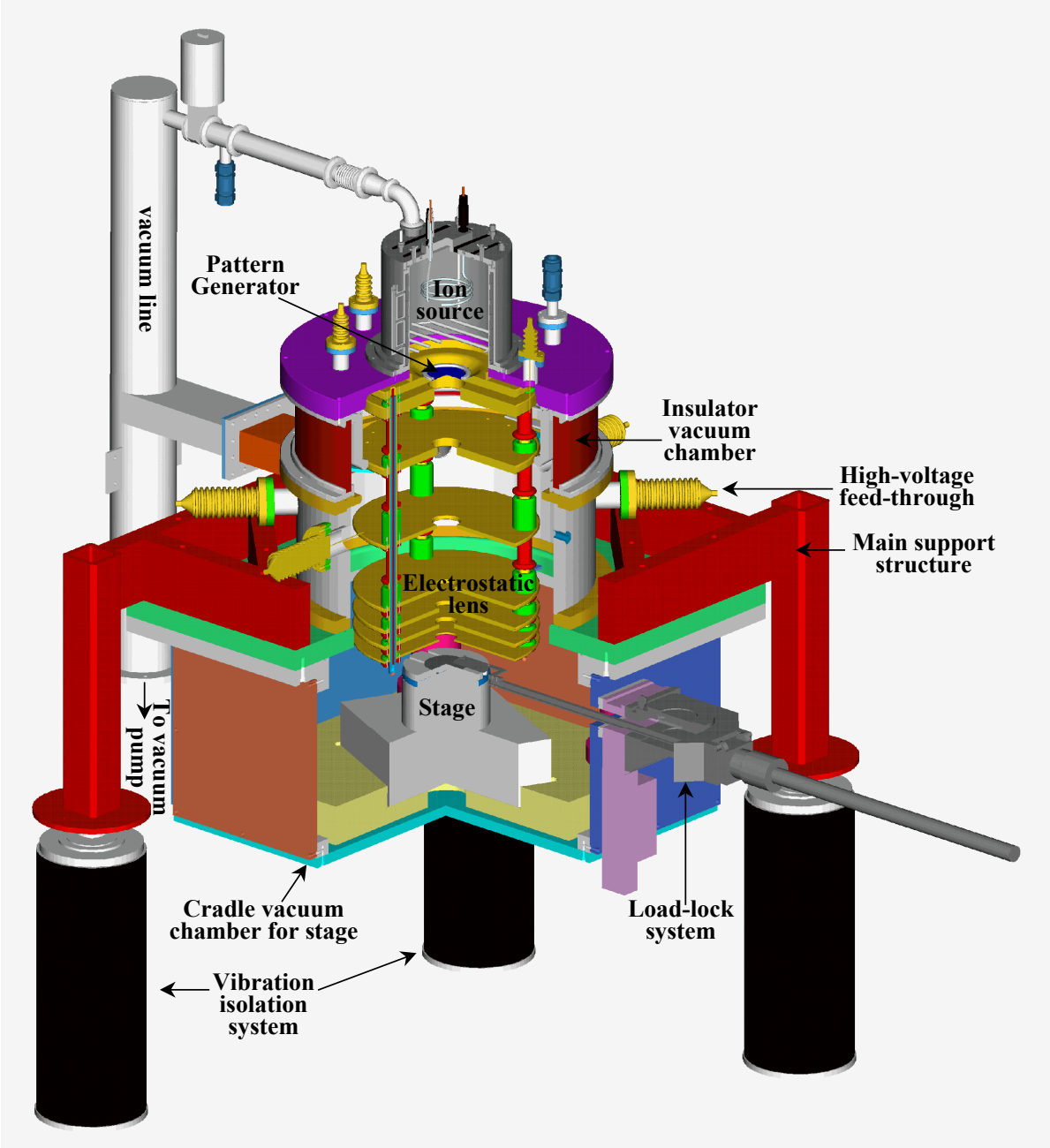

Figure 2.1. Cut view of the prototype MMRL system.

High voltages are applied to the electrodes through ceramic feed-throughs installed on the bottom stainless steel chamber wall and the top lid, where the ion source sits. When the high voltage is applied, the voltage on the top lid is at 75 kV. But the bottom part of the main chamber and the pumping pipe are kept at ground potential. This potential difference is the basis for the top section of the cylindrical chamber wall and part of the by-pass tube between the ion source and pumping line to be made out of ceramic insulator.

2.2 Electrostatic ion optics column

The electrostatic ion optics column consists of eight electrodes with different thickness and inner-diameters while sharing the same outer diameter size--- 30.0 cm. So the whole column assembly can be aligned on a "V-block", which is made of two flat aluminum surfaces as shown in fig. 2.2. The dimensions and the applied voltages of the electrodes are illustrated in fig. 2.3. The surfaces of the electrodes are gold-anodized to prevent surface oxidation, which may cause the charges on the electrode surface and create additional lens aberrations. Electrodes are held together by three fiberglass rods installed with 120^0 circumferential intervals. Ceramic and plastic insulating spacers are placed between the electrodes to control the spacing determined by the MEBS optics design software. The round donut-shaped aluminum rings at the joint serve as triple point protection to prevent arcing between electrodes (fig. 2.2). The parallelism and concentricity of the column assembly have been carefully inspected before the

installation into the system (fig. 2.4). The preciseness is very critical to the ion optics system in MMRL because there is no alignment deflector unit in the column to correct any misalignment. The whole column is suspended onto the vacuum chamber wall by three ceramic levers, which can be seen in fig. 2.4.

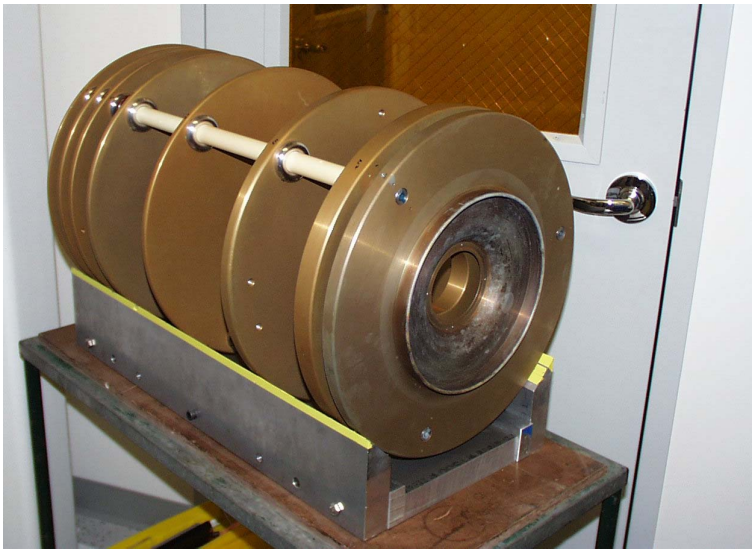

Figure 2.2. MMRL ion optics column is alignment on a "V-block".[1]

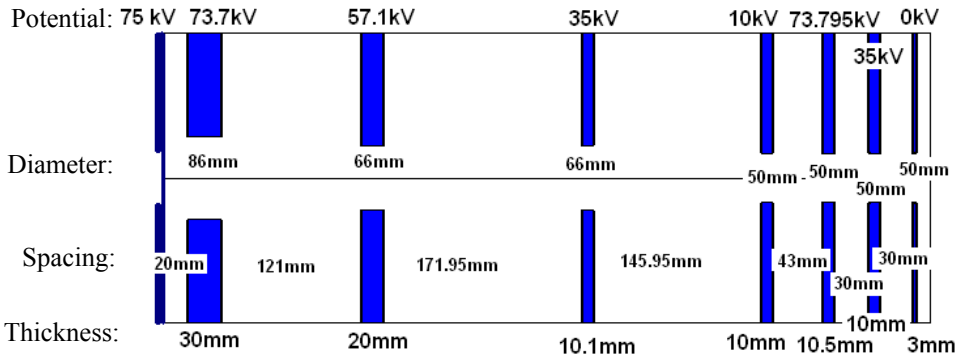

Figure 2.3. Design parameters of the original MMRL ion optics column

Figure 2.4. Parallelism and concentricity inspection. [1]

2.3 Electronics sub-system for MMRL

The electronics component for MMRL consists of a high voltage sub-system and an automation control sub-system. The high voltage sub-system diagram has been plotted in fig. 2.5, which is a revised version based on the original one used by Vinh Van Ngo. The updated version shows the actual high voltage setup more clearly. Helium or hydrogen plasma is generated by the coupling of 13.56 MHz rf power to the gas. A transformer-type matching-network matches the plasma impedance to the rf power supply impedance (50 Ω). Input rf power can be as high as several hundred watts. The ion source and the rf power supply are both biased to 75 kV. Consequently, the rf power supply must be powered by a high voltage isolation transformer. The voltage of 75 kV is achieved by floating a 17.9 kV supply on a rack powered through an isolation transformer biased at 57.1 kV. The HV supplied to electrode #1, #3 and #6 are also powered through the transformer. Electrode #1 is also charged to 75 kV. Then a 1.3 kV

negative power supply, floating on 75 kV, produces a high voltage of 73.7 kV to electrode #2. A voltage of 73.8 kV is applied to electrode #6 by floating 16.7 kV on 57.1 kV. All of the other electrodes are charged by high voltage supplies that are directly powered through a 208V AC power on ground potential.

The ion beam exposure process in MMRL is controlled by an automation system illustrated in fig. 2.6, which is an updated version based on the original one described in Ngo's thesis.[1] In order to realize the proof-of-concept maskless lithography, the function of remotely controlling a multi-aperture pattern generator has been incorporated into the updated automation system. MMRL can be operated in either a projection mode or in a maskless mode. In the projection mode, a pre-patterned stencil mask will be installed at the first electrode. When ion beams drift out through the mask, they keep in a pattern as the mask. Then they will be accelerated to 75 keV and focused onto a wafer with the size reduced by 10x. The automation program will start off by moving the stages to a desired position before the plasma is turned on. Then the plasma will be started and sustained for a time specified in a Labview program. After the exposure, the stage will be moved to the next position. The movement of the stage is more complicated in maskless mode. It can be operated in a manner similar to the projection mode or in a totally different swath mode. This topic will be discussed with more detail at the end of Chapter 3, because it significantly affects the throughput of MMRL. The movement of the stage and the control of the bias voltages, used to switch the ion beamlets on and off, must be precisely coordinated to generate desired patterns on the wafer in the maskless mode. As a result, the tolerance of the timing accuracy for the computer and other electronics, and the

precision of the stage are very stringent in order to generate useable patterns in sub 100 nm scale.

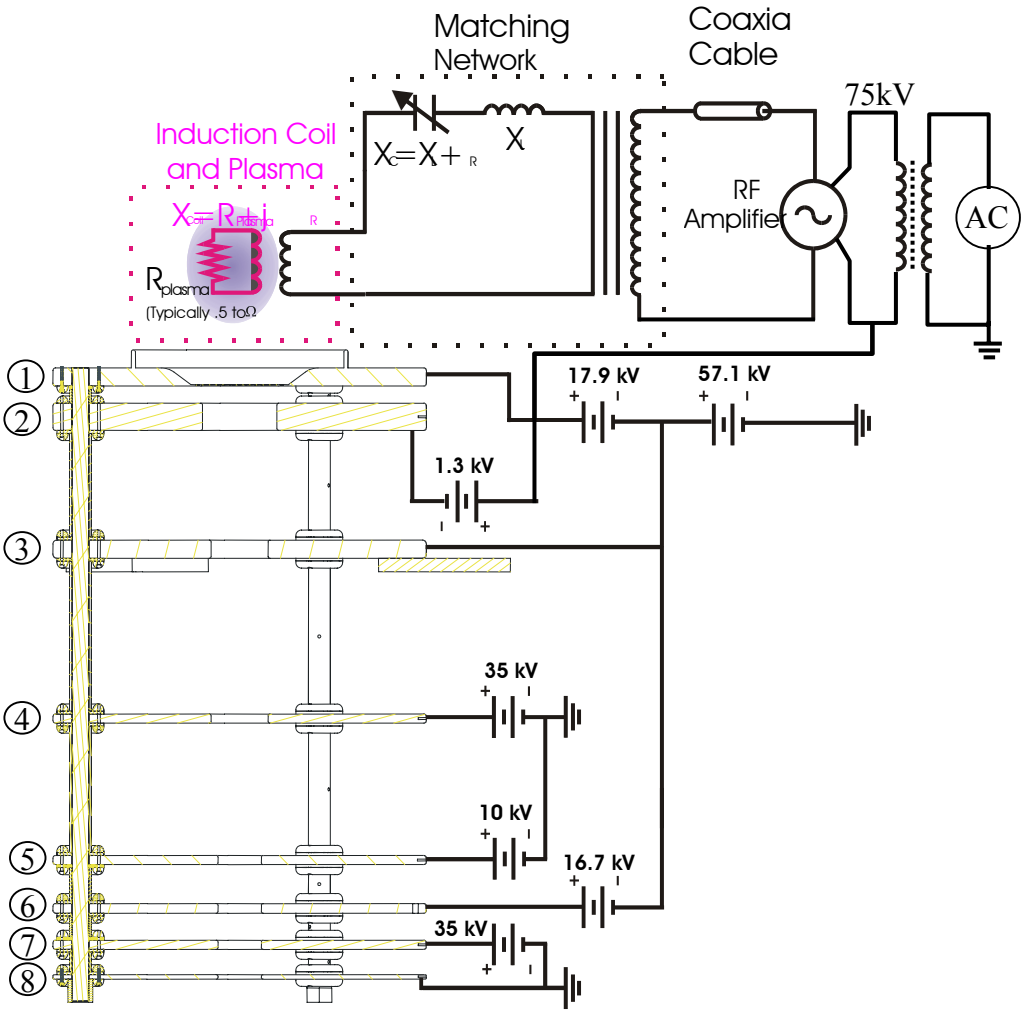

Figure 2.5. MMRL high voltage power supply sub-system.[1]

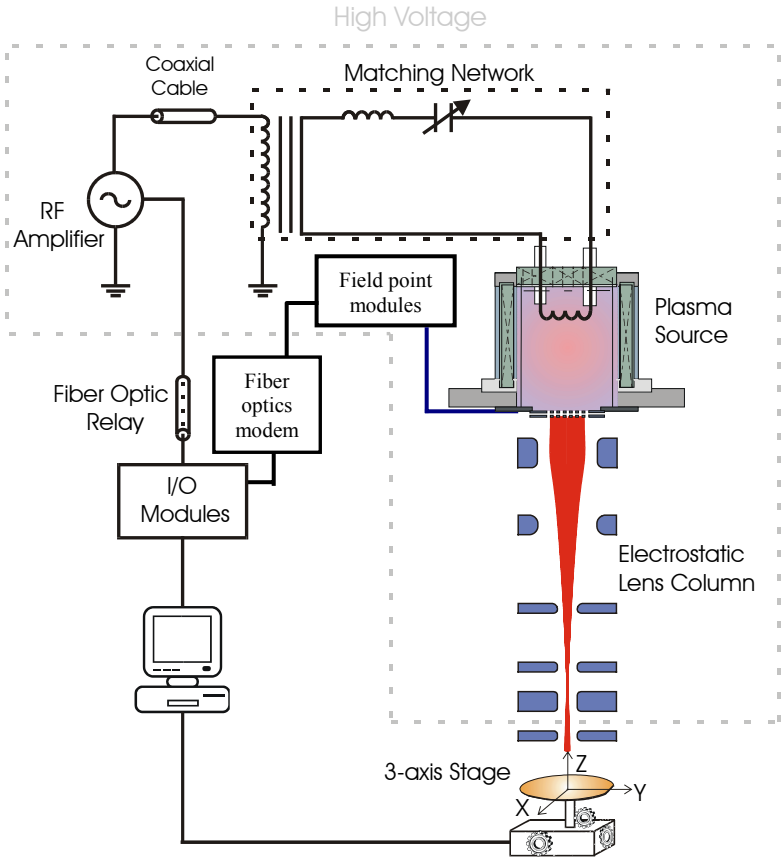

Figure 2.6. Structure of the automation control unit for MMRL.[1]

During a resist exposure experiment, the rf amplifier, the microfabricated pattern generator and the 3-axis stage are simultaneously controlled by a computer. The structure of the automation control sub-system is plotted in fig. 2.6. The rf amplifier and the pattern generator are powered at a 75 kV potential. But the computer is operated at the ground potential, so optical fibers are used to transmit the signal from the ground potential to the 75 kV potential. Pairs of fiber optics relays and modems are used to convert ground potential electrical signals to optical signals, and restore them to electrical

signals at a 75 kV potential. Two eight-channel field-point modules provide 16 independently controlled biasing voltages from 0 to 10 volts.

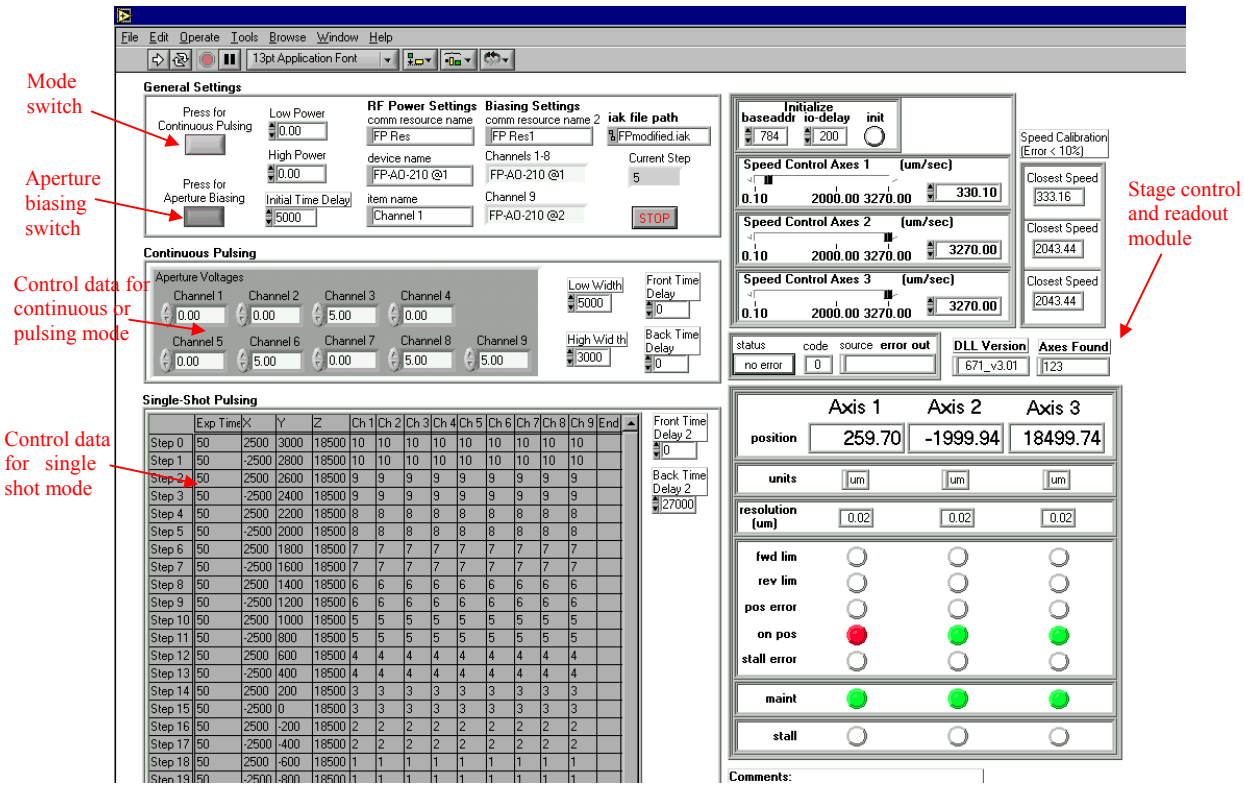

Figure 2.7. Updated Labview control program with the feature of setting the bias voltages to switch apertures on pattern generators.

Computer automation control is managed in a Labview program with an interface shown in fig. 2.7. The Labview program sends out rf power, stage position, and aperture biasing voltage data to I/O modules. These data will then be transmitted to the different system devices. The top left panel ("general settings" panel) has a mode switch for continuous-pulsing mode and single-shot mode. In continuous pulsing mode, the

Labview program will manipulate the rf amplifier output according to the pulse setting specified by “Low Width” and “High Width” blanks, where the rf amplifier will have either a low or high output, respectively. In the meantime, the bias voltage data for each channel (in the “continuous pulsing” panel) will be transmitted to the fieldpoint modules, which will generate analogue voltages to switch the apertures on and off. This mode of operation can be used to discharge clean the ion source, and to measure the ion current before and after the ion beam exposure experiment.

The other important and useful mode is the single-shot mode. The exposure data for this mode are listed in a table in the “single-shot pulsing” panel, which specifies the exposure time in ms, the XYZ stage position in μm and the aperture biasing voltages in volts. After the stage is moved to a specified position, the aperture bias voltages are set in the fieldpoint modules according to the values on the table. After the pre-exposure time delay (“front-time delay”) is over, the program will start the plasma and sustain it for the duration of time specified in the exposure time column. After one raw of exposure data in the table is completed, the plasma will be turned off. The stage will be moved to the new position listed in the next column after a time specified by the post-exposure delay (“back-time delay”). The whole process will be repeated until a table-end flag (text “1”) is met.

2.4 The plasma ion source for MMRL

A multicusp rf-driven ion source has been used on the MMRL system, It works in inductively coupled mode. A uniform hydrogen or helium plasma as large as 19 cm in diameter can be produced by the ion source. The large-area uniform plasma can be used

to directly illuminate a pattern generator or a mask without a complicated beam illumination column. The 3-D model of the ion source is shown in fig. 2.8. The rf antenna is made out of a water-cooled Tungsten or Titanium tubing covered with a quartz sheath. When several hundred watts of 13.56 MHz rf power is applied to the antenna, a high rf voltage can be generated between the two ends of the antenna, and between the antenna and the source wall. Without any protection, the antenna would be quickly damaged by ion sputtering. The metal sputtered from the antenna may also eventually clog up the apertures on the pattern generator. The outer quartz sheath can prevent the sputtering damage to the antenna, because the charge build up on the quartz surface will shield the high voltage between the antenna coil and the plasma. The cylindrical source chamber wall and the backplate are all water-cooled.

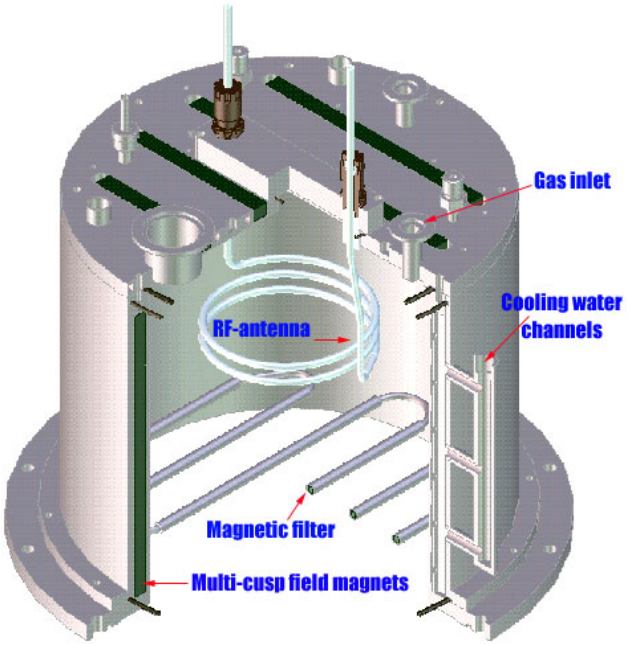

Figure 2.8. 3-D cut view of the MMRL ion source. [1]

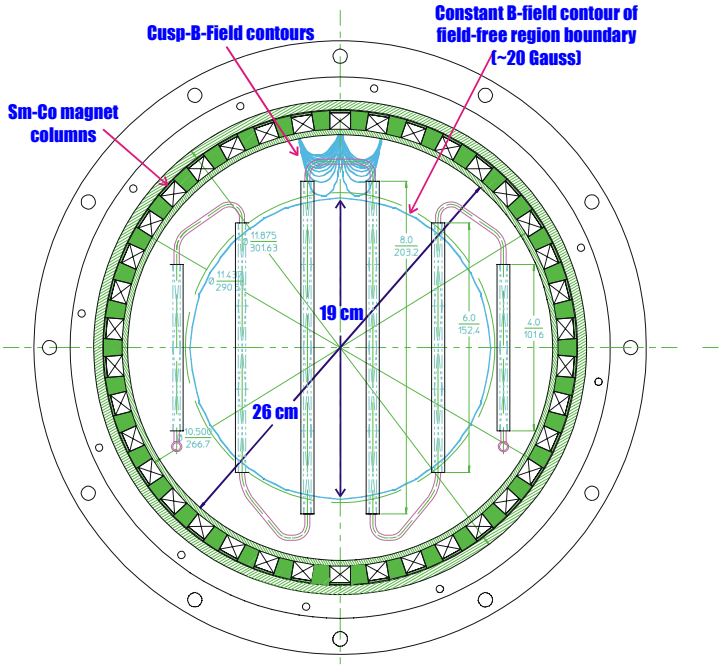

Figure 2.9. Multi-cusp magnets arrangement and the magnetic filter. [1]

Samarium-cobalt permanent magnets are embedded in the chamber wall and in the backplate with alternating polarity in order to generate magnetic field cusps (fig. 2.9) to confine electrons. The magnets can increase the plasma density, lower the plasma potential and improve the plasma uniformity. V. V. Ngo has studied the radial plasma density profile with a Langmuir probe.[1] The result has been presented in Figure 2.10. A plasma density variation less than 15% has been obtained within a radius of 9 cm at different rf powers. It is very difficult to obtain an object field larger than 1.0 cm in charged particle projection optics. Consequently, the usable object field size in MMRL will be less than 10 mm. The radial plasma density variation within a radius of 5 mm

(pointed out by the red line in fig. 2.10) is less than 3%. Considering the large process latitude in charged particle lithography, 3% dose variation is definitely acceptable.

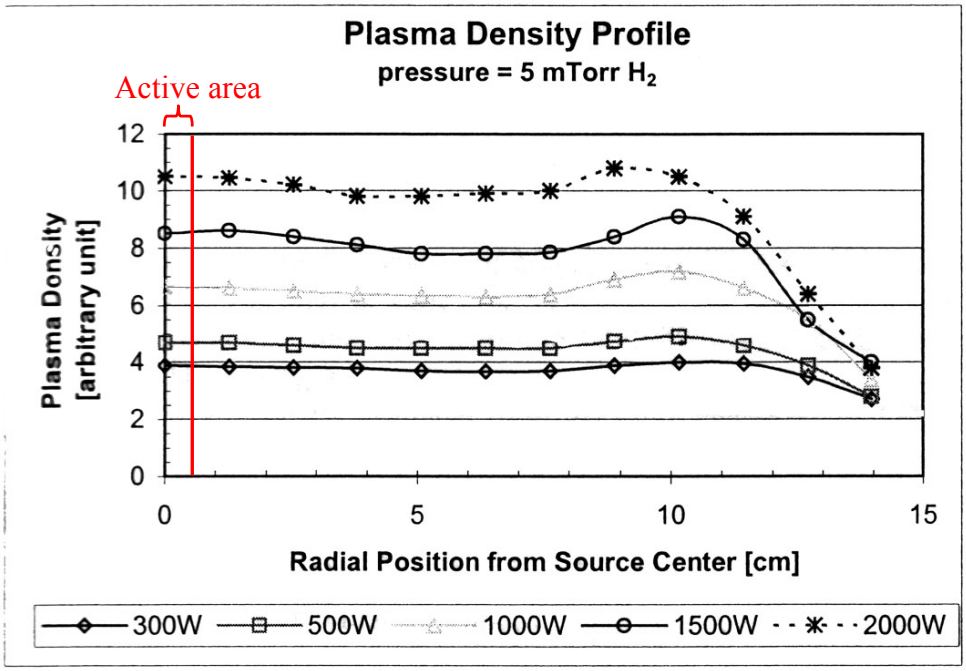

Figure 2.10. Radial plasma density profile of the multicusp ion source used in MMRL system.[1]

A strong magnetic filter is installed between the pattern generator and the antenna. The filter B field confines the ionizing electrons within the plasma generation volume. So most of the ions are produced within the bulk of the plasma, which has a uniform plasma potential. Thus it results in a low axial energy spread of the ions. Yvette Lee, a former graduate student of our group, has extensively studied the energy spread of rf-driven plasma ion sources.[2] Energy spread as low as 2.5 eV can be obtained from an rf multi-cusp plasma ion source with a strong magnetic filter.[3] The low energy spread is essential in the reduction of chromatic aberrations for ion beam lithography applications. A

conventional ion projection lithography system developed at Fraunhofer Institute-ISiT Germany has successfully improved its resolution to 50 nm after the installation of a low-energy-spread multi-cusp ion source developed by our group.[4]

2.5 Ion beam exposure experiments on prototype MMRL system

After the prototype MMRL system was developed, V.V. Ngo tested its resolution capability when operated in projection mode. The first ion beam exposure experiment was carried out with a copper hard mask machined with a mechanical method. The dimensions of the mask and the exposure result are shown in fig. 2.11. The mask has 13 apertures, with a diameter of 200 μm. The apertures are aligned to form a cross pattern. The area covered by the cross pattern was thinned down to 250 μm-thick. If the resolution was better than 20 μm, the expected image on the resist should have been 13 individually discernable apertures with a 20 μm diameter. But the actual image, in fig. 2.11, only showed a large cross pattern on the resist. The reason was because the diameter of the apertures on the resist were so large that they overlaped with each other and formed a large cross pattern.

There were two possible explanations for the poor resolution. The first reason, owing to the large geometrical aberrations, will be analyzed in chapter 3 of this thesis. The other reason could have been the over-dose of ion radiation. UVII HS is a chemically amplified resist with high sensitivity to photon, electron and ion radiations. The required dose to expose a UVII HS resist is only 0.15 $\mu C/cm^2$ for 75 keV H^+. The actual dose that was used in the experiment was 82 $\mu C/cm^2$, which was 500 times higher than the threshold dose sensitivity. Even though the aperture images could not be individually

separated, the distance between the two outmost aperture images had been reduced noticeably from 6 mm on the mask to about 0.64 mm on the resist. This result indicated a demagnification ratio of 9.4.

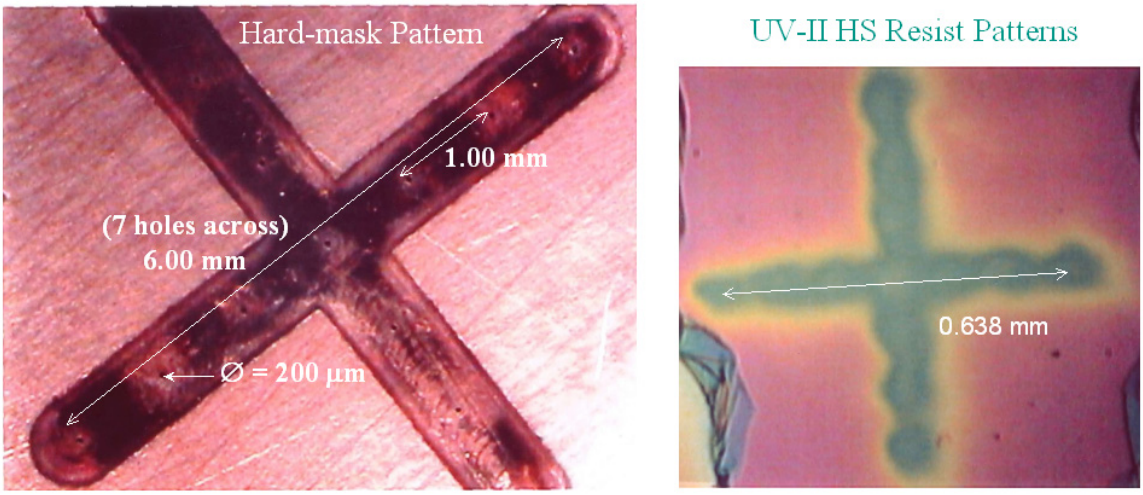

Figure 2.11. Copper mask with 13 apertures drilled in the cross dent (left) and the ion beam exposure result on UV-II HS resist (right). [1]

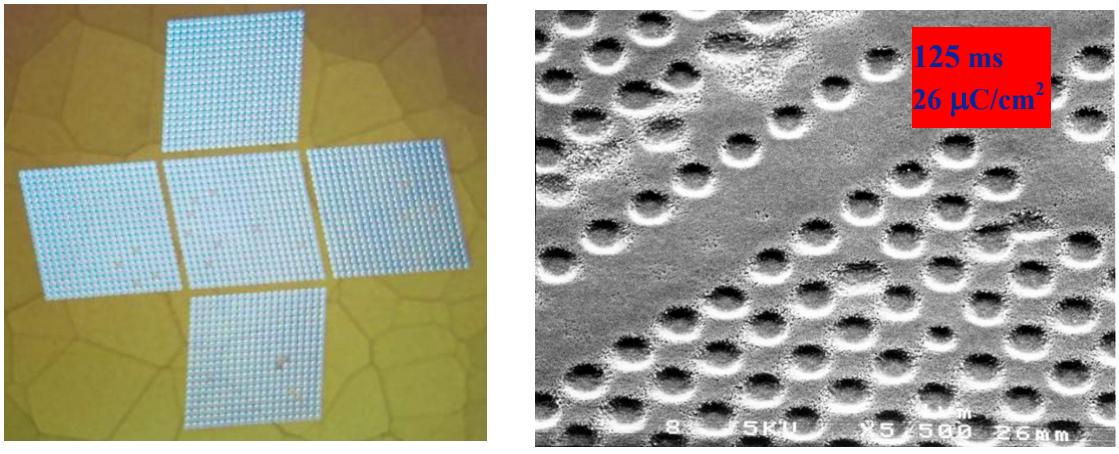

Figure 2.12. The silicon stencil mask (left) and the PMMA exposure result (right). The thickness of the silicon membrane is 66 μm. The average diameter of the apertures on the mask is 7.75 μm. The diameter of the aperture image on the resist is about 1.5 μm. The exposure ion dose is 26 μC/cm^2. [1]

Ngo also tested a microfabricated stencil mask in the MMRL (fig. 2.12). The average diameter of the apertures on the mask was 7.75 μm. If the diameter could be reduced by a magnitude of 10, sub-micro apertures could be printed on a PMMA resist. But the actual diameter of the aperture images on the PMMA resist was about 1.5 μm. The thickness of the mask membrane was 66 μm. Therefore the aspect ratio of the apertures in the mask was 8.5, which was much higher than that of the copper mask shown in fig. 2.11. The resolution was clearly superior to the result obtained on the copper mask, but still far from the targeted resolution.

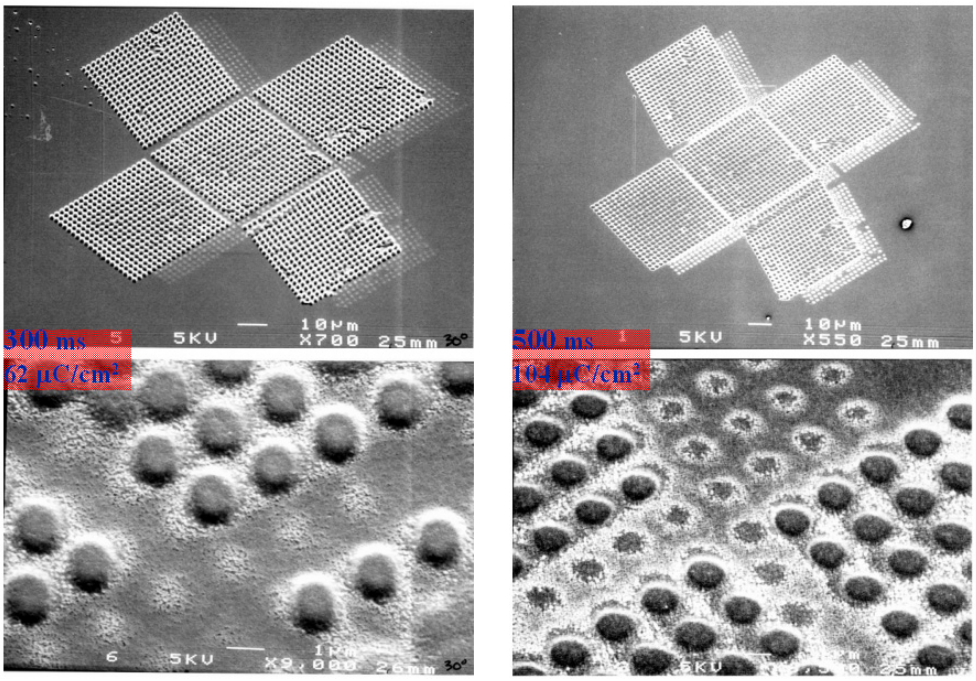

Figure 2.13. Double patterned image at different dose. Upper images are taken at low magnification. Lower image are enlarged view of the upper image.[1]

A double-patterned-image was also discovered when hydrogen was used to generate the plasma (fig. 2.13). The mechanism of the double-patterning was discussed

by Vinh V. Ngo in his Ph. D. thesis[1]. He successfully pointed out that the earth's magnetic field acted as a deflection field to the hydrogen ion beams, which may have H^+, H_2^+ or even H_3^+ species. Since the species have different charge to mass ratios, they will be deflected to different positions and form multiple images. The double-patterned images are formed by H^+ and H_2^+ ions.

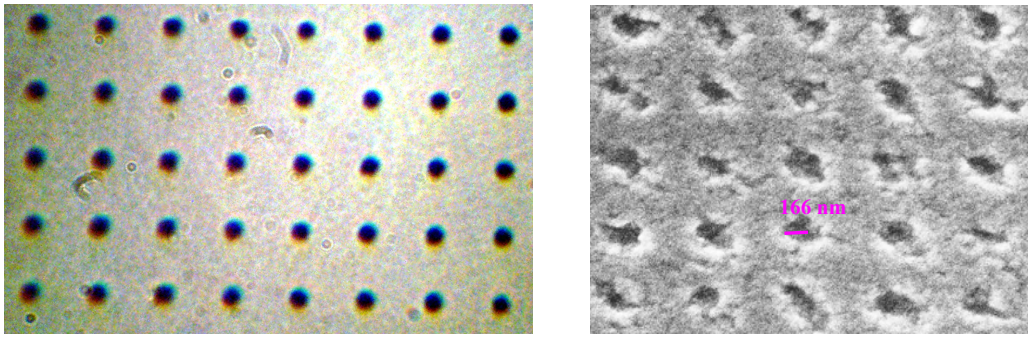

Figure 2.14. An IBM aperture-array mask and the hydrogen ion beam exposure image on UVII HS resist. The diameter of the aperture on the mask is about 1.0 μm.[1]

The exposure result in fig. 2.14 was carried out with an aperture-array mask provided by the IBM Almaden research center. The apertures on the mask have an average diameter of 1.0 μm and an aspect ratio of 20:1. The aspect ratio is higher than that of the masks in fig. 2.12 and 2.13 meaning the extracted ion beam would have a relatively small half angle. But only very rough patterns as small as 166 nm could be observed on the exposed UVII HS resist. The images were too coarse to be of any use. The exposure results in fig. 2.12~2.14 show that the resolution capability on the original MMRL system failed to meet the design target. The resolution was also much larger than

V. V. Ngo's simulation results (6 nm across 1.0×1.0 mm^2 exposure field).[5] This discrepancy will be accounted for in Chapter 3 of the current thesis.

2.6 Beam switching experiment with mechanically drilled pattern generator

A pattern generator is required for MMRL to operate in a maskless mode. A proof-of-concept ion beam switching experiment was carried out on a mechanically machined pattern generator by V. V. Ngo.[1,3,6] The schematic of a 9-hole pattern generator is shown on the left side graph of fig. 2.15. The diameter of the apertures is 50 μm. The extracted ion current versus the biasing voltage on a mechanically drilled single-aperture (300 μm in diameter) switching device is presented in the right side graph of fig. 2.15. From this result, using a biasing voltage as low as 2 volts is sufficient enough to turn off almost all of the current. This also confirms that the beam energy spread is 2 volts or less.

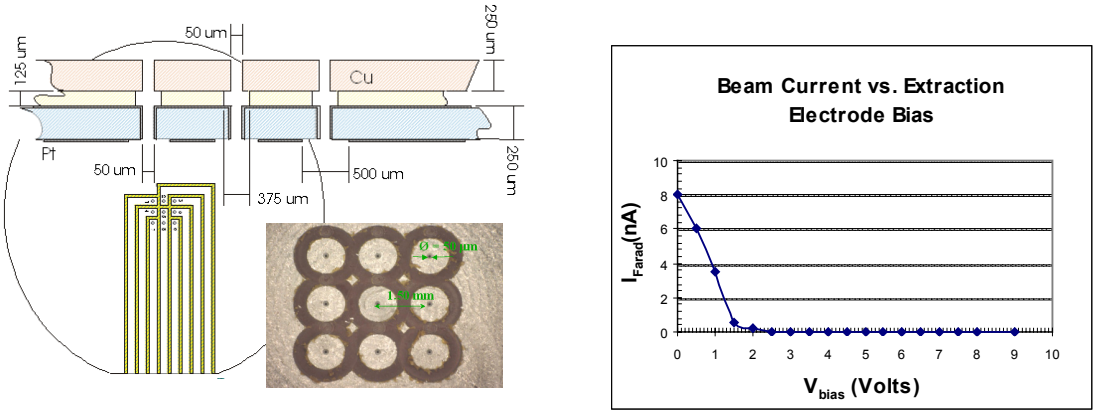

Figure 2.15. Mechanically drilled 9-aperture pattern generator (left) and the beam switching result on a single-aperture (300 μm) switching device (right).[1,3,6]

2.7 Summary

The MMRL system structure has been briefly introduced in this chapter. In order to automatically switch the multiple ion-beam-lets on and off, the automation control system, including the software and hardware, has been updated in the current thesis work. Previous resist exposure experiments and beam switching experiments with a mechanically machined switching device were also discussed.

The resist exposure result on the prototype MMRL system has demonstrated the 10X reduction ratio . But the observed resolution capability was found to be much worse than what the simulation predicted. V. V. Ngo attributed the poor resolution to the rough inner wall profile of the apertures, short noise effect and contamination during resist coating and developing processes.[1] Analysis in Chapter 3 of the current thesis will show that the actual reasons for the poor resolution lie in the ion optics system in the prototype MMRL.

The resolution of the MMRL system must be significantly improved in order to become a potential candidate as one of the next generation lithography (NGL) approaches. Chapter 3 will analyze the optics of the MMRL system in detail. The possible interferences that may cause deviations from the ideal scenario will also be investigated. Experimental results presented in Chapter 3 will show that the result can be successfully improved to 50 nm.

V. V. Ngo has successfully demonstrated the ion beam switching on a mechanically machined single-aperture pattern generator with a diameter of 300 μm. Further reduction in the size of the aperture requires a microfabrication process. Microfabricated pattern generators with switchable apertures of 1.0 μm in diameter, have

been fabricated in the Microfabrication Laboratory at UC-Berkeley and tested in the MMRL. This work will be further elaborated in chapter 4.

Reference:

[1] V.V. Ngo, "Experimental demonstration of a Prototype Maskless Micro-ion-beam Reduction Lithography System",Ph.D. Thesis, Unversity of California 2005.

[2] Yvette Lee, "Production of Low Axial Energy Spread Ion Beams with Multicusp Sources", University of California, 1998.

[3] V.V. Ngo, B. Akker, K. N. Leung et al., "Demonstrations of electronic pattern switching and 10X pattern demagnification in a maskless microion-beam reduction lithography system ", Journal of Vacuum Science and Technology B **21** (6), 2297 (2003).

[4] W. H. Bruenger, M. Torkler, and K. N. Leung, "Resolution improvement of Ion Projector with Low Energy Spread Multicusp Ion Source", Microelectronic Engineering **46**, 477 (1999).

[5] V.V. Ngo, W. Barletta, R. Gough et al., "Maskless Micro-ion-beam reduction lithography", Journal of Vacuum Science and Technology B **17** (6), 2783 (1999).

Chapter 3

Optics and throughput analysis for MMRL

Optics directly limits the resolution and throughput of charged particle lithography systems. MMRL was designed for lithography nodes under 50 nm. But the actual resolution observed on MMRL was much worse than the simulation result obtained by Ngo. V.V.,[1] as discussed in chapter 2. The ion optics column for MMRL was simulated on a commercially available charged-particle optics design software from MEBS™,[2] which has been used to design many high-resolution charged-particle imaging or lithography systems. The discrepancy between the simulation and the experimental results will be explored in this chapter. A more accurate optics model will be used to calculate the actual optics performance for the prototype MMRL system. Solutions to improve the resolution capability will be discussed. Features as small as 50 nm have been experimentally observed after the optics column was optimized and the electromagnetic interference was reduced.

Charged particle lithography has the advantage of high resolution over the traditional optical lithography. But there is a trade-off between the resolution and the throughput for charged particle lithography. Interactions between charged particles limit the maximum allowable current in MMRL, which determines the total exposure time during lithographic processes. In the mean time, the inherently large shaped beam aberrations' coefficients of the charged particle optics limit the attainable field size. Small field size will substantially increase the time for the mechanical stage to scan or step across the whole area of wafers during lithography. All these factors directly affect the throughput capability of MMRL. These issues will also be investigated in the current chapter.

3.1 Introduction to charged particle optics

3.1.1 Comparison of light optics and charged particle optics

As discussed in chapter 1, the resolution capability of the traditional optical projection lithography systems was determined by the diffraction nature of light, which is governed by the Rayleigh's criterion:

$$\text{Resolution} = K_1 \frac{\lambda}{n \cdot Sin(\theta)} = K_1 \frac{\lambda}{n \cdot NA} \tag{3-1}$$

It's easy to see that better resolution can be obtained at shorter wavelength. De Broglie believed that every material has its wave nature. Disregarding the relativistic effect, the wavelength of particles with mass m and energy E can be calculated as:

$$\lambda = \frac{h}{p} = \frac{h}{mv} = \frac{h}{\sqrt{2mE}} \tag{3-2}$$

For a 75 keV electron, the corresponding wavelength is 4.3×10^{-3} nm. A H^+ ion with energy of 75 keV has a wavelength of 1.045×10^{-4} nm. A helium ion is four times heavier than a hydrogen ion, so the wavelength of a 75 keV He^+ ion is as short as 5.23×10^{-5} nm. Even if NA is as low as 10^{-5}, the diffraction limited resolution for 75 keV He^+ ion is still as small as 2.5 nm (k=0.2 and n =1). This means that the diffraction effect in a projection optics can be overcome by switching the imaging medium from light to charged particles.

Another factor affecting the resolution is the lens aberrations. Optical lens is made of materials with uniform diffraction coefficient. It has well defined boundary that can diffract the incident light to certain angles. Optical lens materials can be fabricated into shapes with virtually arbitrary curvatures. And there are many choices of lens materials and coatings, which have different diffraction properties to light. All these properties make it much easier to design a light optics column with most of the major aberrations corrected. As a result, the latest optical lithography tool can expose a field as large as $26\times33mm^2$ with a NA as large as 0.92.

However, charged particle optics has to use an electrostatic lens or a magnetic lens. Currently, there is no applicable way of designing an electrostatic or magnetic lens with abruptly changed electric field or magnetic flux distribution. And it is even very difficult to design a divergent (negative) lens element in charged particle optics for required situations. All these factors make it very difficult to correct the aberrations in charged particle optics. Even though diffraction effect is not significant for charged particle optics in most situations, the inherently large aberrations' coefficients directly limit the attainable field size and the beam half angle (NA). Consequently, charged

particle optics has to work under the conditions of a very low NA and a very small field size to reduce the lens aberrations, which will substantially sacrifice the throughput capability. On the other hand, small NA has the benefit of large depth of focus (DOF). In order to improve the resolution for the traditional optical lithography, the wavelength of the light must be decreased and the lens NA must be increased based on equation (3-1), which will decrease the depth of field according to equation (3-3), and shrink the process window.

$$\text{DOF}=\frac{K_2}{2}\frac{\lambda}{n\cdot\left(1-Cos(\theta)\right)}=K_2\frac{\lambda}{n\cdot(NA)^2} \tag{3-3}$$

Charged particle lithography can have much higher process latitude, which is partially because of the large DOF from the small NA.

Another difference is that charged particles can interact with each other. Charge interactions can deteriorate resolution at high current condition. In order to obtain a throughput to be competitive with the traditional optical lithography, it is inevitable for electron or ion beam lithography systems to work at a total current much higher than that of SEM or FIB, which may result in a high space charge effect or strong stochastic charge interactions. It is imperative to find revolutionary ideas to minimize the charged particle interactions in order to improve the throughput of the charged particle systems.

3.1.2 Aberrations in optics

The property of a lens has linear quantities such as focal length, position of foci, principle planes and nodal planes. But besides these low order terms, there exist perturbations to the imaging property of the lens. The deviations from the perfect images

are called aberrations. The definition of aberrations in charged particle optics is very similar with light optics. The third-order geometrical aberrations of round lenses can be written as:[3]

$$\Delta u_i = C r_a^2 u_a \qquad \text{(Spherical aberration)} \qquad (3\text{-}4)$$

$$+ 2(K + ik) r_a^2 u_o + (K - ik) u_a^2 u_o^* \qquad \text{(COMA)} \qquad (3\text{-}5)$$

$$+ (A + ia) u_o^2 u_a^* \qquad \text{(Astigmatism)} \qquad (3\text{-}6)$$

$$+ F r_o^2 u_a \qquad \text{(Field curvature)} \qquad (3\text{-}7)$$

$$+ (D + id) r_o^2 u_o \qquad \text{(Distortion)} \qquad (3\text{-}8)$$

$r_o^2 := x_o^2 + y_o^2 = u_o u_o^*$. Here r_o, x_o, y_o, u_o, u_o^* are the spatial coordinates on the object plane. And $r_a^2 := x_a^2 + y_a^2 = u_a u_a^*$. Correspondingly, r_a, x_a, y_a, u_a, u_a^* are the beam coordinates on the aperture plane, which measure the beam angles.

3.1.2.1 Spherical aberration

The formation of spherical aberration is because the rays far from the axis are focused more strongly than those closer to it. As a result, the peripheral rays are focused in front of the Gaussian focus and the paraxial rays are focused further away. The circle of least confusion has the minimum diameter and corresponds to the best possible focus in the presence of spherical aberration (fig. 3.1). From equation 3-4, spherical aberration is proportional to the third power of the aperture coordinates, e.g. beam half angle. And it is of the greatest importance in the first (objective) lens of magnifying systems and in the final lens of probe-forming systems.

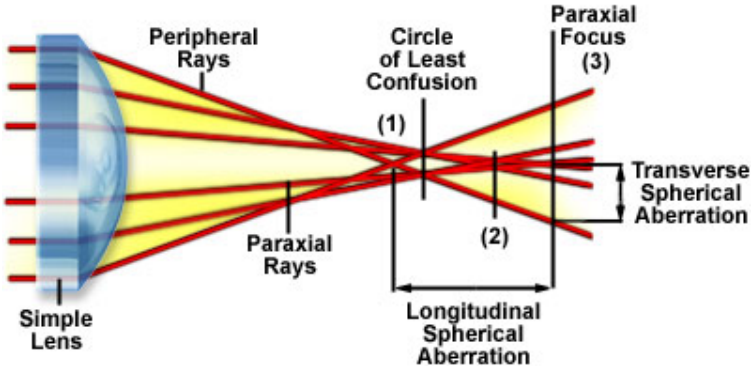

Figure 3.1. Formation and definition of spherical aberration in round lens. Image courtesy of Olympus.

3.1.2.2 Coma aberration

For objective and probe-forming optics, the coma might be the next most important aberration after the spherical aberration if the rays are inclined to the axis at a relative steep angle[3.1]. Coma is similar to the spherical aberrations, but it is mainly encountered with off-axis rays. Coma is proportional to the first order of object off-axis position and the second order of the aperture angle. If off-axis incident rays that arrive on lens at different off-axis positions are focused to different heights, Coma aberration is formed. The diameter of the spot increases with the incident angle. As a result, comet-like shape will be formed on the image plane (fig. 3.2).

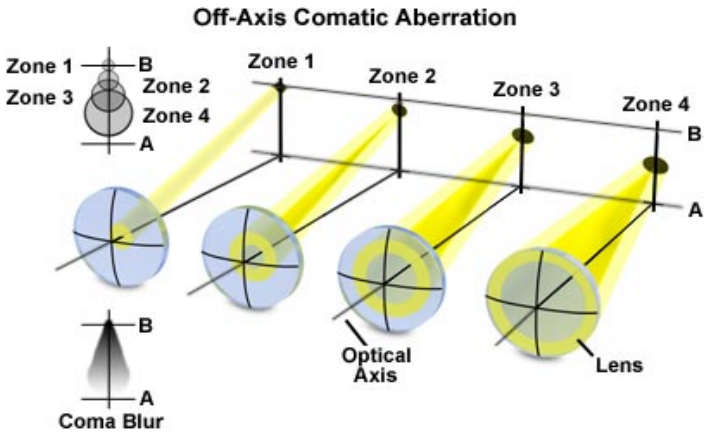

Figure 3.2. The mechanism of coma aberration formation. Image courtesy of Olympus

3.1.2.3 Astigmatism and field curvature

Astigmatism and field curvature are usually the most important image blurs in charged particle projection optics because of the second order dependence to the object's spatial coordinates. They also change linearly with the beam half angle. When off-axis rays on the sagittal plane and the tangential plane are focused on different focal positions, astigmatism aberration will be formed, as shown in fig. 3.3.

When rays are focused through a curved lens, the image plane produced by the lens will also be a curved surface (fig. 3.4). But usually the object and the image planes are flat. The curved Petzval surface will create an image blur on a flat image plane. This is called field curvature aberration. Astigmatism and field curvature aberration can be dynamically corrected in probe beam systems (small-beam direct-write systems) or partially correct in projection systems with variable axis, such as PREVAIL. But they can't be corrected in large-field charged-particle projection systems through conventional round focusing lenses. Consequently, these two aberrations directly limit the attainable field size in electron or ion beam projection lithography systems.

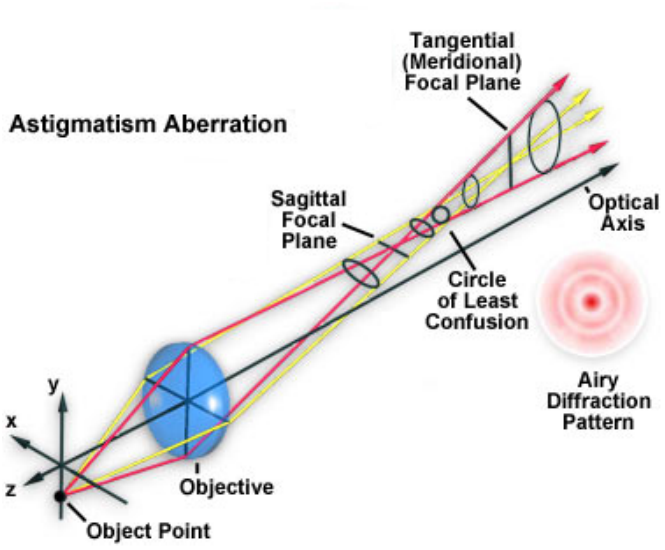

Figure 3.3. Astigmatism aberration. Image courtesy of Olympus

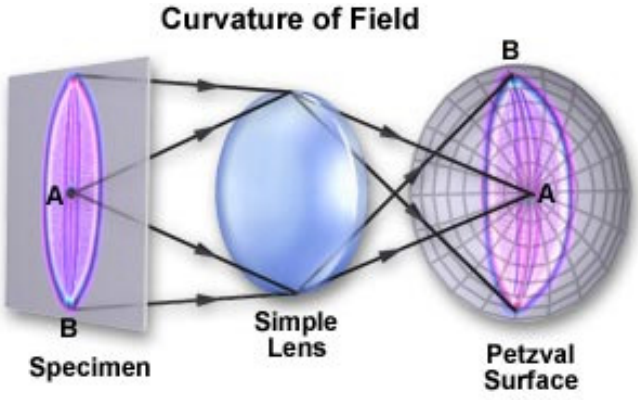

Figure 3.4. Field curvature aberration. Image courtesy of Olympus.

3.1.2.4 Distortion

Distortion aberration is of the most importance to large field projector systems. It is proportional to the third order of the object size according to equation 3-8. Unlike other aberrations, distortion does not cause image blur but merely destroy the proportionality between the image and the object coordinates.[3] If d=0 and D>0 in equation 3-8, pincushion distortion exists in images (fig. 3.5 (b)). If d=0 and D<0, the aberration is called barrel distortion (fig. 3.5 (c)). Pincushion and barrel distortions are isotropic. They are created when lens magnification is dependent on off-axis positions. Magnetic lenses rely on rotating the incoming electron or ion to generate focusing force. If the rotation angle changes with the off-axis position, it will create a special anisotropic distortion: spiral distortion (fig. 3.5 (d)). Spiral distortion only exists in magnetic lenses.

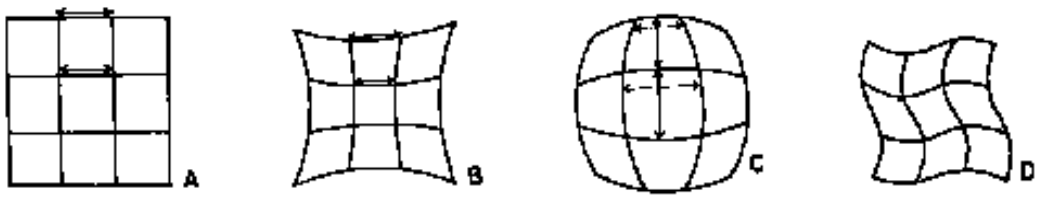

Figure 3.5. Distortion aberration. (A) Undistorted image; (B) Pincushion distortion; (C) Barrel distortion; (D) Spiral distortion.[1]

3.1.2.5 Chromatic aberration

The focusing power of an electrostatic or a magnetic lens depends on the energy of the incoming charged particles. Electron or ion sources can't produce exactly mono-energetic beams. And there are always some fluctuations in high voltage and current supplies for lenses. The energy spread will be broadened when charged particles pass through thin materials, such as a membrane mask used in SCAPEL. The fluctuation of the beam energy will create another image blur---chromatic aberration, which has an axial component (axial chromatic aberration) and a radial component (shaped-beam chromatic aberration). Axial chromatic aberration is proportional to the product of $\alpha \cdot \frac{\Delta V}{V}$, here α is the beam angle, ΔV is the energy spread and V is the beam energy. Shaped-beam chromatic aberration changes linearly with $r \cdot \frac{\Delta V}{V}$, r is the off-axis distance of the beam.

3.1.3 Charged particle optics design

Charged particle optics column based on electrostatic and magnetic lenses has been studied for over a century. With more and more powerful computers readily available, complicated electrostatic or magnetic lens column can be simulated with a PC nowadays. Eric Munro and Xieqing Zhu have pioneered in the computer aided charged particle optics design since 1970s.[4] Their latest charged-particle optics design software

package has been widely used in designing many high-resolution electron and ion beam imaging or lithography systems. The first step in their method is to calculate the magnetic and electrostatic field distribution with the first- or second-order finite element methods (FOFEM and SOFEM), the finite difference method (FDM) and the charge density method (CDM). Then the fields in the lens and the deflector are expended in series as powers of the off-axis distance. These field expansions are then substituted into ray equations. By excluding different orders of terms, first-order paraxial properties, third-order and fifth-order aberrations can be calculated.[5]

The first order optical properties are obtained by evaluating four paraxial rays: focusing ray, field ray, main-field deflection ray and subfield deflection ray. These paraxial rays have unit slope, position and deflection excitations. First order imaging and deflection properties can be extracted from the values of these rays at the image plane. The third-order/fifth-order aberrations can be calculated when third/fifth order expansions are included into the ray equation. And it can be solved through the methods of variation of parameters to yield certain aberrations in the form of an integral.[5] An alternative way to obtain the aberration coefficients is direct ray-tracing as long as the computation accuracy is high enough to obtain a reliable result.[6]

3.2 Re-evaluate the performance of the original MMRL optics

Figure 3.6 is the simulated aberration spot diagram obtained by V. V. Ngo using the MEBS simulation package.[7] The whole spot diagram has 1.0×1.0 mm^2 field of view on the image plane. Since the reduction ratio is 10, the object field size is about 10×10

mm^2. This is much larger than the 1.0×1.0 mm^2 object field size for PREVAIL and SCAPEL. The simulated total beam blur is less than 6 nm at the corner of the exposure field. In order to obtain such a low aberration across such a large field size, the beam half angle on image plane was set to be as small as 10^{-5}. The energy spread used in the simulation is 1.0 volt ripple on a final energy of 75 kV.

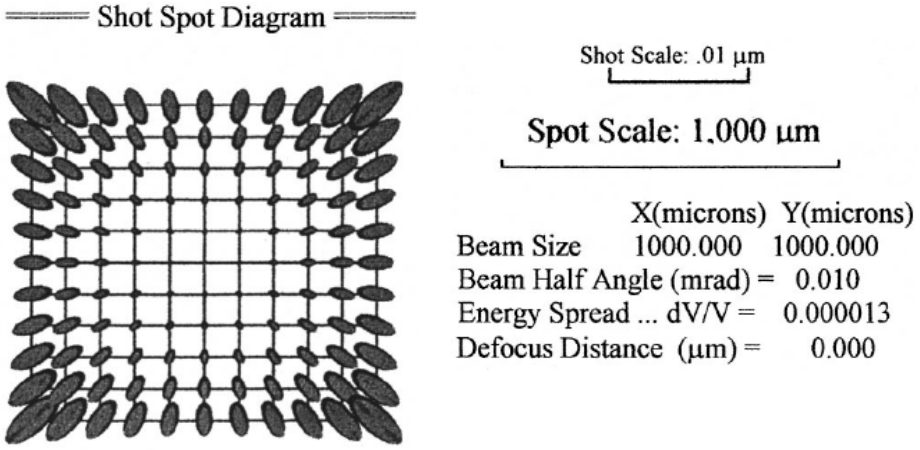

Figure 3.6. Blur spot diagram on the image plane for MMRL optics column simulated with MEBS optics design software.[7]

A beam blur as small as 6 nm across a 1.0×1.0 mm^2 image field was obtained in V. V. Ngo's simulation. However, the resist exposure experiments revealed that the actual beam blur is several orders of magnitude higher than the simulation result. After a thorough analysis to the optics model used in Ngo's simulation and the actual optics column in MMRL, it is found that the discrepancy is caused by the oversimplification to the optics model and some errors in the parameters used in the simulation. These issues will be discussed in the following several sub-sections. An improved simulation result will also be presented.

3.2.1 Influence from the initial ion energy

The initial ion energy on the object plane is set to be 30 eV during the design of the original MMRL optics column. But V. V. Ngo has also claimed that ion beam can be totally shut-off by applying a positive biasing voltage of only 2 volt onto a mechanically drilled switching device.[8] It indicates that the initial ion beam energy might be just around 2 eV, which is 15 times lower than the value used in the simulation of the optics column. Such a large difference in initial ion energy can change the simulation result a lot.

The aberrations of the MMRL optical column at different initial ion energy are plotted in fig. 3.7. The distortion is negligible when the initial beam energy is 30eV, because the original MMRL optics column has been optimized to work in telecentric image condition at this energy. Telecentric image condition can automatically cancel distortion and shaped-beam chromatic aberration. However, when the initial energy changes, ions will not follow the distortion-corrected ray path any more. Thus, the distortion and the shaped-beam chromatic aberration increase extremely fast when the initial ion energy decreases from 30 eV. The shaped-beam chromatic aberrations will become the dominant source of image blur at initial ion energy below 10 eV. And it can be as large as 1.0 μm at the edge of a 1.0×1.0 mm^2 image field when the initial ion energy is as low as 3 eV. On the other hand, the shaped-beam chromatic aberration is proportional to the first power of field size. It is still possible to obtain a resolution better than 100 nm if the off-axis distance is less than 0.1 mm on the image plane. But such a small exposure field will greatly reduce the throughput capability.

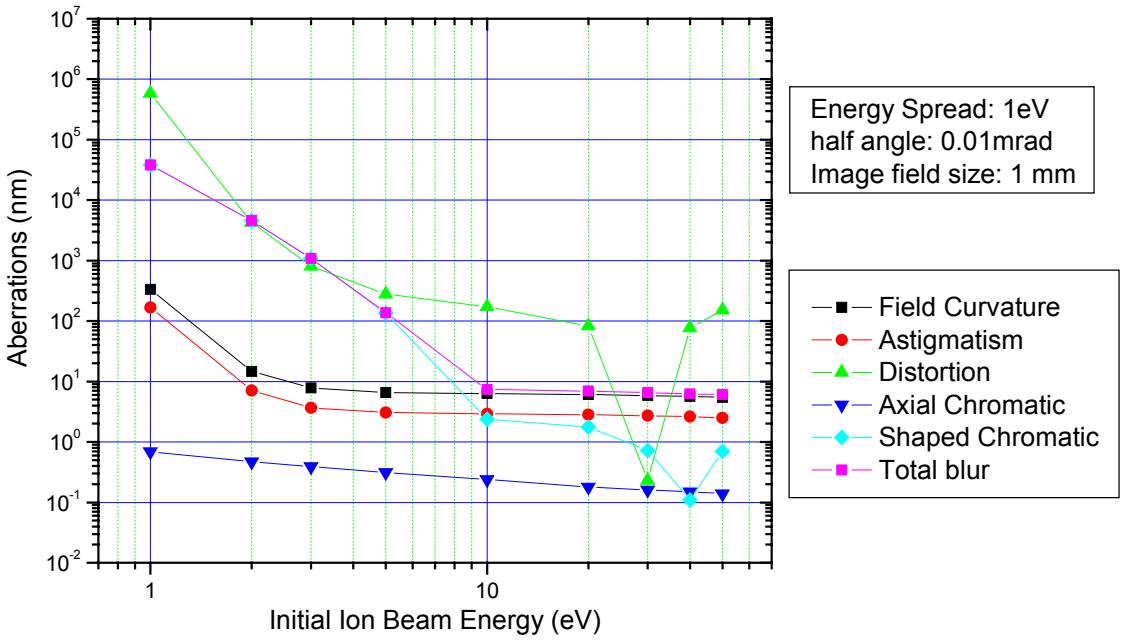

Figure. 3.7 Aberrations versus the initial ion beam energy.

If the initial ion energy is actually 2 eV, the MMRL optics column has to be redesigned to obtain telecentric image condition for much lower initial ion energy. The initial ion energy is mainly determined by the plasma potential inside the ion source. Magnetic multi-cusp field can lower the plasma potential by confining electrons inside plasma. Low plasma potential relaxes the requirement on pattern generator design and fabrication, by decreasing the switching voltage, and by protecting the pattern generator from damages caused by plasma heating and ion sputtering. These issues will be explained with more details in the next chapter. However, the plasma potential may change with the mass of ions, the plasma density, the neutral gas pressure and the input rf power. Any variation to these parameters may cause the shift of the initial ion energy. As

a result, the ion source of the MMRL system must work at a very stable condition. It must be able to provide enough ion current to obtain an acceptable throughput, and a stable and low plasma potential to maintain a constant optics condition and to protect the pattern generator. After the initial ion energy is experimentally determined at this condition, the MMRL optics column should be optimized according to the accurate initial ion energy.

3.2.2 Beam half angle of the original MMRL optics column

The beam half angle at the image plane was set to be 0.01 mrad (NA=10^{-5}) in V. V. Ngo's simulation. The ratio between the beam half angle at the image plane (α_i) and that at the object plane (α_o) is called the angular magnification (M_α). The relation between the size magnification (M) and the angular magnification (M_α) is expressed in the following equation:

$$M_\alpha \cdot M = \sqrt{V_0 / V_i} \tag{3-9}$$

Where V_o and V_i are the electrostatic potential at the object plane and the image plane respectively. This relation can be easily derived from the Lagrange-Helmholtz theorem.

$$d_0 \cdot \alpha_0 \cdot \sqrt{V_0} = d_i \cdot \alpha_i \cdot \sqrt{V_i} \tag{3-10}$$

Here d_o and d_i are the object size and the image size. V_i is 75,000 volt. Based on equation (3-9), the angular magnification will be 0.2 if V_o is 30 volt. If α_i=10^{-5} sr, as

used by Vinh V. Ngo, α_o should be 5×10^{-5} sr. If V_o is only 2 volt, the angular magnification will be 0.0516. Then α_o still needs to be less than 1.9×10^{-4} sr in order for α_i to be equal to 10^{-5} sr on the image plane.

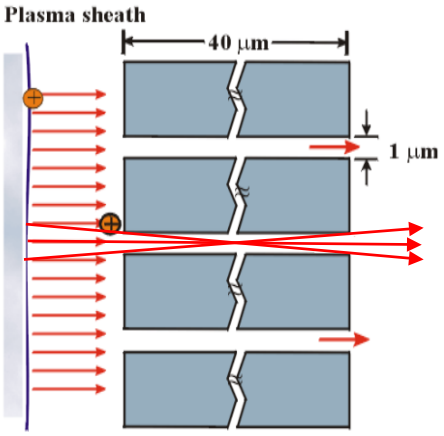

Figure 3.8. MMRL optics column relies on high aspect ratio aperture to obtain low beam half angle on the object plane

The object-side half angle (α_o) in the original MMRL system is mainly determined by the ion temperature, the plasma potential and the aspect ratio of the apertures in the mask or the pattern generator (fig. 3.8). When ions drift out from the plasma sheath, they will be accelerated by the potential difference across the sheath. But ions may have certain transverse velocity originating from the ion temperature. The transverse velocity will cause certain angular distribution to the ions. Fortunately, the ion temperature inside plasma is usually much lower than the electron temperature because of the huge difference in mass between the two particles in plasma.

Suppose the incoming ions have room temperature (300K or 0.025 eV) and the plasma potential is 30 volt, the transverse half angle on the plasma electrode surface, originating from the ion temperature, will be as large as 29 mrad. Actually, the plasma

potential in the ion source might be as low as 2 eV. Then the transverse half angle of ions, caused by the ion temperature, will increase to 112 mrad. The plasma sheath can be regarded as a positively charged region. Even though the ion density in the plasma sheath is lower than that of the plasma bulk, the stochastic ion-ion interactions can't be ignored because of the low ion energy in plasma sheath. The charge interactions within the plasma sheath may further increase the transverse angle of the extracted ions.

The original MMRL system solely relies on the high aspect ratio mask to collimate the incoming ions (fig. 3.8). Even if the mask aspect ratio can be made as high as 40:1, the object side beam half angle will still be as large as 25 mrad. This estimation has neglected the effect of the charge interactions inside the aperture channel and the scattering of the aperture wall. Actually, the openings in the mask or the pattern generator can cause perturbation to the electric field on the column side (fig. 3.9). The curved electric field will focus the incoming low energy ions. Even if the incoming ions are perfectly parallel, the cured electric field will increase the beam half angle by 17.5 mrad. This angle is already 91 times larger than the required object-side half angle (1.9×10^{-4} sr) in order to obtain an image-side half angle of 0.01 mrad (NA=10^{-5}) in Ngo's simulation.

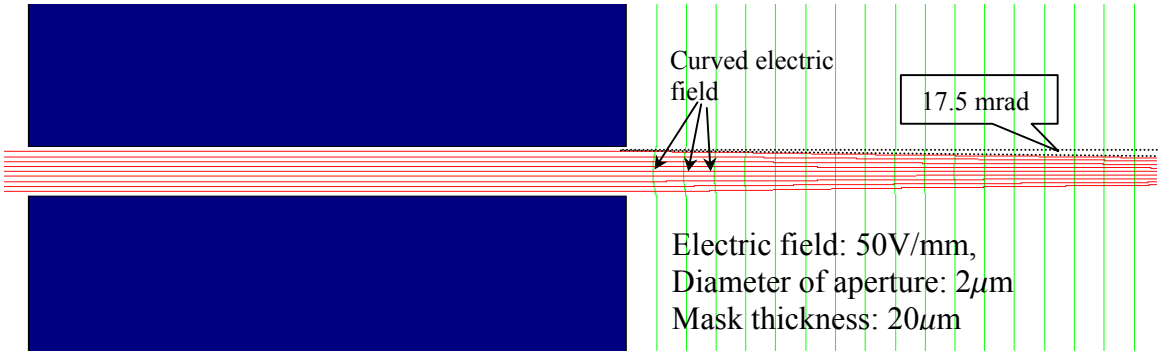

Figure 3.9 The curved electric field around the aperture will focus the incoming low energy ions and increase the object-side beam half angle.

The electric field around the surface of the mask or pattern generator is as low as 50 V/mm in the current MMRL optics column. This is an extremely low electric field for cathode or anode lens. It will greatly increase the charge interactions because the ions can't be accelerated to a high velocity within a short distance. The charged particle interactions will be discussed with more detail in section 3.5. In addition, the switching voltages applied to the different apertures on the pattern generator will generate a transverse electric field on the surface, which will deflect the neighboring ion beam-lets. This effect is called the cross-talking of the pattern generator. Generally speaking, high electric field in the axial direction (perpendicular to the mask or pattern generator plane) is more desirable to reduce the charge interactions and the cross-talking effect. On the other hand, it will also increase the curved electric field strength around the openings on the mask or the pattern generator and greatly increase the beam half angles. Even if the electric field around the pattern generator is as low as 50 V/mm, the perturbed electric field can still increase the beam half angle by 17.5 mrad.

The analysis in the above several paragraphs indicates that it is impossible to obtain an image-side beam half angle as low as 10^{-5} in the original MMRL optics column. The NA used in Vinh V. Ngo's simulation is much smaller than the actual value. This could be another reason for the poor resolution observed in the experiments.

3.2.3 Effect of the beam half angle to aberrations

The analysis in the previous section shows that it is impossible to obtain 10^{-5} numerical aperture in the original MMRL optics column. Large beam half angle will increase spherical aberration ($\propto\alpha^3$), COMA ($\propto\alpha^2$), field curvature ($\propto\alpha$), astigmatism ($\propto\alpha$) and axial chromatic aberration ($\propto\alpha$). Aberrations v.s. the image-side beam half angle are calculated in fig. 3.10 when the initial ion energy is 2 eV. Due to the violation of the telecentric optics condition, the distortion and the shaped-beam chromatic aberration at the edge of the 1 mm exposure field will be increased to about 4 μm in fig. 3.10. Since these two aberrations don't change with beam half angle, they become the major aberrations at small beam half angles. Fortunately, these two aberrations decrease with field size. It is still possible to obtain a resolution less than 100 nm when a small exposure field is aligned with the column axis and the beam half angle is small. Other aberrations don't change too much with the initial ion energy. But they increase very rapidly with the beam half angle. Spherical aberration and COMA become the dominating sources of beam blur when the image side beam half angle was increased to over 30 mrad. Because the spherical aberration doesn't change with off-axis distance, it will not decrease in the center of the field. Field curvature and astigmatism are the most important source of aberrations in medium range of NA. These two aberrations are usually the most important aberrations for most charged particle projection lithography systems. But they decrease very fast with the size of the exposure field. So they can be minimized at a small field size. The above analysis indicates that the resolution of the MMRL system can be improved by decreasing the beam half angle.

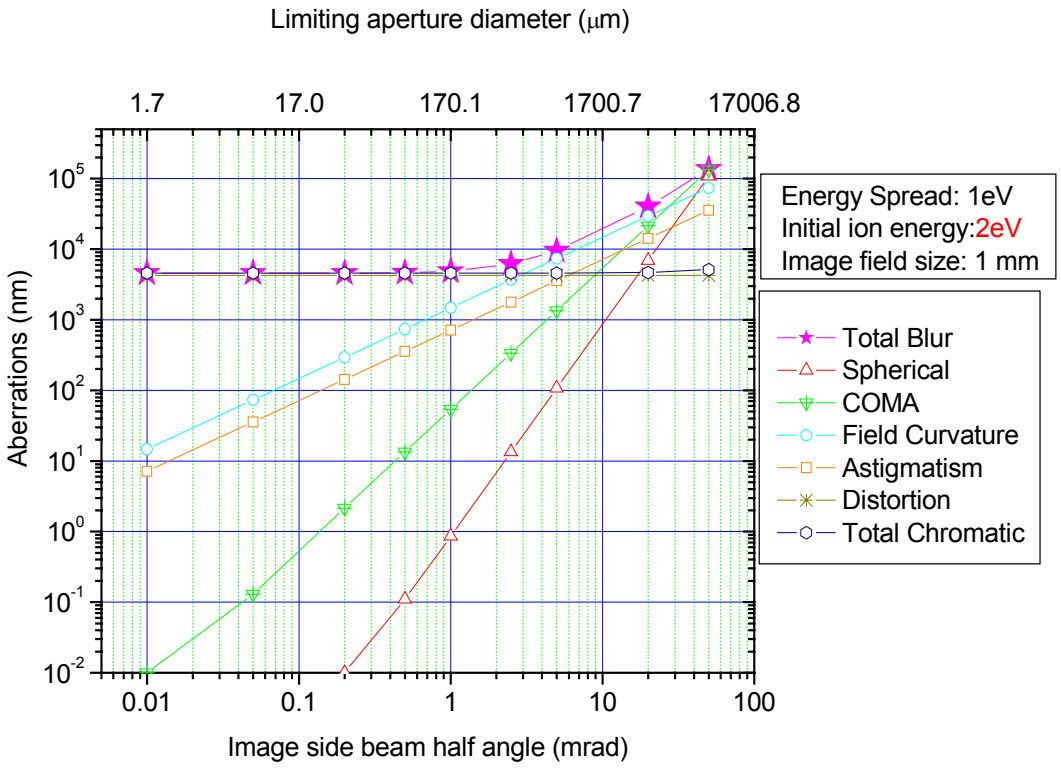

Figure 3.10. Aberrations versus the image side beam half angle when the initial ion energy is set to be 2 eV.

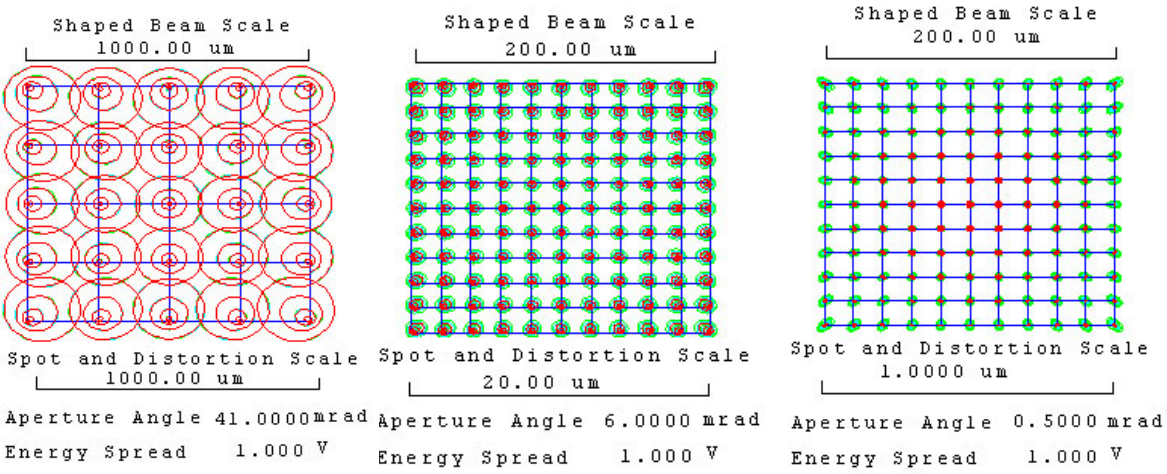

Figure 3.11. The aberrations' spot diagrams at three different beam half angles.

The aberrations' spot diagrams for three different beam half angles have been plotted in fig. 3-11. The image-side beam half angle in the left side graph of fig. 3-11 is 41 mrad. The shaped beam size (whole exposure field) in this plot is 1.0 mm. It is easy to see that the resolution is worse than 200 μm over the whole exposure field. Because the blur is dominated by spherical aberration, it doesn't change with off-axis position. This result agrees with the exposure image shown in fig. 2-11, where the aspect ratio of the mask in the experiment is only 1.25:1, corresponding to an image-side beam half angle of 41 mrad. The beam half angle in the middle plot of fig. 3.11 is 6 mrad. The beam blur is about 1.2 μm within the whole 200 μm exposure field. It agrees very well with the resist exposure result in fig. 2-12, which was obtained on a microfabricated mask with an aspect ratio of 8.5:1, corresponding to an image-side beam half angle of 6 mrad. When the beam half angle is decreased to 0.5 mrad in the right side graph of fig. 3-11, the resolution will be improved to about 30 nm in the center of the exposure field. Yet, the resolution at the edge of the exposure field is worse than that of the center. This means that the shaped beam aberrations can not be ignored at this condition. It also shows that the resolution can be substantially improved by decreasing the beam half angle.

It will be interesting to evaluate the optics of the MMRL system at the telecentric condition. Fig 3.1 shows the computed aberrations at the edge of a 1.0 mm exposure field when the initial ion energy is set to be 30 eV. The distortion and the shaped beam chromatic aberration have been almost totally eliminated. Since the shaped beam aberrations are minimized at the telecentric optics condition, the acceptable image field size will be greatly increased.

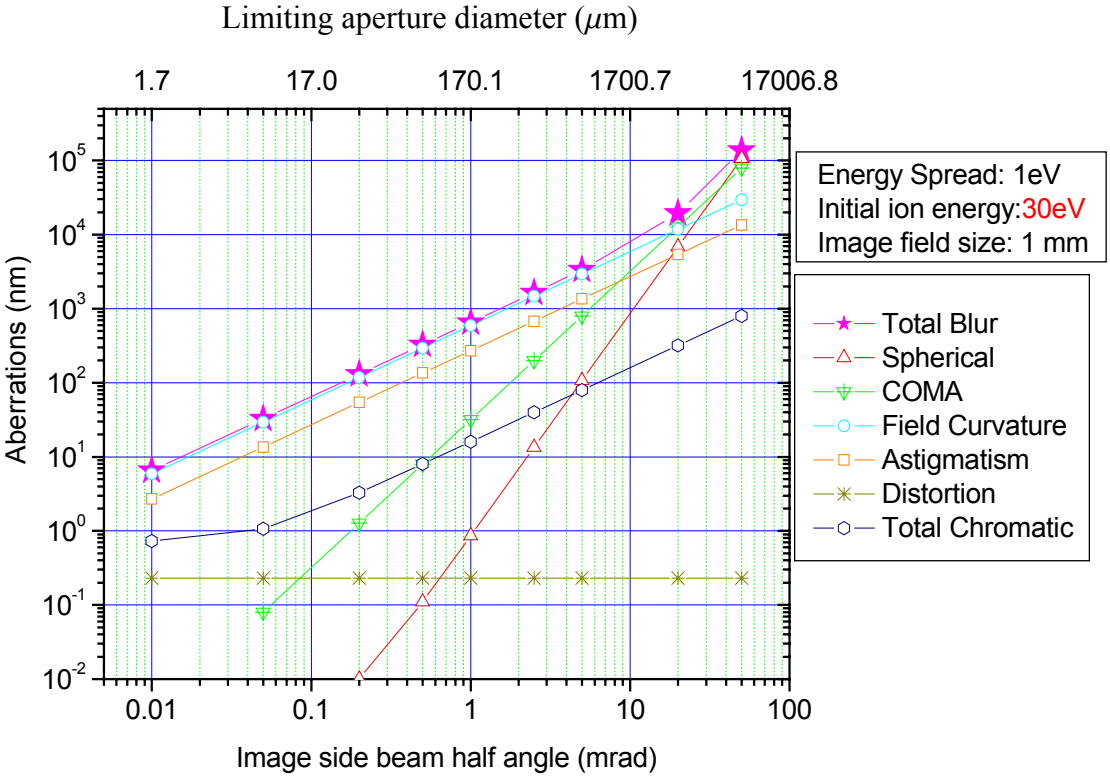

Figure 3.12 Aberrations v.s. image side beam half angle at telecentric optics condition.

3.2.4 Actual MMRL optics performance at different field size and beam angle

Based on the discussions above, the discrepancy between Vinh V. Ngo's simulation results and the experimental results can be explained with the low initial ion energy and the large beam half angle in the actual MMRL system. Total beam blurs at

different field sizes and different beam half angles have been calculated in fig. 3-13, when the initial ion energy was set to be 2 eV.

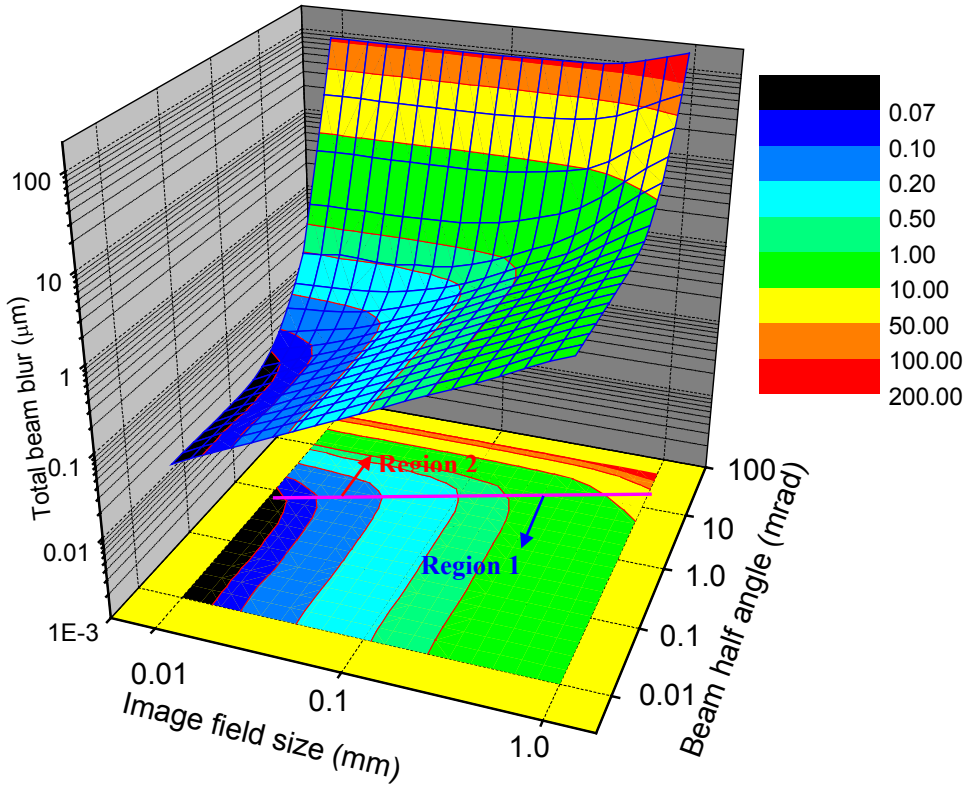

Figure 3.13 Total beam blur versus image field size and beam half angle when the initial ion energy is set to be 2 eV. All the axises are plotted in log scale.

The 3-D color profile has been projected onto the bottom surface in fig. 3.13. The projected color contour plot can be separated into two regions by a purple straight line. Beam blur in region 1 is mainly limited by field size. And the one in region 2 is determined by beam half angles. Region 1 is much larger than region 2. It means that the

total beam blur is mostly determined by shaped-beam aberrations. Among them, the off-axis chromatic aberration is important at small beam half angles and large beam sizes. Astigmatism and field curvature are the dominating source of blur at medium beam half angle and large field sizes. Due to the large off-axis chromatic aberration, image field size has to be smaller than 0.02 mm to obtain resolution of 70 nm (black region). But the beam half angle can be as large as 1.0 mrad for this resolution.

If the MMRL optical column is redesigned for the actual initial ion energy to work in telecentric condition, distortion and shaped beam chromatic aberration can be cancelled. Initial ion energy doesn't change other aberrations too much (fig. 3.7). So the beam blur for telecentric imaging condition can be approximated with the quadrature sum of spherical aberration, coma, field curvature, astigmatism and axial chromatic aberration. The simulated total beam blur at telecentric condition is shown in fig. 3.14. The projected contour plot is till separated into two regions, which have the same definitions as fig. 3.13. Region 2 is much larger than region 1. It means that the beam blur is mostly limited by beam half angles. The dark blue and the black areas are the regions for sub-50 nm resolution. The resolution capability can be greatly improved at telecentric optics condition. Within a 250 μm image field size, resolution better than 50 nm can be obtain at a beam half angle of 1.0 mrad. Selection of the beam half angle and the image field size directly affects the resolution and the throughput for MMRL. Choosing the operation parameters along the purple line in fig. 3.14 will give both a maximum field size and a maximum beam angle for certain resolution.

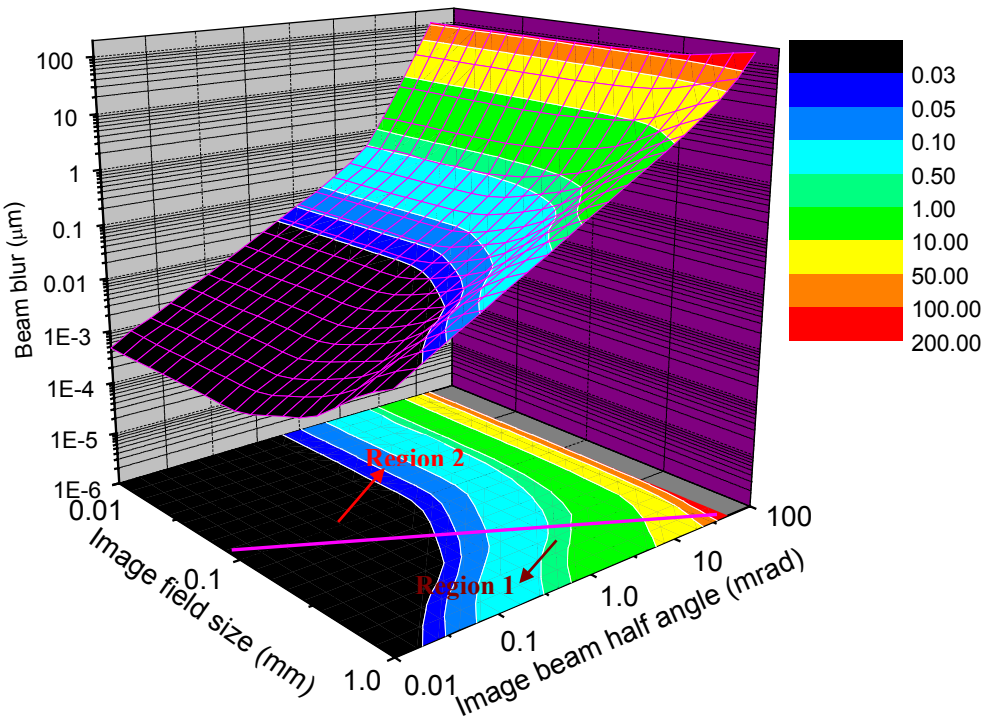

Figure 3.14 Total beam blur versus the image field size and the beam half angle in telecentric optics condition.

3.3 Resolution improvement by employing a limiting aperture to the MMRL ion optics column

It is difficult to obtain a small beam half angle in the original MMRL optics column, which is the major reason for the large beam blur observed in Vinh V. Ngo's experimental result. In order to reduce the beam half angle, a limiting aperture has been installed at the beam cross-over position.[9] For ordinary projection optics, ions injecting from a mask or a pattern generator with the same radial and circumferential slopes will be focused onto a same point in a plane perpendicular to the column axis. This plane is called the cross-over plane. The spatial coordinate on the cross-over plane corresponds to the angular coordinate on the object plane. If a limiting aperture is installed on the cross-over plane, it will only transmit ion beams with angles in a certain range on the object plane. The range of the angle is determined by the diameter of the limiting aperture. The center point of the angular distribution corresponds to the off-axis coordinates of the limiting aperture. Ions on the object plane may have a Gaussian angular distribution, which has the maximum amplitude at zero-angle. Consequently, the on-axis point on the cross-over plane has the highest current density. The current density will decrease very rapidly with increasing off-axis distance. Thus, it is very important to align the limiting aperture to the point with the highest current density.

3.3.1 Limiting aperture design

The original MMRL optics column is shown in fig. 3-15. The new optics column with a limiting aperture is plotted in fig. 3-16. There are two thick electrodes on the both

sides of the limiting aperture, which can help to reduce the electric field around the limiting aperture. The aberration integration simulation was performed on the new column. The result is about the same as fig. 3.13 because the addition of the limiting aperture does not change the ray trajectory too much. The corresponding limiting aperture diameter for certain beam half angle can be found in fig. 3-10 and fig. 3-12. It can also be calculated with the following equation:

$$D_{ap} = \alpha / 0.00588 \tag{3-11}$$

Here, D_{ap} is the limiting aperture diameter in μm and α is the image-side beam half angle in mrad. In order to obtain a beam half angle of 1.0 mrad, the diameter of the limiting aperture should be 170 μm. In the ideal case, beam blur will be less than 70 nm within a field of 20 μm on the image plane if the beam half angle is 1.0 mrad.

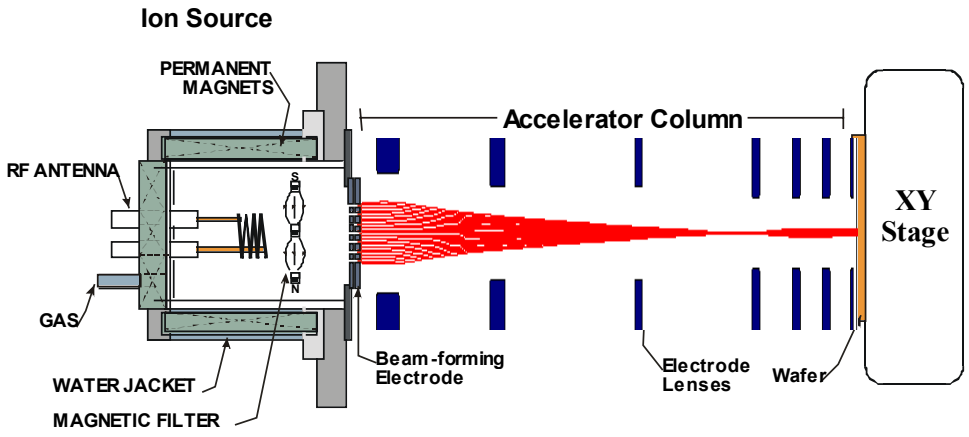

Figure 3.15. Schematic of the original MMRL ion optics.

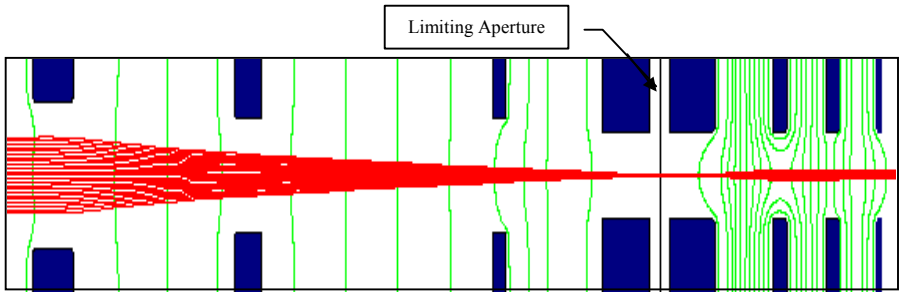

Figure 3.16 New MMRL optics column with a limiting aperture placed at the cross-over plane.

3.3.2 Resist exposure experiment with a limiting aperture

Ion beam exposure experiment has been performed with a limiting aperture of 100 μm in diameter. The comparison of the exposure results with and without a limiting aperture has been shown in fig. 3.17. The same 1 μm hole-array mask has been used in both experiments. The image obtained on the original MMRL optics column is very rough because of large blur. After a limiting aperture was installed, helium ion beam exposures on PMMA C4 resist give much better resolution than before. Round contact holes with diameter of 200 nm show fairly smooth and sharp edges (fig. 3.17 (b)). In addition, features as small as 120 nm can be observed in some areas even though the edge isn't very smooth. The experimental results confirmed the resolution improvement after a limiting aperture was installed. But 200-nm features are still larger than the simulation prediction. There might be some other factors that haven't been taken into consideration, such as the aberrations induced by the limiting aperture.

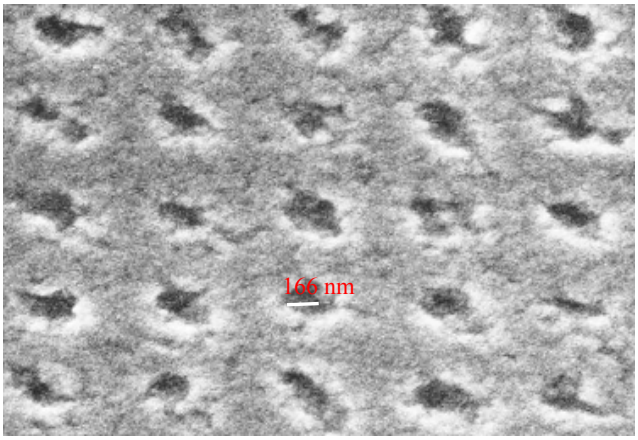

a)

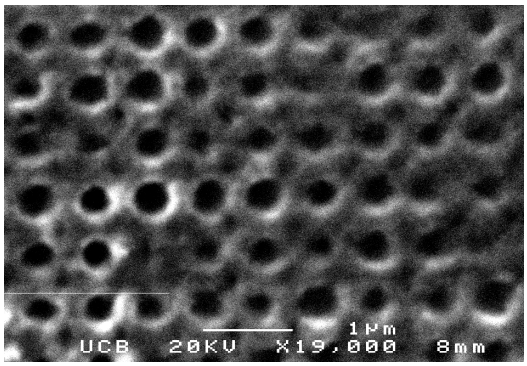

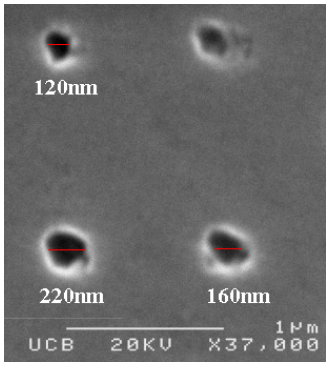

b) c)

Figure 3.17 a) Ion beam exposure result on the original MMRL system; b) Helium ion exposure on PMMA C4 with 100 μm limiting aperture installed; c) Features as small as 120 nm can be resolved in some area.

3.3.3 Field-free limiting aperture design

Even though the electric field around the limiting aperture has been reduced by the two thick electrodes placed on the both sides, as shown in fig. 3.16 and the top left graph of fig. 3.19, some residual electric field can still penetrate into the aperture. The axial potential distribution for the prototype limiting aperture design has been calculated in fig. 3.18. Even though the first order derivative to the potential (e.g. the electric field) is small around the limiting aperture plane. The second order derivative of the potential

shows a very high spike at the limiting aperture plane. This is caused by the abrupt change of the electric field on both sides of the limiting aperture. It will act as an additional electrostatic lens with extremely small diameter (shown in the top middle graph of fig. 3.19) and generate additional aberrations. Because of the small thickness, aberration integration simulation may not be able to reflect the aberrations generated by the limiting aperture. However, accurate ray tracing should be able to take those aberrations into account as long as the finite-element mesh around the limiting aperture is set to be dense enough.

During the ray tracing simulation, three bunches of rays with angle up to 0.45^{o} are emitted from three points on the object plane. The spacing between the three points is 10 μm. With a reduction ratio of 10, the spacing will be focused to 1.0 μm on the image plane. The ray tracing results around the image plane are shown in the right side graphs of fig. 3.19. The size of the ray bunch corresponds to the beam blur of the optics column. With the prototype limiting aperture design (fig. 3.16), the ray-tracing simulation gives a beam blur much higher than 100 nm.

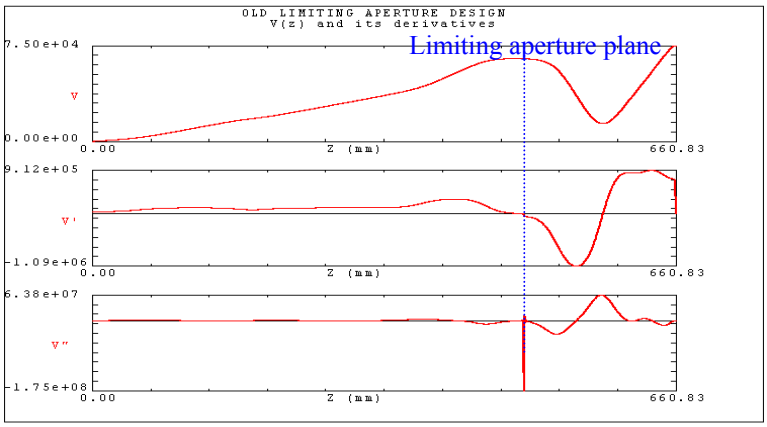

Figure 3.18 The axial potential distribution and its first, second order derivatives along the column if a limiting aperture--with the design shown in fig. 3.16.-- is installed

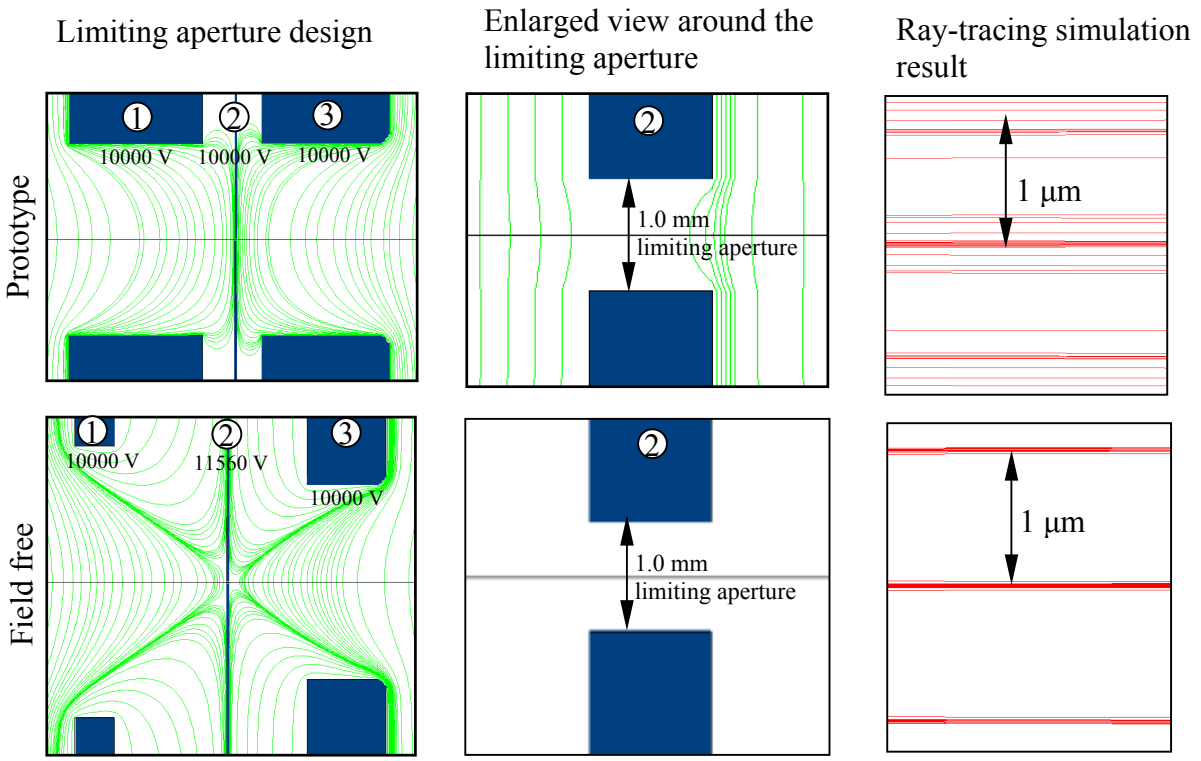

Figure 3.19 Two different limiting aperture designs and the corresponding ray-tracing results. The top one is the prototype limiting aperture design. The bottom one is the new field-free limiting aperture design.

A possible solution to eliminate aperture-induced aberrations is to create a field-free region on both sides of the limiting aperture. This kind of limiting aperture design has been successfully obtained as shown in the bottom left graph of fig. 3.19. The position and the shape of the two adjacent electrodes (1 and 2) have been adjusted to balance the electric field on both sides of the limiting aperture, and then the voltage on the limiting aperture was increased to 11,560 volt, which resulted in an almost "field-free" region around the limiting aperture (bottom middle graph in fig. 3.19). Ray tracing simulation (two right-side graphs of fig. 3.19) shows that the field-free limiting aperture can greatly minimize the aperture induced aberrations. Axial potential distribution and its

first-order/second-order derivatives have been calculated for the column with the field-free limiting aperture (fig. 3.20). The electric field and its derivative are both zero at the limiting aperture plane, which confirmed the field-free limiting aperture design.

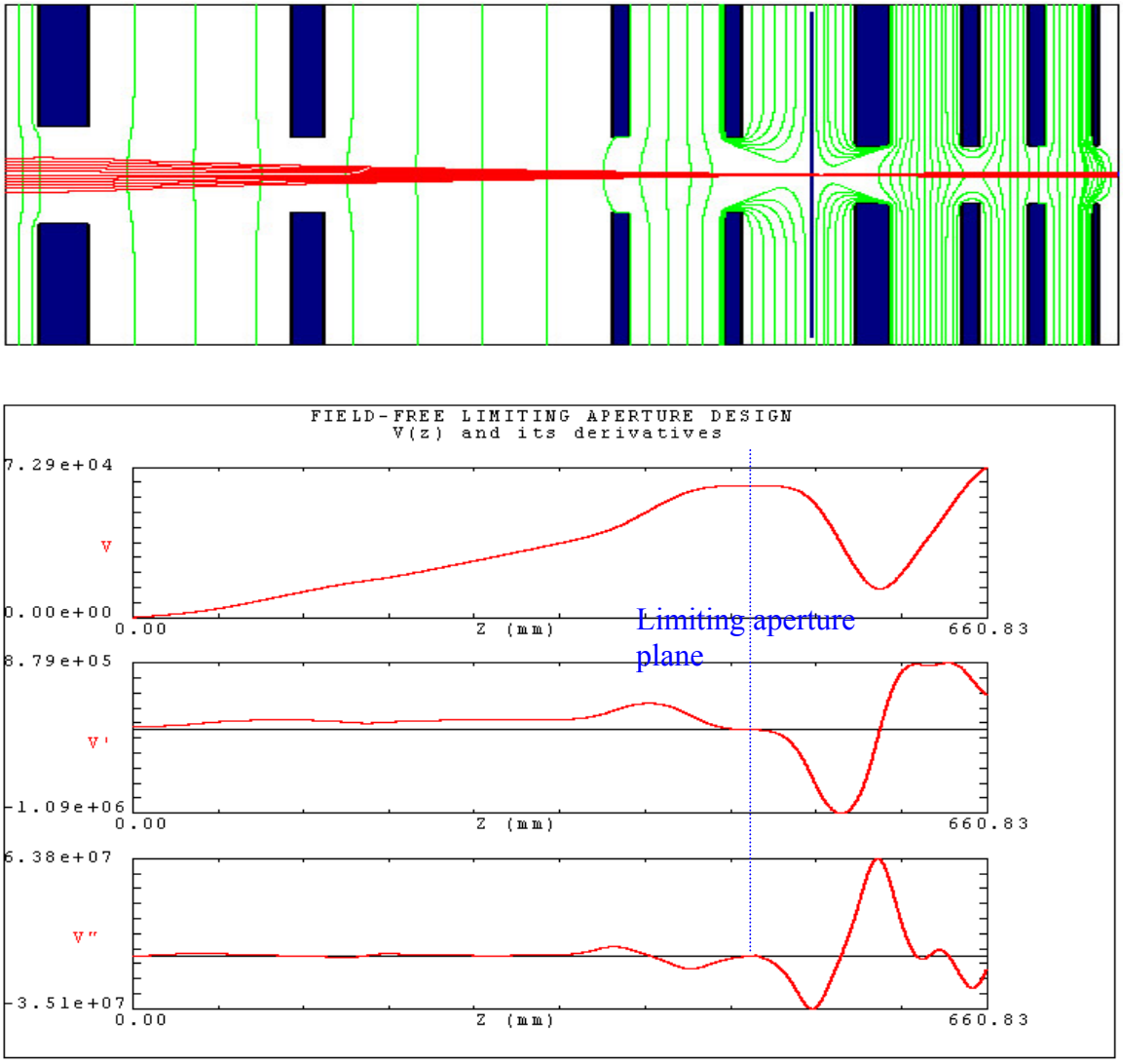

Figure 3.20. New ion optics column with a field-free limiting aperture design (top) and the axial potential distribution with its first/second order derivatives along the column axis.

3.3.4 Resist exposure experiment with the field-free limiting aperture

Resist exposure experiment had been carried out to test the performance of the field-free limiting aperture. Fig. 3.21 is the developed 950K A4.5 PMMA resist after exposed by the 75 keV helium ion beam to a dose level of 20 μC/cm^2. Contact holes with diameter of 100 nm have been printed on the resist. The edge is very smooth and sharp. The resolution has clearly been improved after a field-free limiting aperture with a diameter of 100 μm was incorporated into the MMRL optics column.

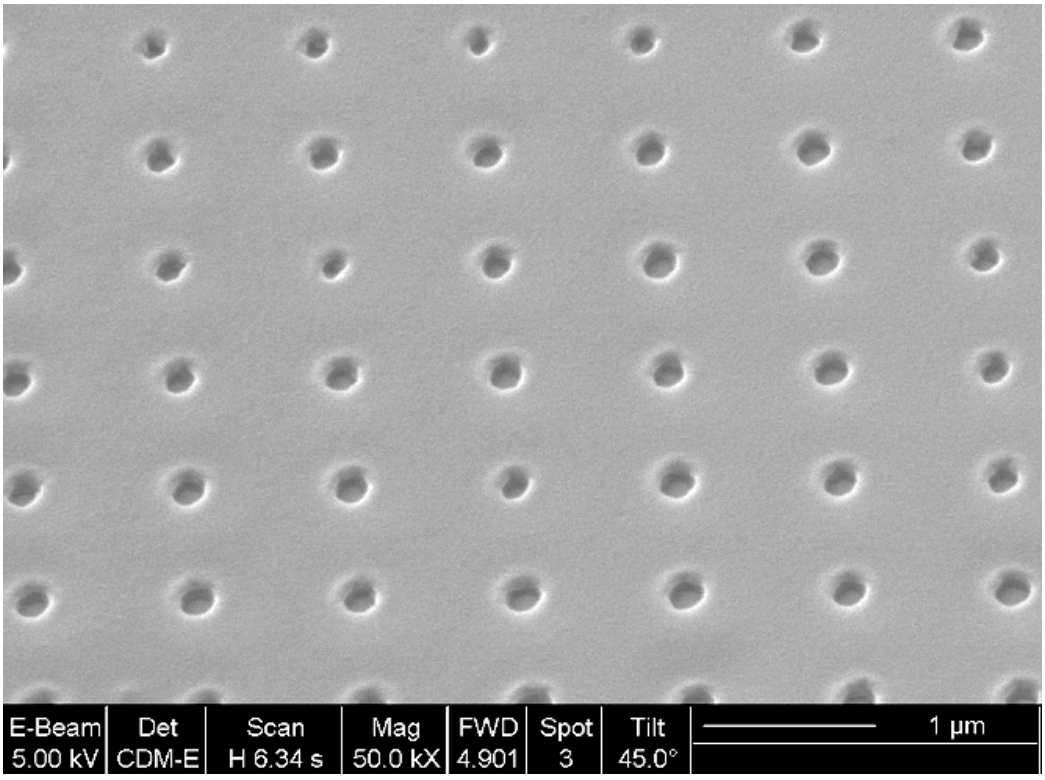

Figure 3.21. Contact holes printed on 950K A4.5 PMMA resist after the field-free limiting aperture was installed. Exposure dose is 20 μC/cm.

In a low dose condition, features as small as 50 nm can be observed in the result shown in fig. 3.22. Compared with the result obtained by V. V. Ngo, resolution has been improved by more than one order of magnitude. If the features on the mask have different aspect ratios, patterned ion beams will have different beam half angle in the original MMRL optical column. So the resolution will change with different features. But the beam half angle in the new MMRL optical column is only determined by the diameter of the limiting aperture. Features with different aspect ratios can be printed with about the same resolution. This is very important for process control.

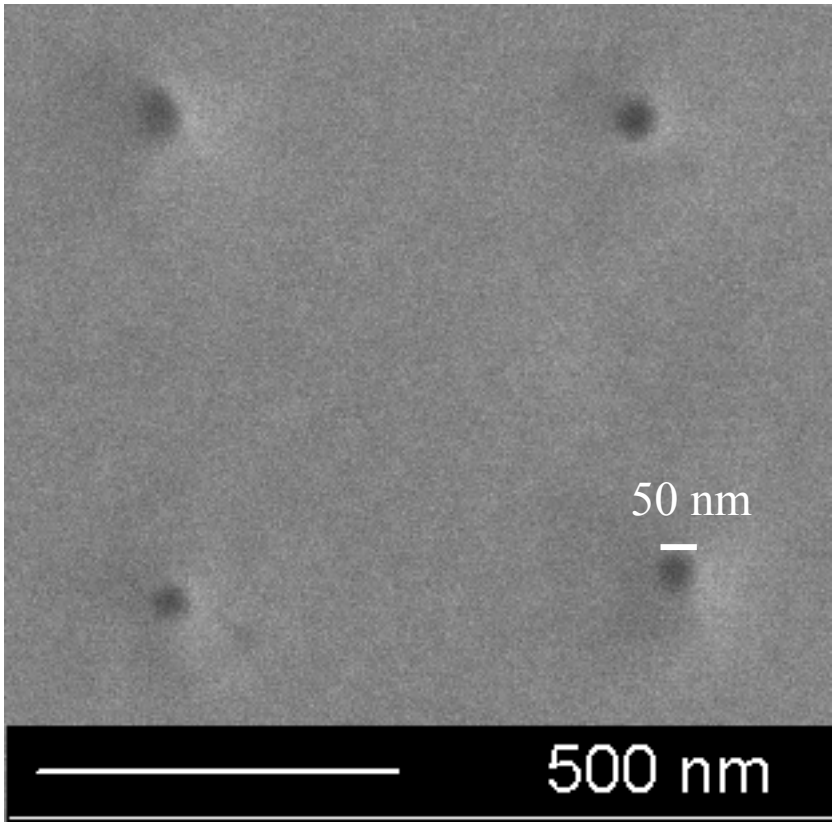

Figure 3.22 Contact holes printed on 950K A4.5 PMMA resist with dose of 5 μC/cm.

3.4 Electro-magnetic interference

The early ion beam exposure experiments on the MMRL system revealed a double-pattern image problem. This is caused by the earth magnetic field as pointed out be Vinh V. Ngo in his Ph.D. thesis.[1] If the ion source is operated at a low power and high-pressure condition, H^+, H_2^+ and H_3^+ ions will be produced in the discharge plasma. Due to the different charge-to-mass ratio, they will be deflected to different positions on the wafer plane by the earth magnetic field. When the original MMRL system was designed, there is no magnetic shielding at all. Even though the Lamour radius of ions is much larger than that of electrons, they can still be deflected by tens of microns in the 0.5 gauss earth magnetic field because of the long column length and the low ion energy in some sections of the ion optical column.

Besides the static magnetic field, there exist two other electro-magnetic interferences (EMI) in the MMRL lab space---high frequency rf radiation and low frequency stray magnetic field. High frequency rf comes from the rf power supply. Stray ac magnetic field can be generated by many lab equipments. RF power can be coupled to the high voltage power supplies and create rf ripple, which will increase the chromatic aberration. Fortunately, rf EMI can be shielded with high conductance metal sheets. So the matching box and the antenna leads must be totally enclosed. The matching box must also be connected with the rf power supply through high conductance metal sheets with sufficient surface area because of the skin effect for rf current.

Low frequency ac magnetic field can deflect the ion beams like the earth magnetic field does. But the deflection direction changes with time, so it will directly blur

the printed images. Stray ac magnetic field must be shielded with high permeability materials. The shielding to the ac magnetic field will be discussed in section 3.4.3.

3.4.1 Deflection due to the earth magnetic field

The magnitude of the earth magnetic field is about 0.5 gauss. The deflection caused by the earth magnetic field can be precisely calculated after the axial electrostatic potential distribution is simulated by SOELENS, which is a second-order finite element code for calculating the electrostatic potential distribution in any rotationally symmetric electrostatic lens. The earth magnetic field can be approximated with the deflection field generated by a very large magnetic deflector. A simple saddle yoke type deflector has been used to generate a 0.5-gauss magnetic field perpendicular to the column axis. The deflector is 1300 mm long with the inner and outer diameter of both 25 mm across a span of 90^{o}. Then a direct ray-tracing program based on Runge-Kutta method, called SORAY, was been used to precisely calculate the beam deflection in the compound field generated the magnetic deflector and the electrostatic lenses. The simulation result has been listed in table 3-1.

Table 3-1 Beam deflection due to the 0.5 gauss earth magnetic field for different ions.

Ion species	H^+	H_2^+	H_3^+	He^+	C^+	N^+	N_2^+	O^+	O_2^+	H_2O^+	OH^+
Deflection (μm)	57	40	33	28.5	16.5	15	10.8	14.3	10	13.47	13.86

Fig. 3.23 is the PMMA resist exposure result obtained by Vinh V. Ngo when hydrogen was used to form the plasma. There are two images separated by 13 μm in the experimental result. If the two images are generated by H^+ and H_2^+ separately, the

spacing will be 17 μm from the data in table 3-1. It is very close to the experimental observation---13 μm---considering that the 0.5 gauss earth magnetic field is not exactly perpendicular to the column axis.

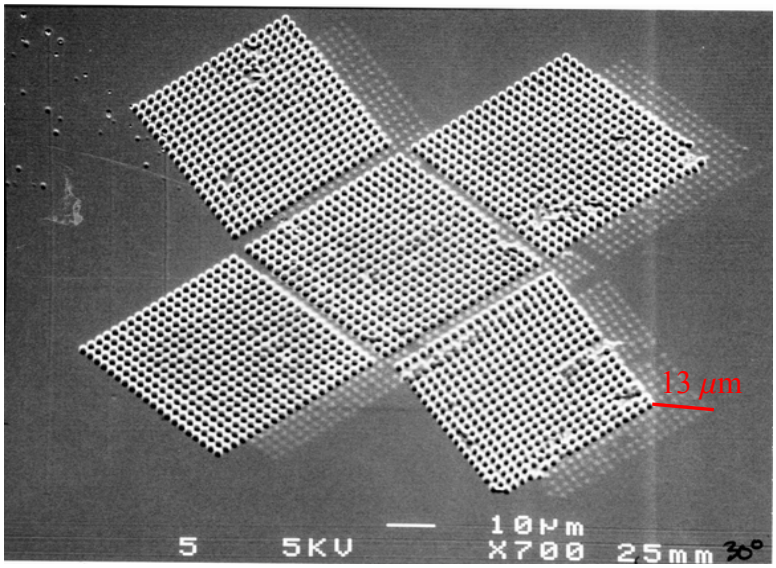

Figure 3.23 Hydrogen ion beam exposure on PMMA resist. Double image pattern with spacing of 13 μm has been observed.[5]

It has been experimentally demonstrated that H^+ ion species ratio can be as high as 98.5% with input rf power of 2,500 watt and operation pressure of 5 mTorr in the MMRL ion source[1]. But the effect of H_2^+ can not be ignored in low power and high pressure operating condition. The ambient magnetic field on the column axis should be decreased by 867 times to obtain an image distance of 15 nm for H^+ and H_2^+ ions. This shielding ratio is extremely difficult to obtain considering the large diameter of the electrodes in MMRL. Helmholtz coil can be used to actively cancel part of the ambient

magnetic field. But the ion optics column in MMRL is longer than 60 cm. It is difficult to totally cancel the magnetic field along such a long space using Helmholtz coil. Active cancellation using Helmholtz coil and passive magnetic field shielding should be combined to reduce the beam deflection to an acceptable range.

Another solution to eliminate the double-image problem is to use helium to generate the plasma. Ideally, helium gas will only produce He^+ ion. But helium is extremely difficult to be ionized. If trace amount of impurities exist in the ion source, they will be ionized with a higher portion and generate multiple images. An ion source cleaning process has been developed to eliminate the impurities. First, the ion source wall is baked with a heat tape for over four days right after the initial pump down. Then a helium discharge cleaning process with rf power of 100~200 watt is applied for 8 hours. The helium ion beam exposure result in fig. 3.21 confirmed that most of the impurities could be decreased to a negligible low level with the cleaning process above.

3.4.2 Interference from the ac magnetic field

After the resolution on MMRL has been improved by employing a limiting aperture on the cross-over plane, much smaller features can now be resolved. In some experiments, a strange exposure pattern can be observed frequently, as shown in fig. 3.24 (a~c). At a relatively high dose, the contact-hole patterns sometimes show elliptical shape with a long-axis distance of about 300 nm (fig. 3.24 (a)). When the dose is decreased, two small holes can be observed at the bottom of some large holes (fig. 3.24

(b)). At an even lower dose level, pairs of adjacent holes with diameter less than 60 nm can be observed. This strange result can be explained with the interference from the stray ac magnetic field.

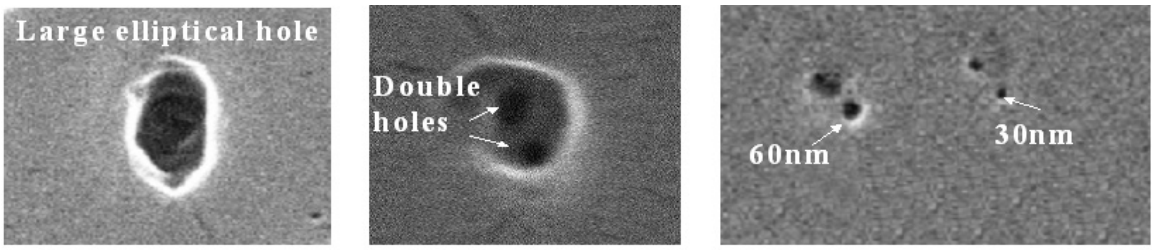

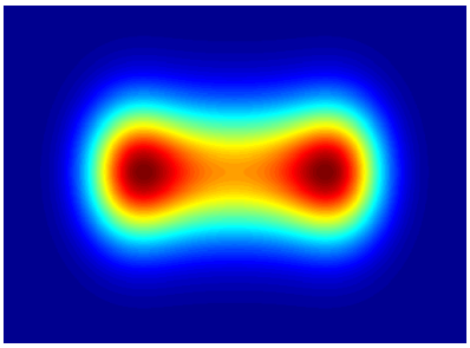

(d) Simulated dose profile in ac magnetic field

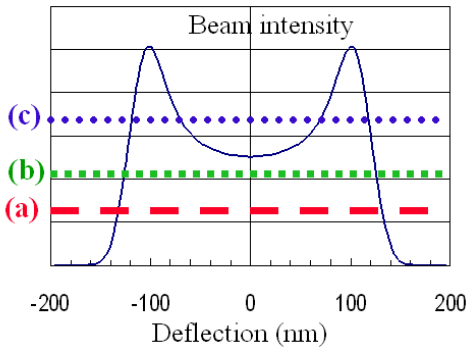

(e) Cross-sectional view of the dose profile

Figure 3.24 AC magnetic field interference can create elliptical hole (a) or pairs of small holes (b,c) depending on the exposure dose. This can be explained with the simulated dose profile (d) when 3.5 mGauss ac magnetic field exists. The three dashed lines in the cross-sectional view of the dose profile (e) corresponding to the three scenarios shown in figure a-c.

A simulation program has been developed with Matlab to calculate the ion beam exposure dose profile in a 60 Hz sinusoidal ac magnetic field. The magnitude of the ac magnetic field was set to be 3.5 mGauss in one direction. The simulated dose map is shown in fig. 3.24 (d). It shows two humps along the beam deflection direction. The cross-sectional view of the dose map along the peak of the two humps is shown in fig.

3.24 (e). The dashed lines with different colors represent three different doses that generate the resist profile in fig. 3.24 (a~c).

High frequency electromagnetic interference (EMI) can be easily shielded with high conductivity metals. But low frequency EMI (stray ac magnetic field) can only be shielded by high permeability metals. Stray ac magnetic field has the highest magnitude within the frequency range of 60~300 Hz. Many lab equipments can generate ac magnetic field, especially from the transformer. There are two high-voltage isolation transformers used for the MMRL system. Even though they are 2 meters away from the column, the stray ac magnetic field generated by the transformers can still be detected by an ac gauss meter around the column. Turbo pump controllers and power supplies are also sources of ac magnetic field, especially the turbo controller. They should be placed far away from the column.

Improper grounding to lab equipments can also generate ac magnetic field. In order to reduce the risk of electric shock, all the lab equipments have been grounded through a separate grounding path, as illustrated in fig. 3.25. The other end of the grounding path is connected to the grounding wires of the building infrastructure. Part of the current from the hot wire will be coupled into this separate grounding path. Then the return current on the neutral wire will be less than the current on the hot wire. There will exist a net current on path 1, which will generate ac magnetic field in lab space and affect the imaging quality. In a proper grounding design, all the current returns along the same path as the power cables. So the grounding path lying on the floor of the MMRL lab space has been disconnected. And all the equipments have been grounded through a grounding wire returning with the power cables.

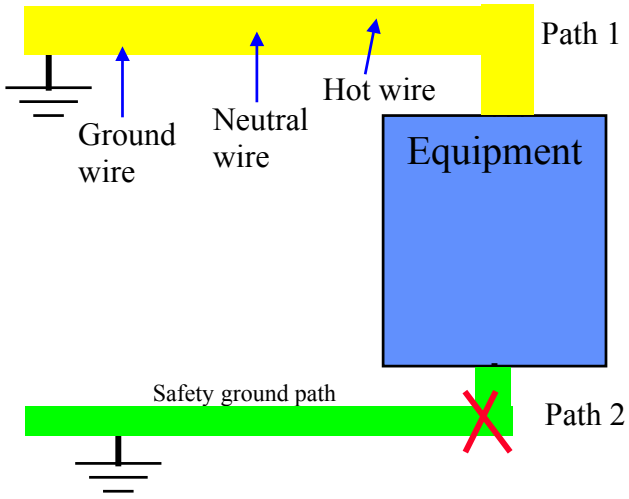

Figure 3.25. Separate grounding path can cause unbalanced current in path 1 and 2, which will generate stray ac magnetic field in lab space. In order to reduce this effect, the grounding path must be placed together with the hot and neutral wires.

3.4.3 Magnetic field shielding for MMRL

In order to further reduce the interference from the ambient magnetic field, the magnetic field has to be shielded. The principle of the magnetic field shielding is to provide a high conductance path for the ambient magnetic flux around the system. Magnetic shielding materials are chosen based on permeability and saturation. As permeabilities increase in magnetic shielding materials, their saturation levels decrease. Fortunately, the ambient magnetic flux density is usually about several gauss or even lower. Alloy with extremely high permeability, μ-metal (80% nickel-iron alloy), has been

used to design the magnetic shield for MMRL. The saturation level of the μ-metal is about 8000 gauss, which is much higher than the ambient magnetic flux density in the MMRL lab. The magnetic shield for the MMRL system is free from the saturation effect.

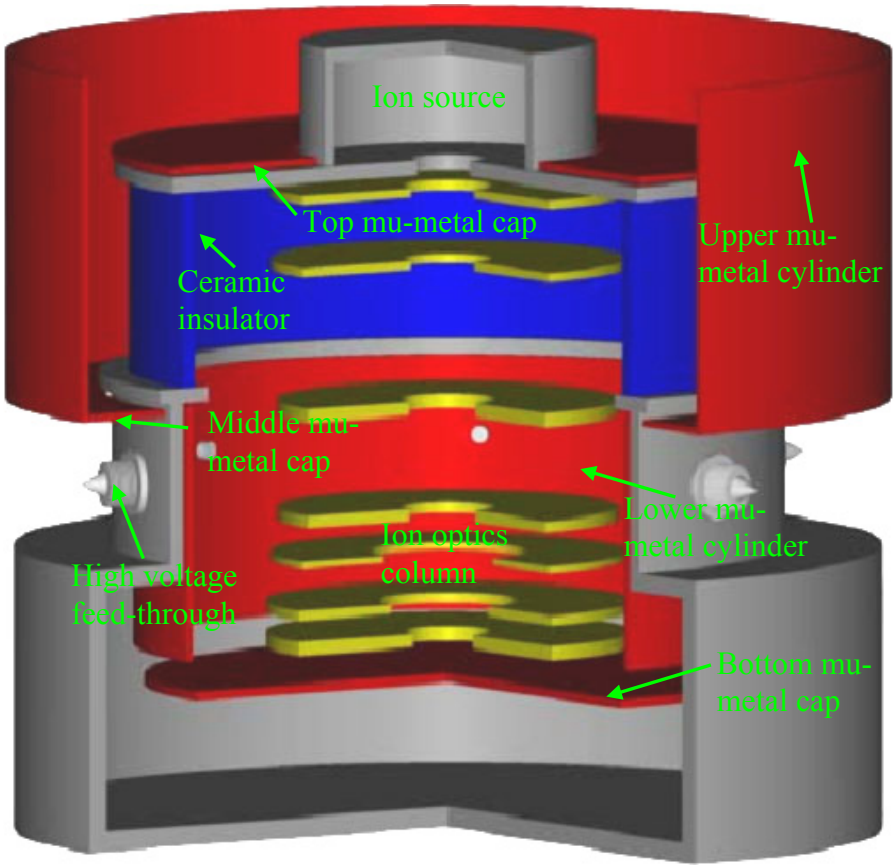

Fig. 3.26 Schematic drawing of a proposed magnetic shield design for MMRL.

The attenuation factor of an infinitely long cylindrical magnetic shield can be calculated from the following equation:

$$A = (\mu/4)\left[1-\left(\frac{R_0 - T}{R_0}\right)^2\right]+1 \qquad (3\text{-}12)$$

Where A is the dc magnetic field attenuation factor, μ is the relative permeability, R_o is the outer diameter of the cylinder, T is the thickness of the shielding material. Based on this equation, in order to obtain an attenuation factor of 40 in a long cylinder with a diameter of 15 inch and a permeability of 10,000, the thickness should be above 0.117 inch.

A magnetic field shield for MMRL is shown in fig. 3.26. It consists of two cylinders with different diameters and a donut-shape plate in between. There are two extra caps placed on the both ends. Since the top ion source is charged to 75 kV in MMRL, certain spacing between the top cap and the upper cylinder is required. Multi-layer Teflon sheets will be inserted in the spacing to hold the voltage between 75 kV and ground. The top mu-metal cylinder has been extended by 12 inch higher than the mask plane to improve the shielding effect. The top and bottom caps are used to further reduce the magnetic field that may enter from the two open ends of the cylinders.

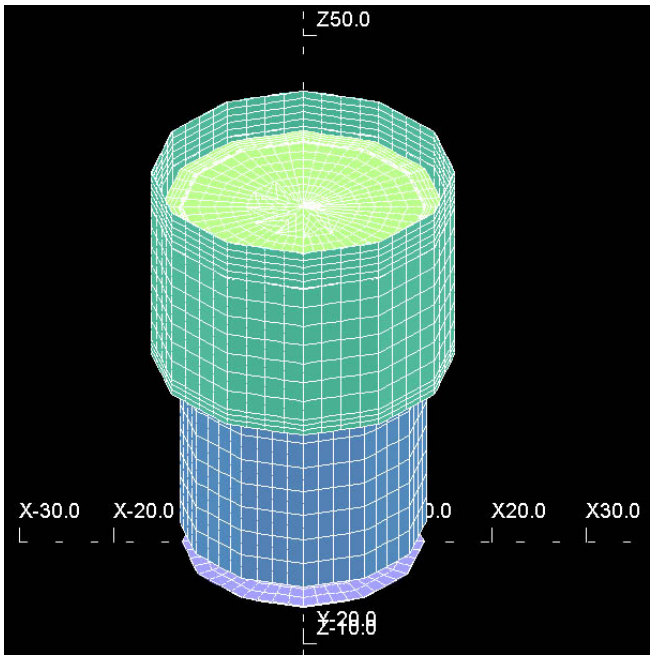

Fig. 3.27 Finite element model built in the OPERA-3D with surface mesh plotted. View angle has been tilted by 35^o out of the plane.

In order to evaluate the effectiveness of the above design, finite-element-mesh simulation has been carried out to determine the attenuation factor. The FEM simulation was performed on commercially available software called OPERA3D-TOSCA from Vector Fields Inc. The finite-element model for the magnetic shield built in OPERA3D has been plotted in fig. 3.27.

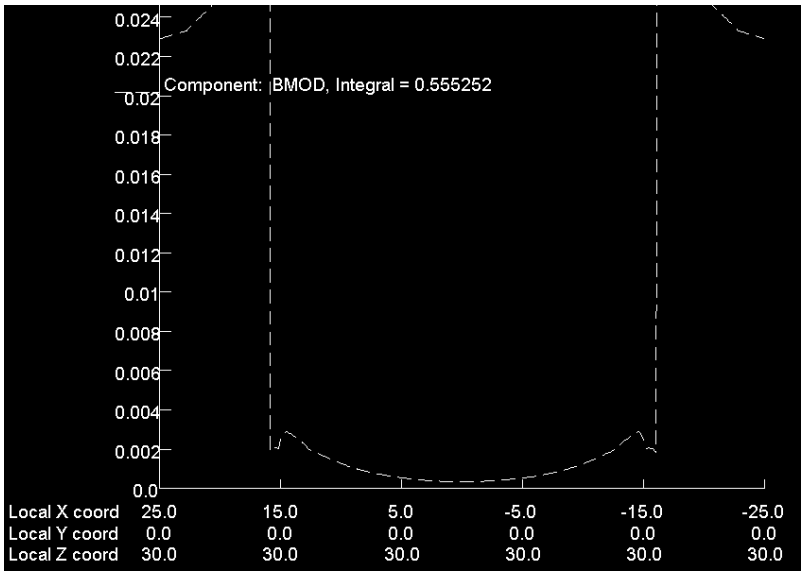

Fig. 3.28 Magnetic flux density along a straight line that crosses the column axis. The coordinates of the line were displayed at the bottom of the plot.

It's very difficult to generate first-order finite elements in very thin shielding materials with circular shape. As a result, duodecagons are used to approximate the μ-metal cylinders in the finite element models. Quadrilateral meshes, instead of triangular meshes, were adopted to increase the simulation speed. An ambient magnetic flux with density of 0.0225 gauss was created outside the shielded space. Shielding alloy with thickness of 0.125 inch and a permeability constant of 10,000 was used in the simulation.

The magnetic flux density along a straight line, parallel to the X-Y plane and crossing the axis at 30 inches above the bottom cap, is plotted in fig. 3.28. The magnetic flux density on the axis has been decreased to 0.00033 gauss, which corresponds to an attenuation factor of 68.

The magnetic flux density along the axis of the column has also been calculated (fig. 3.29). The magnetic flux density is lower than 0.00055 gauss all along the column axis, which means that an attenuation factor better than 40 has been obtained with the magnetic shield plotted in fig. 3.26.

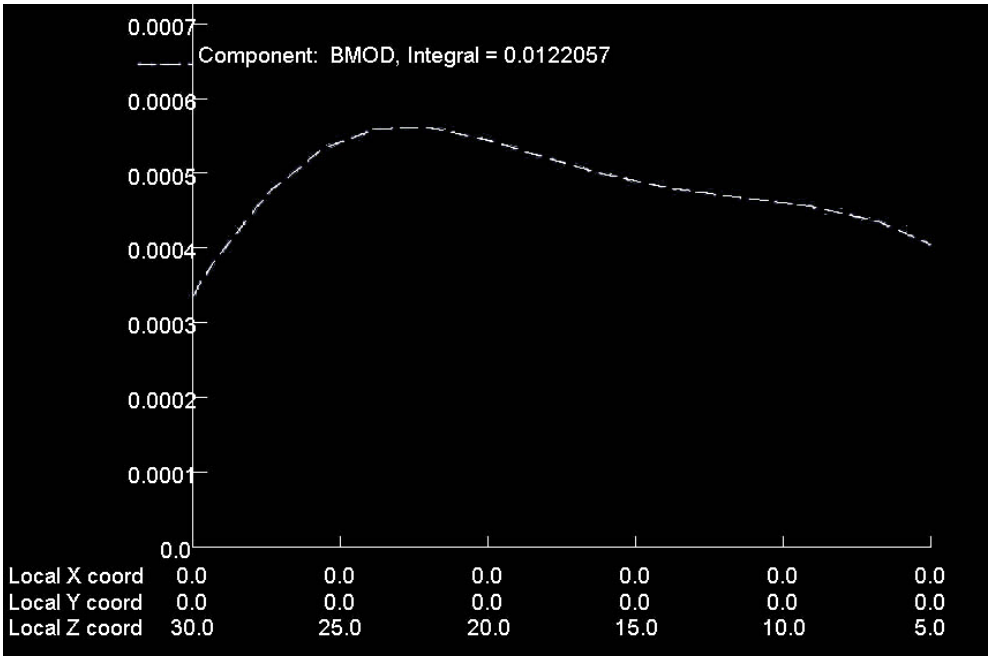

Fig. 3.29 Magnetic flux density along the column axis if the ambient magnetic flux density is 0.0225 gauss

3.5 Ion-ion interactions in MMRL ion optics

There are two major factors that directly limit the throughput of charged particle lithography systems. The first factor comes from the large lens aberration coefficients, which limit the attainable field size and the beam half angle. The second factor is caused by the interactions between charged particles, which limit the maximum allowable beam current that can be transmitted to the image plane without losing the spatial resolution of the patterned beams.

Charged particle interactions can be categorized into three kinds: global space charge effect, trajectory displacement effect, and Boersch effect[10]. Global space charge effect is caused by the average electric field generated by the charged particles. It acts as a negative lens resulting in a defocus effect to the ion or electron beams. The defocus effect can be compensated by adjusting the lens power or moving the image plane. But the non-uniform defocus due to the space charge can also generate extra lens aberrations.[11] Trajectory displacement effect, first investigated by Loeffler, is caused by the interactions between the charged particle and its neighbors encountered along the path. It causes lateral shift of the particle positions and changes the particles' velocity perpendicular to the column axis. The Boersch effect, first investigated by Boersch, is also known as energy broadening. It is generated because the individual interactions along the beam path can also change the axial velocity of the particles. It will increase the axial energy spread and create extra chromatic aberrations in focusing lenses and deflectors. The trajectory displacement effect and the Boerach effect are generated by statistical interactions. Consequently, they can't be cancelled and will directly deteriorate the system resolution.

3.5.1 Physics of charged particle interactions

Many characteristics of the trajectory displacement effect can be understood through a very simple physics model (fig. 3.30). If two identical particles with the same energy E and charge q move in parallel at distance D apart, they will be deflected to opposite directions by displacement d after traveling for a distance L. If $d << D$, we can assume the repulsive force between the two particles is the same all long the path. Then the displacement d can be calculated with the following simple equation:

$$d = \frac{L^2 \cdot q^2}{16\pi\varepsilon_0 D^2 E} \tag{3-13}$$

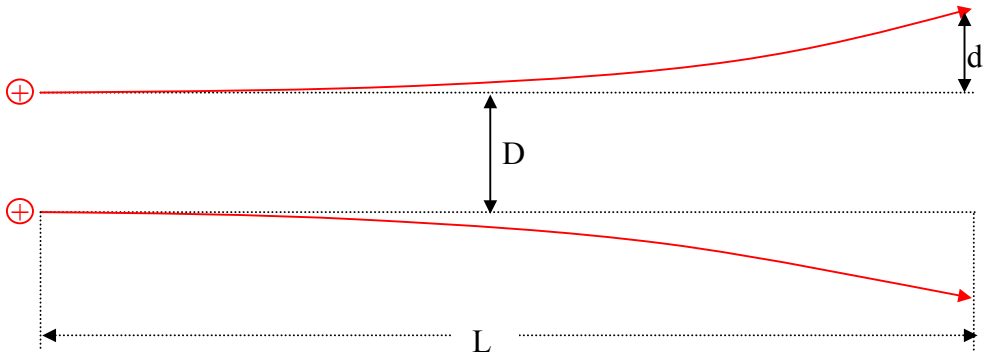

Figure 3.30 Repulsive force between two ions will deflect them in opposite directions by a displacement of d. The distance of the two particles is D and the length of the path is L.

The spacing D is inversely proportional to the cube root of the particle density (n), e.g. $D \propto \frac{1}{n^{\frac{1}{3}}}$. The current density of the charged particle beam can be expressed with equation (3-14):

$$J = n \cdot q \cdot v = n \cdot q \cdot \sqrt{\frac{2E}{m}} \tag{3-14}$$

$$\therefore \qquad n = \frac{J\sqrt{m}}{q\sqrt{2E}} \tag{3-15}$$

$$\therefore \qquad D \propto \frac{q^{\frac{1}{3}}(2E)^{\frac{1}{6}}}{J^{\frac{1}{3}}m^{\frac{1}{6}}} \tag{3-16}$$

Substitute equation (3-16) into equation (3-13), the following equation can be obtained:

$$d \propto \frac{L^2 q^{\frac{4}{3}} J^{\frac{2}{3}} m^{\frac{1}{3}}}{16 \cdot 2^{\frac{1}{3}} \pi\varepsilon_0 E^{\frac{4}{3}}} \tag{3-17}$$

Even though the above model is not sufficient to quantitatively calculate the trajectory displacement effect in an actual ion or electron optical system, equation 3-17 can still provide some qualitative information about the dependence of the charged particle interactions with beam energy, current, particle mass and column length. In general, the lateral trajectory displacement increases very fast with the column length L. Decreasing the column length can be very efficient to reduce the charged particle interactions. High current density will increase the mutual interactions because of the small spacing between the particles. For highly collimated ion or electron beams, the incoming particles will be focused onto a tiny cross-over point along the column axis. The smaller the cross-over diameter is, the higher the current density will be. Since the diameter of the cross-over is proportional to the beam half angle, larger beam half angle and lower total current on the object plane can reduce the current density on the cross-over position and minimize the charged particle interactions. But throughput will suffer at low beam current. Also, large beam half angle will increase beam blur generated by the lens aberrations. This is one of the most important trade-offs between the resolution and the throughput that may limit the scalability of the charged particle lithography or inspection systems for future design rules.

Another way to counteract the charged particle interactions is to increase the beam energy along the beam path. High energy will decrease the particle density for the same total current. It can also reduce the particle transit time along the column to minimize the transverse displacement from the mutual repulsive force. High mass ions will increase the trajectory displacement effect because they move slower and have a higher particle density for the same total current. MMRL is an ion beam projection system. If helium ions are used to expose resist, charged particle interaction effects can be 19 times higher than electron beam lithography at the same current. Fortunately, ion beam lithography requires lower dose to expose resist than the electron beam counterpart. But low dose may generate shot-noise problem for features below 30 nm or smaller.

Since Boersch effect also originates from the statistical particle interactions, the above analysis to the trajectory displacement effect is also valid for Boersch effect. These two stochastic interactions become dominant in narrow beams with current about tens of microamps. The space charge effect increases linearly with the beam current. It is the dominant charged particle interactions in high current wide beams coming out from low brightness sources.

3.5.2 Charged particle interactions in electron and ion projection lithography systems

The coulomb interactions in probe forming systems are expected to be very high because of the high current density at the emission or focused spot. Projection systems

can tolerate higher total current by spreading the current over a large exposure area, except that there may exist small cross-overs along the axis of the beam path, where the current density is high. The charged particle interactions for electron and ion projection systems have been studied by several groups based on different optics models, which will be discussed in the following several paragraphs. Several empirical or analytical equations for the trajectory displacement effect have been obtained based on these models. Even though these equations are not exactly the same with each other, they share many common characteristics.

G. H. Jansen has studied the trajectory displacement effect for a one-lens projection system through extended two-particle theory and Monte Carlo simulation.[12] An analytical equation has been obtained by fitting the simulation results:

$$FW_r = C_1 \frac{I^{2/3} L_s^2}{V^{4/3} F^{4/3}} \left(\frac{M}{1+M} \right)^{7/3} = C_2 \frac{I^{2/3} f_2^{5/3}}{V^{4/3} F \cdot NA^{1/3}} \tag{3-18}$$

Here FW_r is the trajectory displacement, C_1 and C_2 are constants, I is the total current, L_s is the column length, M is the magnification, V is the beam accelerating voltage, F is the field size, f_2 is the focal length of the lens and NA is the system numerical aperture (e.g. beam half angle). Actually, equation 3-18 is very similar with equation 3-17, even though equation 3-17 is based on an extremely simple physics model without any focusing optics. Equation 3-18 has some extra terms such as M, F, f_2 and NA because it has considered the focusing lens in projection system. Jansen also predicted that the maximum attainable current on IMS ALG-1000 (He^+) ion projection lithography system is about 0.2~0.3 μA for 0.18 μm nodes, while that for SCAPEL electron projection lithography system is about 25 μA. The difference of the attainable current

between IPL and EPL is close to 100, which is 5 times higher than the prediction based on equation (3-17).

S.D. Berger and coworkers have studied the particle-particle interactions for a two-lens doublet projection system.[13] Their Monte-Carlo simulation was performed with a commercially available software (Discrete Coulomb Interactions Simulation Software from Munro's Electron Beam Software Ltd.). They also gave an empirical equation for the trajectory displacement effect of an ion beam projection system:

$$b_{ion} = k_{ion}\left(\frac{(L+L_0)I^{\frac{1}{3}}(M+M_0)}{V\cdot\alpha}\right) \tag{3-19}$$

Here K_{ion}, L_0, and M_0 are constants, L is column length in mm, I is the beam current in μA, M is the image magnification, V is the beam accelerating voltage and α is beam half angle. The exponents on L, V and I in equation 3-19 are quite different from equation 3-17 and 3-18. But S.D. Berger and his coworkers pointed out that the simulation time for ion projection lithography is much longer than that of electron beam lithography, so the data set used to fit equation (3-19) may not be enough to give accurate parameters for voltage and current.

The stochastic coulomb interactions on ion projection lithography systems have also been experimentally investigated. The experiment was carried out on the ion projection lithography system in IMS by P. W. H. de Jager and coworkers.[14] They also gave a fitted empirical equation:

$$d_{CI} = \frac{\left(\frac{I}{I_c}\right)^p \cdot \left(\frac{m}{m_{es}}\right)^{p/2} \cdot \left(\frac{f}{f_{es}}\right)}{\left(\frac{V}{V_c}\right)^{1+p/2} \cdot \left(\frac{\alpha}{\alpha_{es}}\right) \cdot \left(\frac{dc}{dc_{es}}\right)^q} \tag{3-20}$$

The subscript "es" and "c" are referred to some constants, and dc means the diameter of the cross-over. p is close to 2/3 in the equation. If the charged interactions are taken into account on their 258 keV IPL system, the attainable He^+ beam current for 50 nm node is about 1.84 μA if the angle of the beam is 45 mrad at the cross-over and the focal length is 196 mm.

3.5.3 Stochastic ion-ion interactions in MMRL system

Even though several analytical or empirical equations have been reported for the trajectory displacement effect, these equations are different with each other because of the different optics models and the different computational methods used in the simulations. It is extremely difficult to precisely predict the trajectory displacement effect with an analytical equation for ion projection systems because the ion energy is not constant in electrostatic lens. However, the dependences of the charged particle interactions on ion current, beam energy, column length, and beam half angle are similar for most systems. The dependence of the trajectory displacement effect with ion energy and current is the same in equation (3-17), (3-18) and (3-20).

MMRL is a special ion projection lithography system with final beam energy of 75 keV. Based on the allowable current on a 258 keV IPL system reported by de Jager and equation (3-17,18,20),[14] the maximum attainable beam current for MMRL will be lower than 0.35 μA for He^+ assuming similar optical condition. Actually, the beam energy is extremely low around the pattern generator plane in MMRL, and it is much less than 75 keV in most parts of the ion optics column in MMRL, as shown in fig. 3.18. This will definitely increases the charge interactions a lot. MMRL relies on limiting aperture

to obtain a small beam half angle and improve the system resolution. Thus, a lot of large-angled ion beams will be blocked by the limiting aperture. But the blocked ion current can still increase the charged particle interactions along the beam path before the limiting aperture. If these factors are taking into account, the maximum He^+ beam current in MMRL might be lower than 0.35 μA for 50 nm resolution. The above analysis indicates that the charged particle interaction effects are very challenging issues for MMRL system.

3.6 The throughput of MMRL system

Conventional optical lithography system can print one layer on 300 mm wafer in about one minute. Even though maskless lithography eliminates the non-recurring cost on expensive masks, the target throughput for maskless lithography systems still needs to be more than 10 wafer-per-hour (WPH) on 300 mm wafers in order to be competitive with the conventional optical lithography for medium and low volume production. There are still lots of challenges to be investigated in order to obtain the targeted throughput for the sub 50-nm nodes, such as the particle-particle interactions, the speed of the high precision mechanical stages, and the attainable data rate for pattern generators, etc.

3.6.1 Maximum allowable current and source brightness

The analysis of the ion-ion interactions indicates that the maximum helium ion current on MMRL should be less than 0.35 μA for sub 50 nm nodes. Based on the aberrations simulation result in fig. 3.14, the optimized MMRL optical column can be operated with 1.0 mrad image side beam half angle on 0.25 mm exposure field. The corresponding beam brightness at the wafer plane will be:

$$B = \frac{I}{S \times \pi \times \alpha^2} = \frac{0.35 \cdot 10^{-6}}{0.025 \times 0.025 \times 3.14159 \times 0.001^2} = 178 \text{ A/cm}^2\text{sr} \qquad (3\text{-}21)$$

Q. Ji has experimentally demonstrated that the brightness of a multicusp He^+ ion source can be as high as 440 A/cm^{2}sr at 2.0 keV ion energy,[15] which corresponds to a brightness of 16,500 A/cm^{2}sr at 75 keV. Even though lens aberrations and ion-ion interactions along the beam path will reduce the beam brightness on the wafer plane, it is still not difficult to obtain a brightness of 178 A/cm^{2}sr at the wafer plane in MMRL. So the source brightness is not the bottleneck to the throughput for MMRL.

If the required dose to expose a chemical amplified resist is 1.0 μC/cm^2 and half of the area on wafer needs to be exposed, then the total exposure time (beam-on time) for a 300 mm wafer can be calculated as:

$$\frac{\pi \cdot 15^2 \cdot 10^{-6} \cdot 0.5}{0.35 \cdot 10^{-6}} = 1009.8 \text{ seconds} \qquad (3\text{-}22)$$

This means that the maximum throughput on the current prototype MMRL system is less than 3.6 WPH if the beam settling time and mechanical stage traveling and alignment time are negligible.

The maximum allowable current is determined by charged particle interactions. There are two possible approaches to increase the allowable current for MMRL.

1) **Increasing operation voltage in MMRL.** Stochastic coulombic interactions are inversely proportional to beam energy to the power of 4/3. If the beam voltage is increased to 163 kV, the allowable current will be increased to 1.0 μA. The maximum possible throughput will be 10 WPH. If the operating voltage is further increased to 273.4 kV, the current can be as high as 2.0 μA. The throughput can be improved to 20 WPH (only considering the exposure time). There is a potential challenge in increasing the operating voltage of MMRL. If the electric field around the DPG is too high, then the electric field will penetrate into the aperture, as illustrated in fig. 3.9. It will strongly focus the incoming low energy ions and greatly increase the beam half angle after ions are extracted out of the apertures. Then a lot of the current will be blocked by the limiting aperture on the cross-over plane. In order to keep the same amount of current on the wafer plane, the total current before the limiting aperture has to be increased, and it might increase the space charge effect before the limiting aperture. This is a trade-off that needs to be investigated.

2) **Employing quadrupole lens to decrease ion-ion interactions at the cross-over**. Quadrupole lens has the property of focusing in one direction and defocusing in the perpendicular direction. With more than two quadrupole lenses, a focused image in both directions can be formed on an image plane, as illustrated in fig. 3.31. The cross-overs in this kind of multipole optics will be straight lines instead of a point.[16] Consequently, the charged particle interactions in the cross-over will be greatly reduced. But multipole lens can

also induce non-symmetric beam aberrations. Also, the magnifications in the two perpendicular planes of the multipole lens optics are different. The feasibility of using multipole lens for high-resolution projection optics still needs to be investigated through extensive simulations and experiments.

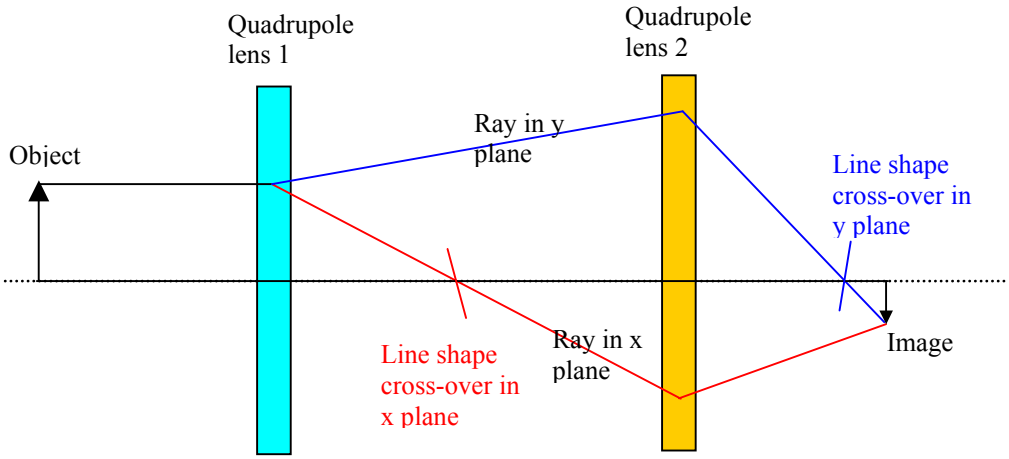

Figure 3.31. The schematic of image formation using double quadrupole lenses.

3.6.2 Requirement on mechanical stage at different writing modes

3.6.2.1 Stitch-step mode

There are two possible writing modes for MMRL. The first one is the stitch-step mode as illustrated in fig. 3.33. This mode of operation consists of two steps. First, all the

exposure features within several small sub-fields are stitched together to form a large major field. Then a mechanical stage will move the wafer by a step distance.

There is a certain pitch distance between the switching apertures in the pattern generator (fig. 3.32). Beam scanning unit must be incorporated in order to expose all the areas that need to be patterned. Stitching deflectors control the beam stitching within a small sub-field. Electrostatic deflector should be used as stitching deflector because of its high speed. Main-field deflector will deflect the ion beam from one sub-field to the neighboring one. Because of the large deflection distance within the main-field, magnetic deflector is a more suitable choice as the main-field deflector.

After a main field is exposed, the mechanical stage will move the wafer to the next adjacent main field. One die on the chip can be formed by several main fields. Even though the sub-field size is 0.25×0.25 mm^2 in the prototyping MMRL system, the stepping distance is the same as the main field size, which can be much larger than the sub-field size. When the stage is stepping from a main field to the adjacent one, it takes certain time for the stage to accelerate, travel, decelerate and settle at the next field. If the main field size is 1.0×1.0 mm^2, then the stage needs to step 70686 times to cover the whole area on a 300 mm wafer. Assuming that it takes 0.1 second for the mechanical stage to move one step, the total time to cover a 300 mm wafer will be 7069 seconds. It is comparable to the exposure time (beam-on time) calculated in section 3.6.1.

In order to reduce the stage stepping time, the size of the main field has to be increased. The total stepping time is inversely proportional to the square of the main field size. If the main field can be increased to 10×10 mm^2, the total stepping time for a 300 mm wafer can be reduced to about 1.17 minutes assuming the single stepping time is 0.1

seconds. However, it might be very challenging for the mechanical stage to accelerate, decelerate and travel for 10 mm within 0.1 second while maintaining a spatial precision as high as 10 nm or better. It might be very difficult to achieve high throughput in stitch-step mode because of the small field size in charged particle optics.

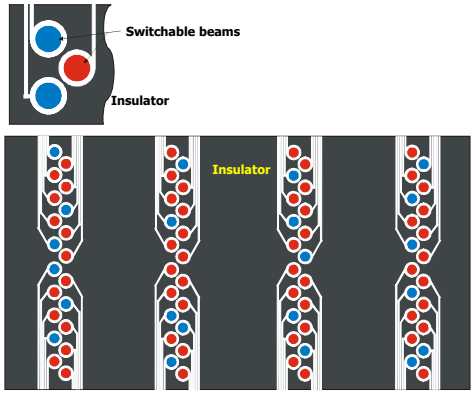

Figure 3.32. An illustrative switching aperture layout design in a pattern generator.[1]

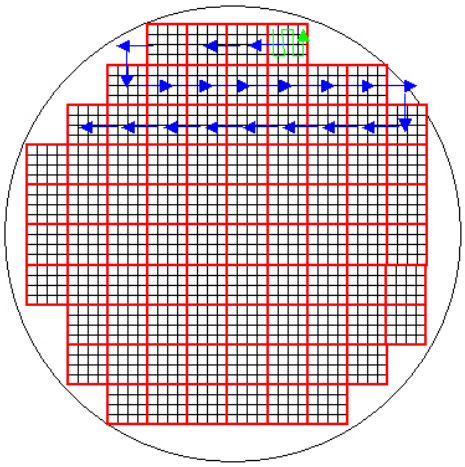

Figure 3.33. Illustration of the stitch-step mode. Small grids represent sub-fields. Red thick grids represent main fields. Stitching deflectors can fill the ion beam over all the areas in a sub-field. Green line represents the deflection generated by the main-field deflectors among the small sub-fields. Blue arrows indicate the movement of the mechanical stage.

3.6.2.2 Swath mode

In order to overcome the issue of frequent stage acceleration and deceleration in stitch-step mode, maskless lithography systems can also be operated in swath mode. In this mode, the stage will move with a constant speed while sweeping across the wafer in

one direction. When the ion beam moves out of the exposure area on wafer, the stage will be decelerated and accelerated in the opposite direction after stepping to the perpendicular direction with a distance equal to the width of the beam swath. So the ion beam will expose a long strip across the wafer during one step.

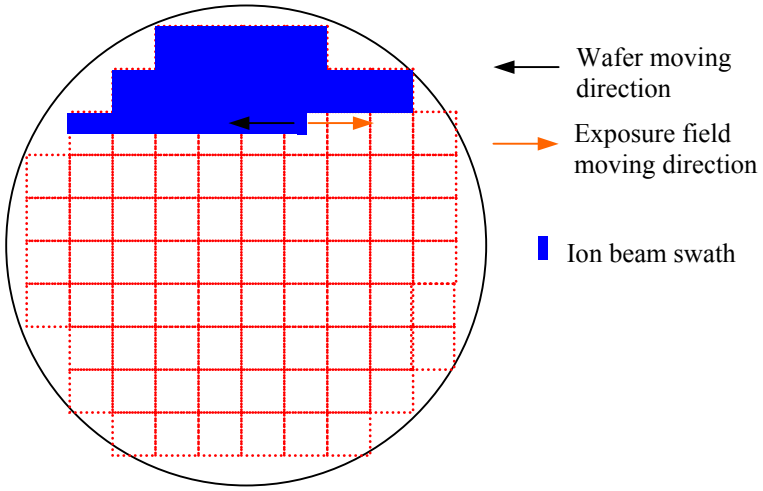

Figure 3.32. Illustration of the swath mode operation.

There are several characteristics in this mode of operation. First, the stage travels at a constant speed during one step. The speed of the stage is determined by the total ion current and the width of the swath. If the width of the swath is d in cm, the total ion current is I in μA and the dose is D in μC/cm^2, then the speed of the stage is determined by the following equation:

$$v = \frac{I}{d \cdot D} \quad \text{(cm/s)} \tag{3-23}$$

Suppose I =0.35μA, d =0.025cm and D=1.0 μC/cm^2, the velocity of the stage should be 14.0 cm/s. In order to cover all the area on a 300 mm wafer, the stage needs to accelerate and decelerate for 300/0.25= 1200 times. This is much less than that of the stitch-step

mode. If the width of the swath is further increased to 1.0 mm, the number of times that the stage reverses will be decreased to 300. And the speed will also be decreased by 4 times if the total current is the same. Large exposure field size will greatly relax the requirement on the mechanical stages.

Second, one pixel on the wafer can be exposed by many times when the beam swath passes through the wafer. This kind of operation can average out the variation of the current coming out from different switching apertures. Also, the redundancy in exposure can tolerate some defective switching apertures along a row on pattern generator. If there are 1000 switching apertures in one row on pattern generator and 10 of them are defective, the variation of the dose for a pixel on the wafer is still as low as 1%.

Grey level exposure in swath mode can be realized with two methods. First, the current from each switching aperture can be changed by adjusting the applied biasing voltage. If the biasing voltage can be coded to 256 levels, the exposure dose can also have 256 grey levels. Second, the dose of a certain pixel on the wafer can be controlled by varying the number of the switched-ON apertures when they pass through the pixel on the wafer.

In general, the requirement of the mechanical stage is much more realizable in the swath mode than that of the stitch-step mode. In order to improve the throughput of MMRL, the total current and the exposure field size has to be increased.

3.7 Conclusions

Lens aberrations on the MMRL system has been re-evaluated based on a more accurate ion optics model. It revealed that inaccurate initial ion energy and erroneous beam half angle used in Vinh V. Ngo simulation had caused the discrepancy between his simulation and the experimental results. Based on the new analysis, a limiting aperture has been incorporated into the MMRL ion optics column. With a field-free limiting aperture of 100 μm in diameter, MMRL can readily print sub-100 nm features on PMMA resist. Besides the reduction of lens aberrations, resolution capability can also be affected by the DC earth magnetic field and the AC electro-magnetic interference (EMI). These interferences have been discussed in detail, and solutions to reduce them have been presented.

In order to obtain a throughput better than 10 WPH, Ion current of several micro-amps is required in MMRL. Qualitative analysis to the ion-ion interactions has been carried out on a simple physics model. It agrees surprisingly well with the results obtained from the extended two-particle theory and the Monte-Carlo simulations reported by other research groups. Due to the high mass of ions, the maximum allowable current on the prototype MMRL system might be lower than 0.35 μA for 50 nm node. Small exposure field size in charged particle lithography might also limit the throughput of MMRL, because it will take significant amount of time for the mechanical stage to accelerate, decelerate and travel for many times. The requirement on the mechanical stage can be relaxed in a swath mode operation. But the maximum allowable ion current and the exposure field size must be increased in order to obtain the targeted throughput---10 WPH on 300 mm wafers.

Reference

[1] V.V. Ngo, "Experimental demonstration of a Prototype Maskless Micro-ion-beam Reduction Lithography System",Ph.D. Thesis, Unversity of California 2005.

[2] Eric Munro, "Computer programs for the design and optimization of electron and ion beam lithography systems", Nuclear Instruments and Methods in Physics Research A **258**, 443 (1987).

[3] P.W. Hawkers and E. Kasper, "Principle of electron optics: Basic Geometrical Optics". (1989).

[4] H.C. Chu and Eric Munro, "Numerical analysis of electron beam lithography systems. Part III: Calculation of the optical properties of electron focusing systems and dual-channel deflection systems with combined magnetic and electrostatic fields", Optik **61** (2), 121 (1981); Eric Munro, "Numerical modelling of electron and ion optics on personal computers", Journal of Vacuum Science and Technology B **8** (6), 1657 (1990).

[5] Eric Munro, in *Handbook of CHARGED PARTICLE OPTICS*, edited by Jon Orloff (CRC, 1997), Vol. 1.

[6] Eric Munro, Xieqing Zhu, John Rouse et al.,"Aberration analysis of wide-angle deflectors and lenses by direct ray-tracing, and comparison with conventional aberration theories" presented at the Preceedings of SPIE Conference on Charged Particle Optics, San Diego, California,SPIE,2522,(1995).

[7] V.V. Ngo, W. Barletta, R. Gough et al., "Maskless Micro-ion-beam reduction lithography", Journal of Vacuum Science and Technology B **17** (6), 2783 (1999).

[8] V.V. Ngo, B. Akker, K. N. Leung et al., "Demonstrations of electronic pattern switching and 10X pattern demagnification in a maskless microion-beam reduction lithography system ", Journal of Vacuum Science and Technology B **21** (6), 2297 (2003).

[9] X. M. Jiang, Q. Ji, L. L. Ji et al., "Resolution improvement for a maskless microion beam reduction lithography system ", Journal of vacuum Science and Technology B **21** (6), 2724 (2003).

[10] Pieter Kruit and Guus H. Jasen, in *Handbook of Charged Particle Optics*, edited by Jon Orloff (CRC, 1997), Vol. 7.

[11] Liqun Han, W. Dan Meisburger, R. Fabian W. Pease et al.,"The global Space Charge Effects In High Throughput Electron Beam Lithography" presented at the Proceedings of SPIE conference on Charged Particle Optics IV SPIE,37777,192(1999).

[12] G. H. Jansen, "Trajectory displacement effect in particle projection lithography systems: Modifications to the extended two-particle theory and Monte Carlo simulation technique", Journal of Applied Physics **84** (8), 4549 (1998).

[13] S. D. Berger, D. J. Eaglessham, R. C. Farrow et al., "Particle-particle interaction effects in image projection lithography systems", Journal of Vacuum Science and Technology B **11** (6), 2294 (1993).

[14] P. W. H. de Jager, G. Derksen, and B. Mertens, "Experimental results of the stochastic coulomb interaction in ion projection lithography", Journal of Vacuum Science and Technology B **17** (6), 3098 (1999).

[15] Q. Ji, X. Jiang, T.-J. King et al., "Improvement in brightness of multicusp-plasma ion source", Journal of Vacuum Science and Technology B **20** (6), 2717 (2002).

[16] Yuichiro Yamazaki, Osamu Nagano, Susumu Hashimato et al., "Electron optics using multipole lenses for a low energy electron beam direct writing system", Journal of Vacuum Science and Technology B **20** (1), 25 (2001).

Chapter 4

Pattern generator development for MMRL

4.1 Introduction

Traditional electron beam lithography with a single Gaussian round beam or a shaped beam is inherently a maskless lithography approach.[1] But the improvement of the exposure pixel rate on the traditional electron beam maskless lithography systems can not keep up with the pace of Moore's law.[2] The throughput of the fastest electron beam direct-write systems available today is lower than 0.1 WPH for 300 mm wafers. More parallel exposure scheme must be incorporated to improve the throughput, such as the adoption of multiple individually controllable beamlets. If the brightness of each beamlet is the same as that of the single Gaussian beam in a traditional direct-write system, ignoring the effect of charged particle interactions and neglecting the possible limitations

set by other sub-systems, then the attainable throughput will be multiplied by the number of total beamlets.

Charged particle maskless lithography techniques have been reviewed in Chapter 1. Multiple beamlets can be generated through either a multi-source approach or a single-source approach. In the first approach, multiple sources can be generated by multiple field emission sources, such as the MCC system developed by Advantest,[3] or multiple photoelectron sources modulated by laser beams, such as DIVA[4] system developed in Stanford University and the multiple beam system developed by Etec.[5] While in the second approach, multiple beamlets are usually generated through a so-called aperture plate system (APS). First, an electron beam emitted from a field-emission source will be accelerated to several keV and then expanded by an illumination column to illuminate the first aperture plate on APS, which has many square aperture patterns with a certain pitch distance. Multiple patterned electron beam-lets can be generated after the illuminating electrons pass through the first aperture plate. They can be individually switched on and off by the blanking electrodes addressed on the second aperture plate. The deflection voltage applied to the blanking electrodes can be generated by laser illuminated photo-diodes--- such as the system developed by MAPPER lithography in Delft, the Netherlands,[6] or by the embedded CMOS circuit---such as the PML2 system developed by IMS in Vienna Austria.[7] The electron beamlets deflected by the second aperture plate will be blocked by a third aperture plate or by a downstream limiting aperture placed at the cross-over position in the optics column. Because the electron beam has been accelerated to several keV before arriving at the first aperture plate, the APS is subjected to a high thermal load because of the electron beam heating.

MMRL is also a multiple-beam maskless lithography system. It has a unique way of generating multiple individually controllable ion beamlets due to the fact that it directly places a pattern generator in front of a plasma source. The multi-cusp plasma ion source for MMRL can produce a uniform plasma within an area of 19 cm in diameter. A microfabricated pattern generator with many patterned apertures and switching electrodes is directly placed under the plasma source. The energy of the ions drifting out from the plasma sheath, can be lower than 10 eV if the plasma potential is well controlled. Therefore ion or electron heating and damage of the pattern generator due to ion sputtering can be minimized. A retarding potential of 10 volt applied to the switching electrodes will be sufficient to shut-off the ion current. The development of a microfabricated pattern generator for MMRL will be discussed in this chapter.

4.2 Previous research on the multiple switchable aperture system

Multiple ion beam switching through a multi-aperture extraction system had been demonstrated by Y. Lee on a filament-driven plasma ion source in 2000.[8] The picture of the multi-aperture extraction system is shown on the left side graph of fig. 4.1. It consists of two copper layers and a plastic insulator layer in between. The thickness of all the

three layers is 50 μm. One side of the copper layer was patterned into individually addressed switching electrodes. Switching apertures with diameter of 40 μm were mechanically drilled through the three layers. The ion source body was biased to positive 30 volt in order to extract ion current to ground potential, as shown in the right side graph of fig. 4.1. Negative 50 volt with respect to the source wall was applied to the first copper layer in order to prevent the primary electrons from being collected by the Faraday cup. Only 4 watt of discharge power was used to generate the plasma, so the plasma density and the plasma potential were extremely low in the experiment. A positive 31-volt with respect to the ground potential applied on the second metal layer was sufficient to repel most of the ions. Since the source body was biased to positive 30 volt with respect to the ground, the potential barrier was only 1.0 volt. This means that the plasma potential should be lower than 1.0 volt in her experiment. The ion current measured from the 9 apertures at ON and OFF states has been plotted in fig. 4.2.

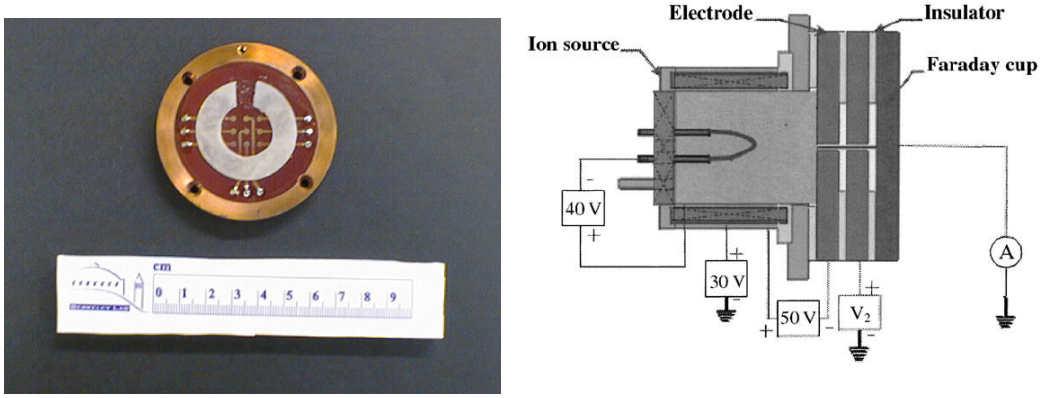

Figure 4.1 Mechanically fabricated multi-aperture extraction system and the experimental setup for the switching experiment.[9]

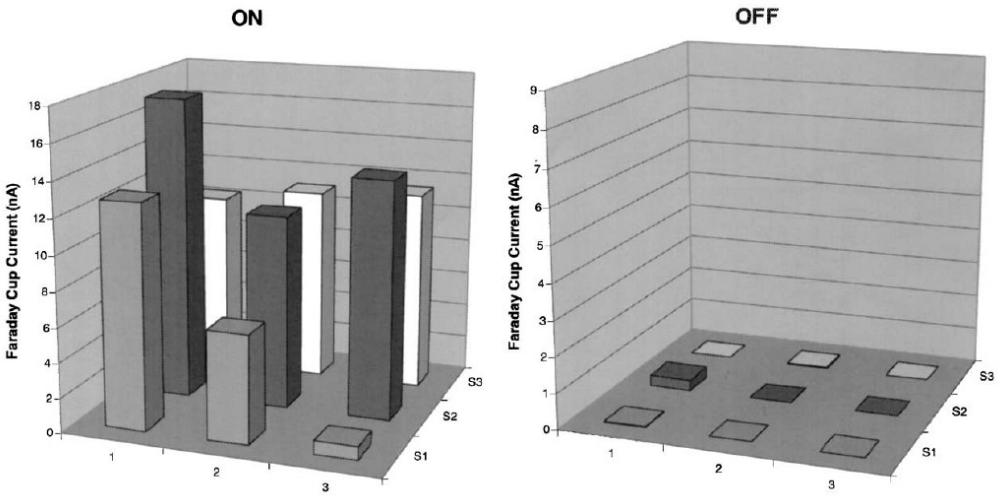

Figure 4.2 Ion current measured on the 9-channel switching apertures in ON and OFF state.[9]

The experiment discussed above has demonstrated the switching capability of a mechanically machined multiple-aperture extraction system operated under an extremely weak filament-driven plasma. Filament driven ion sources can cause serious contamination problem because the tungsten filament can evaporate and deposit on the pattern generator. An rf driven plasma source is more appropriate for this application.

It is well-known that a filament-driven plasma is relatively more stable than an rf-driven plasma. And the plasma potential of an rf generated plasma is usually higher than that of a filament discharge plasma. Besides the above issues, much higher discharge power will be input into the rf ion source of MMRL during a normal operation condition in order to obtain an acceptable throughput. Plasma potential usually increases with the input rf power. So it is expectable that beam switching will be more challenging if a

pattern generator is operated under an rf-driven plasma source with a relatively high input power. Additionally, in order to print features less than 100 nm in maskless mode, the diameter of the apertures should be smaller than 1.0 μm with the 10X reduction optics column in MMRL. Then the pattern generator must be fabricated by microfabrication processes.

This chapter will describe the development of a microfabricated pattern generator that can be operated with an rf plasma ion source at a relatively high input power. Even though it seems to be very straightforward to incorporate the pattern generator into a system with an accelerating and focusing column, some unexpected problems actually arose during the integration process. These problems will be investigated.

Even though the design and the fabrication of a microfabricated pattern generator has been described in Vinh V. Ngo's Ph.D. thesis,[9] there is no successful experimental result demonstrating the switching capability. Thus, the development of the microfabricated pattern generator will begin with a simple one in the current thesis work. Then the design will be optimized based on the experimental results obtained in previous steps.

4.3 Beam switching experiment with the 1st version micro-fabricated pattern generator on an rf-driven ion source

As discussed in the previous section, the plasma potential of an rf-driven plasma ion source can be higher than that of a filament driven ion source. It can also increase

with the input rf power. The objective of the experiment in this section is to demonstrate the switching capability of a micro-fabricated pattern generator on an rf driven plasma ion source without any downstream ion accelerating and focusing column.

4.3.1 Structure and fabrication process flow of the 1st version microfabricated pattern generator

In order to reduce the complexity of the fabrication process, the first microfabricated pattern generator only consists of two metal layers and a 1.0 μm-thick insulator layer in between. The structure of the pattern generator is shown in fig. 4.3 (a). Only 9 apertures were patterned in the first microfabricated pattern generator (fig. 4.3 (b~c)). The fabrication process flow is presented in fig. 4.4.

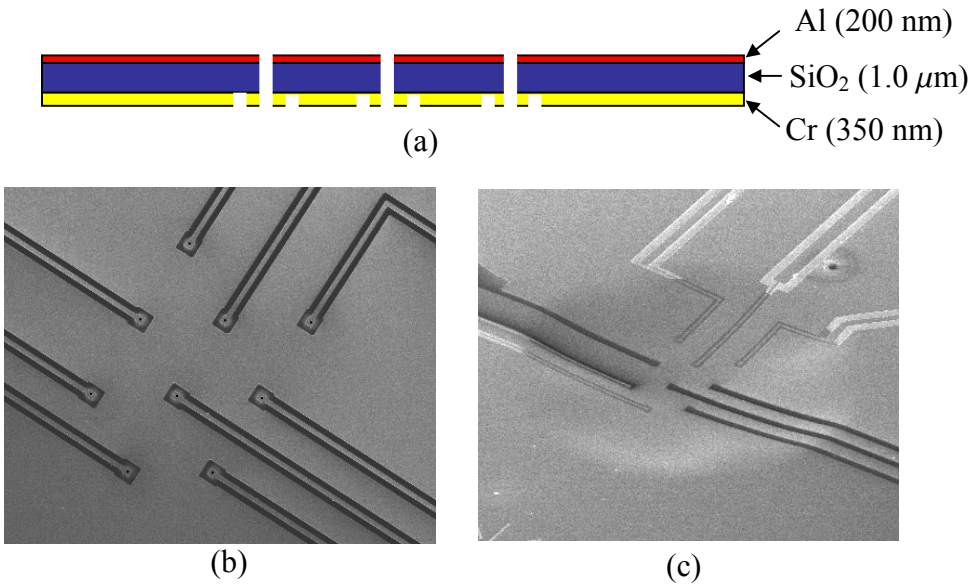

Figure 4.3. (a) The structure of a microfabricated pattern generator with two metal layers and a SiO_2 layer. (b) The top view of the 9-hole pattern generator imaging with focused ion beam system. (c) SEM image of the 9-hole pattern generator when the electron beam is tilted to 54°.

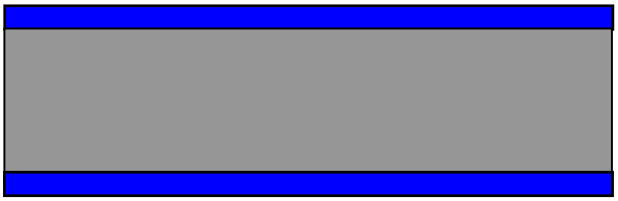

(a) Wet oxidation 1μm SiO_2 on bare silicon wafer

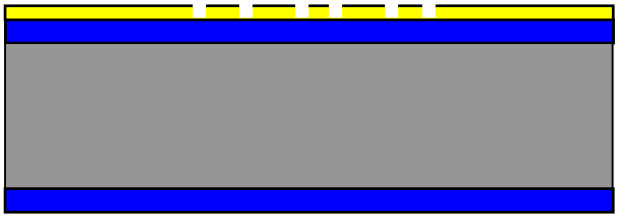

(b) Deposit 350 nm-thick chromium metal. And pattern the connection wires and switching pads.

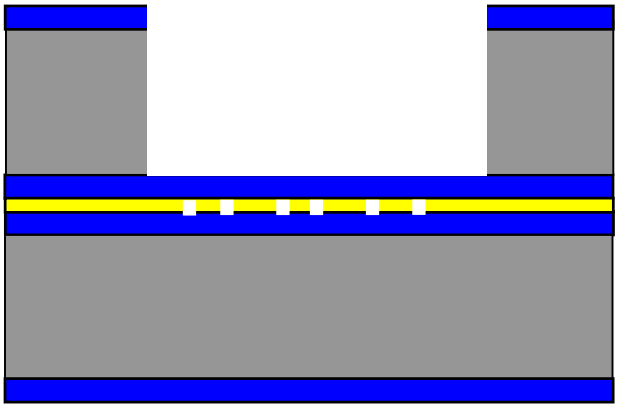

(c) Pattern the backside window using STS through-wafer etching. The front side of the wafer has been bonded to an oxidized wafer to protect the metal from exposing to the plasma.

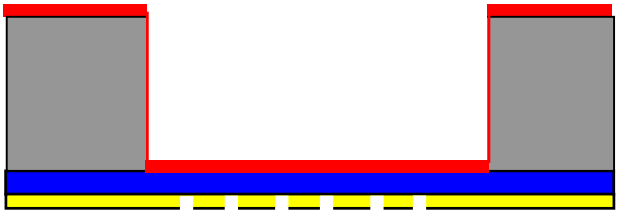

(d) Back-side aluminum deposition

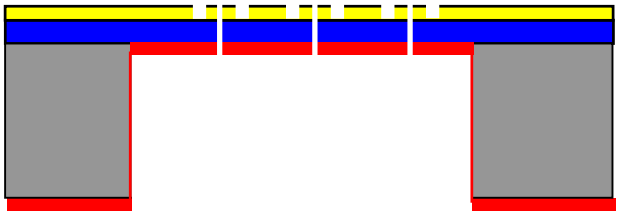

(e) Switching apertures are drilled through the membrane by using a FIB tool

Figure 4.4 Fabrication process flow for the 9-hole pattern generator shown in fig. 4.3

The silicon dioxide membrane is formed by means of a wet-oxidation process at a temperature of 750^{o}C (fig. 4.4). The process-induced stress will deform the membrane after it is released (fig. 4.3 (c)). It is possible to reduce the process-induced stress by replacing the oxide layer with a layer of low-stress nitride deposited by a PECVD process, which is usually carried out at relatively low temperature. The backside window is etched by a RIE (Reactive Ion Etch) process in STS (Surface Technology System), which will create a very steep sidewall. It is very difficult for aluminum to cover the steep sidewall. The pattern generator design and fabrication process flow will be further optimized after the proof-of-concept ion beamlet switching is successfully demonstrated.

4.3.2 Experimental setup and result of ion beam switching

The pattern generator substrate wafer was cut into dies of about 1.0×1.0 cm^2 after the microfabrication process was completed. It was then assembled onto a PCB board that has many patterned connection wires (fig. 4.5 (a)). Most of the areas on the PCB board are covered by a layer of insulating paint, except for the exposed copper wires that were bonded to the pattern generator and the soldering contacts connected to a multiple-channel voltage supply. The multi-channel bias voltages were generated by two 8-channel fieldpoint modules. The pattern generator chip and the PCB board were attached onto a 4" copper plate, which directly face the plasma during the experiment. There is a large hole in the center of the copper plate, which is aligned with the active area on the pattern generator, so that ion beam can drift out from the pattern generator.

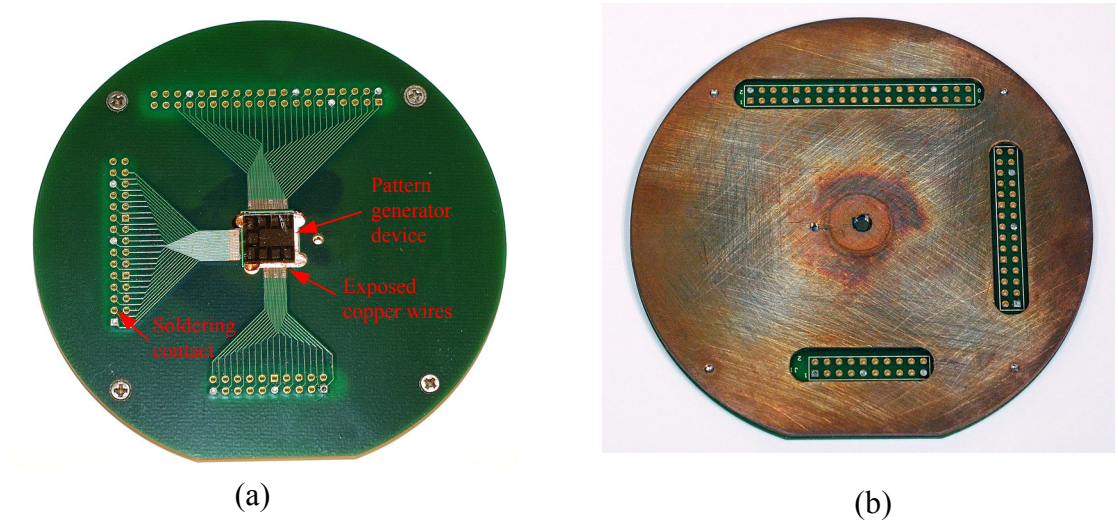

(a) (b)

Figure 4.5. The pattern generator assembly used in the experiment. (a) The contact pads on the pattern generator are bonded onto the copper wires on the PCB board. (b) The backside of the pattern generator is attached to a copper plate, which will be directly placed in front of the plasma.

The experiment was performed on an inductively coupled rf-driven plasma source with an external antenna (fig. 4.6). The back-plate and the front-plate of the ion source chamber are made of aluminum. The ion source chamber is made of pyrex glass tube with an outer diameter of 13 cm. A Faraday shield was incorporated into the antenna design to reduce capacitive coupling discharge, which might result in a high plasma potential. One pair of strong permanent magnets were installed at the exit of the plasma source as an filter to reduce the plasma loss rate. The magnetic field between the two magnets is about 400 Gauss. The permanent magnets in the back-plate can also confine the plasma. Sine there are only 9 apertures with diameter of 1.0 μm to extract ion beam, a channeltron ion detector was used to amplify the ion current signal during the experiment.

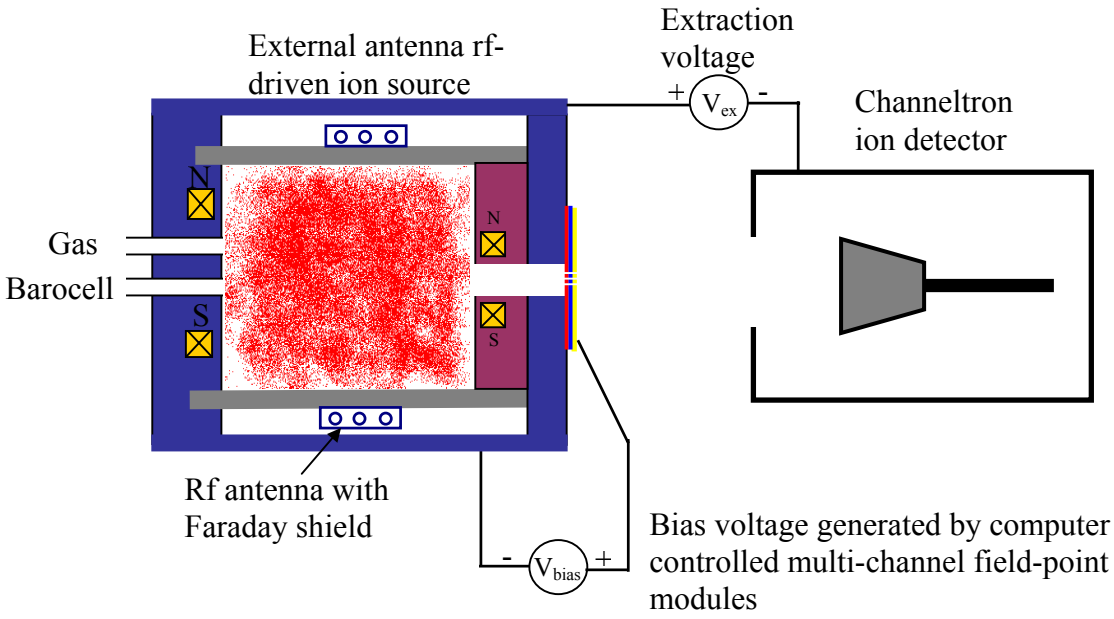

Figure 4.6. Experimental setup of ion beamlet switching experiment on an inductively coupled plasma (ICP) ion source.

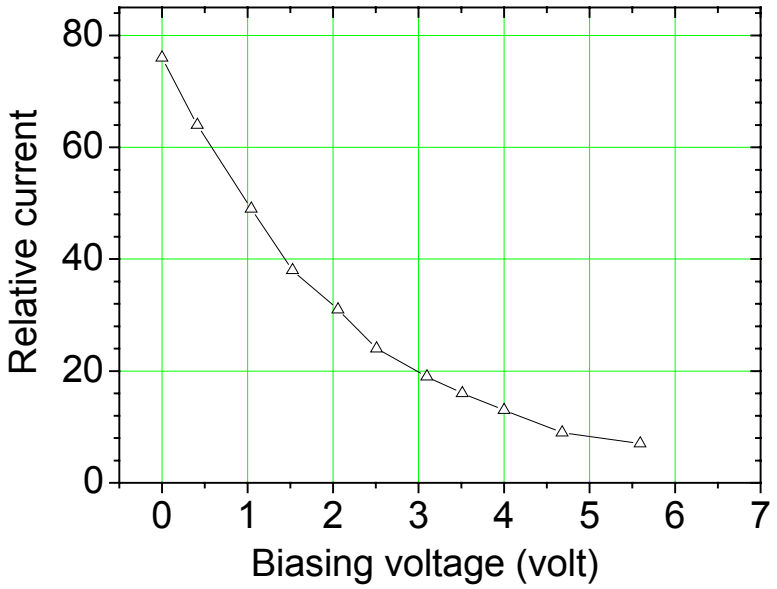

Figure 4.7. Ion current versus the bias voltage applied on the switching apertures

Ion beamlet switching experiment has been carried out under various plasma operation conditions. But it is only successfully demonstrated when the ion source is operated in a low-power high-pressure weak plasma mode. Under this condition, the light of the plasma is so weak that it is barely visible in a totally dark environment. The experimental result in fig. 4.7 was obtained at an rf power of 50 watt and a neutral gas pressure of 500 mTorr (argon). The ion current can be reduced to 10% by applying a positive bias voltage of 5 volt. The remaining background current could be the dark-current of the channeltron detector. If the plasma ion source works in a bright mode, positive 10 volt-bias voltage almost has no effect on the collected ion current. In addition, the patterned chromium wires and the switching electrodes can be easily damaged in the bright plasma mode because the positive bias voltage can extract very high electron current from the plasma.

The ion current from each aperture can be obtained by subtracting the current measured when the aperture is switched OFF from the current measured when all the apertures are ON. The result has been plotted in fig. 4.8. A statistical analysis to the nine data points gives a mean value of 0.2 and a standard deviation of 0.034. The maximum deviation is observed on channel 6, which is 30% less than the average current. The uniformity of the current is directly related to the shape of the apertures patterned in the membrane. It is a very important issue for lithography process control. It can be improved by adjusting the voltage applied on different apertures, so that the currents from all apertures are the same in the ON state. A lookup table containing the correction voltages for every channel must be supplied to the pattern generation computer during a maskless lithography process.

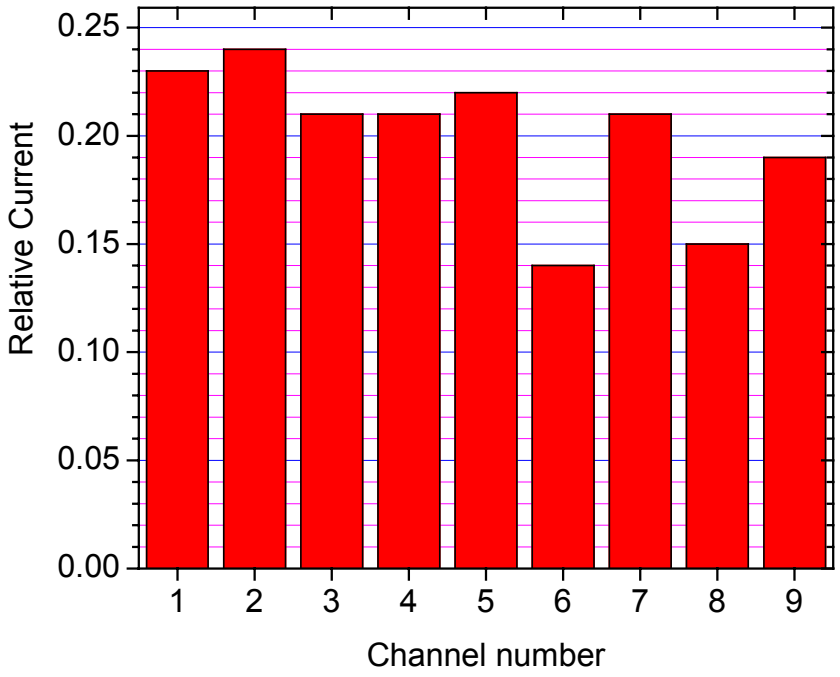

Figure 4.8 Ion current from different apertures.

4.3.3 Damage of the apertures during experiment

The diameter of all the switching apertures on the pattern generator was about 1.0 μm before the experiment. After the pattern generator had been operated for one hour or so (plasma was on), it is very clear to see that some of the apertures were enlarged (fig. 4.9). The damage to the apertures could be attributed to arcing inside the apertures. Since the pattern generator directly faced the plasma ion source, the pressure inside the

apertures was very close to that of the plasma ion source, which is very suitable for discharge to occur. When plasma is on, both ions and electrons will exist in the switching apertures. If a bias voltage is applied between the two metal layers, discharge can be easily triggered inside the apertures. It can damage the aperture because of the heat generated by the arcing and the possible ion bombardment on the sidewalls. The stability and the lifetime of the pattern generator under the harsh environment of plasma is still an important issue that needs further investigations.

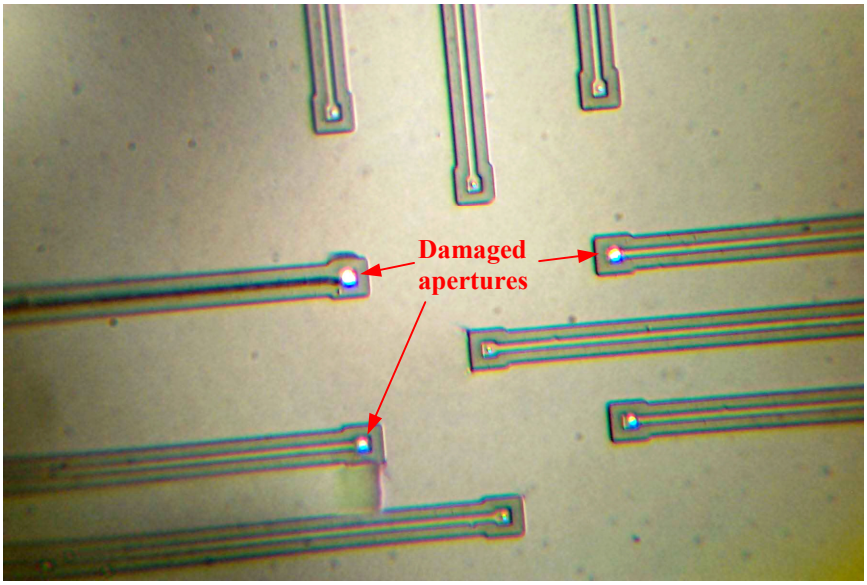

Figure 4.9. Damage to the switching apertures during operation.

4.4 Integration of a three-layer pattern generator in the MMRL

If the plasma source in fig. 4.6 works in a high density bright mode, the three-layer pattern generator shown in fig. 4.3 can not switch off the ion current completely by a positive 10 volt bias voltage. A possible explanation could be the high plasma potential in the plasma source with an external antenna due to the lack of plasma confinement on the sidewall. The ion source for MMRL is a multi-cusp, rf-driven inductively coupled plasma source (fig. 2.8 in chapter 2). The geometry of the antenna has been optimized to reduce the energy spread. And the permanent magnets embedded in the ion source body can effectively confine the electrons from losing to the source wall. Consequently, the plasma potential in the ion source of MMRL could be much lower than that of the ion source shown in fig. 4.5 under the same input rf power. Thus, it might be easier to switch off the ion beamlets in the MMRL ion source with a relatively high plasma density.

4.4.1 Fabrication process flow for the 2nd version microfabricated pattern generator

A new three-layer pattern generator similar to the one shown in fig. 4.3 had been fabricated for the integrated experiment carried out on MMRL. The insulating layer in the 2nd version pattern generator has been replaced with low-stress silicon nitride (LSN) because of the better film quality, the low process-induced stress in the PECVD process and the resistance to KOH wet-etch. A new process flow is presented in fig. 4.10. Chromium was been chosen as the top metal layer because of the good adhesion

properties and the resistance to KOH wet-etch. KOH wet-etch process on the (100) surface of the silicon wafer can form a slope with an angle of 57.5^{o}, which results in a relatively gentle sidewall than the RIE silicon etch process. The most difficult steps in the fabrication process are step (e) and step (f), because it is quite difficult to clean the aluminum inside the apertures from the front side. This is the reason why only 50 nm-thick aluminum was deposited on the back of the pattern generator.

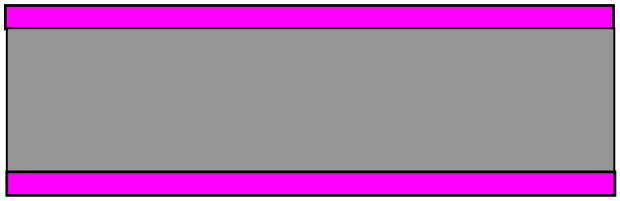

(a) Sub-atmospheric CVD to form 1.0 μm low stress nitride (LSN).

(b) Chromium deposition and patterning the isolation trenches to form the connection wires and the switching electrodes

(c) Pattern the switching apertures through the chromium layer and the silicon nitride layer using chromium wet etch process and silicon nitride plasma etch.

(d) Pattern the backside window into LSN layer and etch through the silicon wafer in KOH.

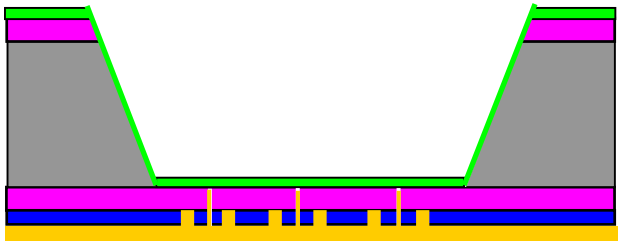

(e) Shield the frontside chromium wires and the patterned switching apertures with photoresist. Then deposit 50 nm aluminum on the backside of the wafer.

(f) Using aluminum wet-etch and plasma RIE aluminum etch to clean the aluminum deposited inside the switching apertures. The backside aluminum layer is protected by photoresist

Figure 4.10. Microfabrication process flow for the 2nd version pattern generator with LSN film

It is very difficult to install a channeltron detector into the MMRL system. Consequently, a Faraday cup will be used to measure the ion current. In order to obtain a measurable ion current, 162 switching apertures were patterned in the new pattern generator (fig. 4.11). They are divided into 9 groups. Each group is connected to a channel on the field-point modules.

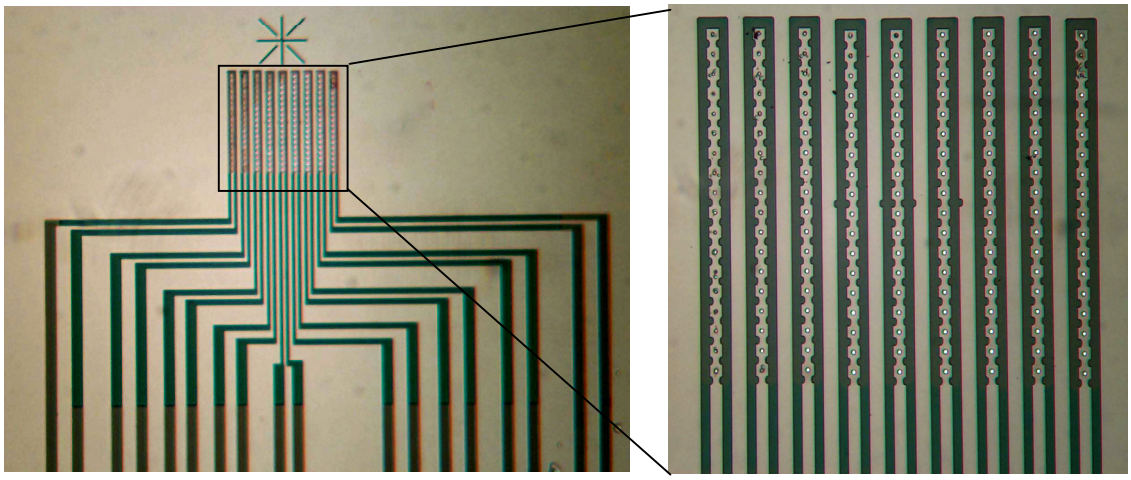

(a) (b)

Figure 4.11. (a) The second version microfabricated pattern generator. (b) The enlarged view of the 192 apertures.

4.4.2 Beam switching experiment with the new three-layer pattern generator

The second version of microfabricated pattern generator was installed in a similar assembly as the one shown in fig. 4.5. During the ion beamlet switching experiment on MMRL, a strange phenomenon was observed. Compared with the experiment discussed in section 4.3, the 2nd version three-layer microfabricated pattern generator is extremely easy to be damaged during the operation in MMRL. One of the damaged pattern generator is shown in fig. 4.12. Usually, very obvious arcing marks can be observed

between the patterned chromium wires and through the insulating layer between the chromium and the aluminum layers.

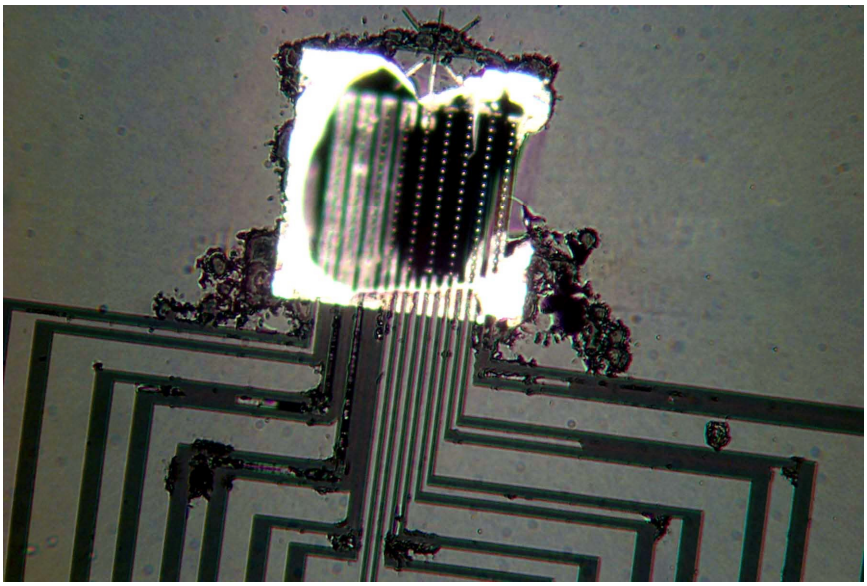

Figure 4.12 Damaged pattern generator when the plasma is on and a positive bias voltage is applied to the chromium layer.

Even though the damage to the switching apertures has been observed in the experiment discussed in the last section (fig. 4.9), the membrane was still unbroken. There must be some other reasons that caused the serious damages to the pattern generator when it was operated in the MMRL. In order to make sure that the low stress nitride film can hold the bias voltage applied between the two metal layers, a newly fabricated pattern generator was tested in a gas pressure same as the operating pressure in the ion source before the plasma is started. The low stress nitride film and the chromium wires remain intact even after a bias voltage as high as 20 volt was applied to the switching electrodes.

After months of studies under different plasma operating conditions and electrode biasing conditions, the suspect was finally narrowed down to the back-streaming secondary electrons. Secondary electrons are generated when the high-energy ions impinge on the limiting aperture or the resist on the wafers. Once generated, they will see an accelerating voltage toward the pattern generator plane (fig. 4.13). The final energy of the secondary electrons—when arriving at the pattern generator plane---can be higher than 60 kV. Even though most of the secondary electrons generated at the wafer plane are blocked by the limiting aperture, those that can pass through will arrive at the pattern generator plane with energy of 75 keV.

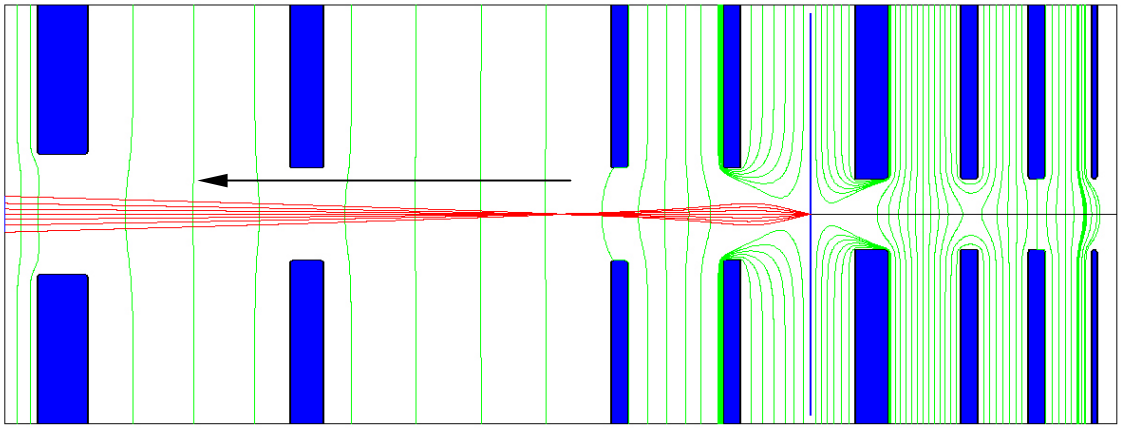

Figure 4.13 Secondary electron generated at the limiting aperture plane will be accelerated toward the pattern generator plane

Electrons with energy higher than 65 keV can easily penetrate through the device layer of the microfabricated pattern generator. Monte Carlo simulation to the electron penetration process is presented in fig. 4.14. Circles along the electron path represent the collisions between the incoming electron and the substrate. The simulation was carried out in a program called CASINO. Along the trajectories inside the LSN layer, incoming

electrons will knock out some electrons from the molecular bonds through inelastic collisions. When a bias voltage (about 10 volt) is applied to the chromium and the aluminum layers, the free electrons knocked out by the incoming high-energy electrons can move along the path of the radiation damage. They will be accelerated and will knock out more free electrons along the path. Thus, arcing will be initialized through the LSN layer. It can eventually damage the whole membrane, as shown in fig. 4.12. Then the patterned chromium wires will be exposed to the plasma. They can extract very high electron current because of the positive bias voltage. This can overheat the chromium wires and make them peel off from the LSN film. In addition, the low energy electrons diffusing out from the plasma can also trigger arcing between the pattern chromium wires.

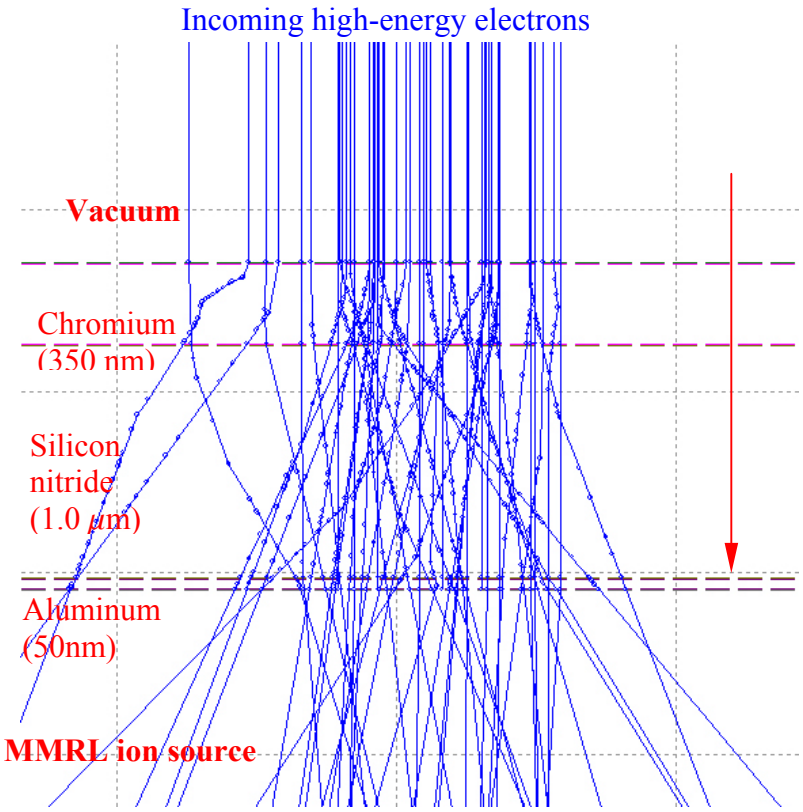

Figure 4.14 Penetration of the secondary electrons (65 keV) through the pattern generator. Small circles represent collisions inside the materials.

4.5 Ion beamlet switching in the MMRL with the 3rd version of microfabricated pattern generator

As discussed in section 4.4, high-energy secondary electrons emitted from the limiting aperture plane or from the wafer plane can trigger arcing across the low stress nitride layer in the second version microfabricated pattern generator. In order to improve the stability of the microfabricated pattern generator, a 10~20 μm-thick intrinsic silicon layer will be incorporated into the third version design. Because the positively biased chromium wires can extract very high electron current from the plasma, a new operation scheme will be implemented in the following experiment to resolve this problem.

4.5.1 Structure of the 3rd version pattern generator and a new operation scheme

The structure of the third version microfabricated pattern generator is similar to the second version, except that the insulation layer has been extended by adding a layer of intrinsic silicon with thickness of 10~20 μm. The cross-sectional view of the pattern generator has been plotted in fig. 4.15 together with the ion source of the MMRL system. The connection wires and the switching pads are patterned in the chromium layer. Beam switching is accomplished by applying a positive bias voltage to the chromium electrodes at the exit of the apertures. Gold or copper might be a better choice as the material for the switching electrodes because they are also resistant to KOH wet etching and have much higher conductance than chromium. But the complexity of the fabrication process will increase because of their poor adhesion properties to the silicon nitride layer.

Since the total thickness of the insulation layer has been increased by 10~20 times, the electric field will be decreased by 10~20 times. Even though the electrons with energy higher than 65 keV can still penetrate 20 μm-thick silicon layer and cause radiation damage, the electric field isn't strong enough to trigger avalanche breakdown. High aspect-ratio apertures in the silicon layer are etched by a RIE process. They can collimate the incoming ion beams so that the large-angled ions, which will not pass through the downstream limiting aperture, will be blocked before entering the column space. This can help to reduce the total current along the ion optical column before the limiting aperture and minimize the space charge effect.

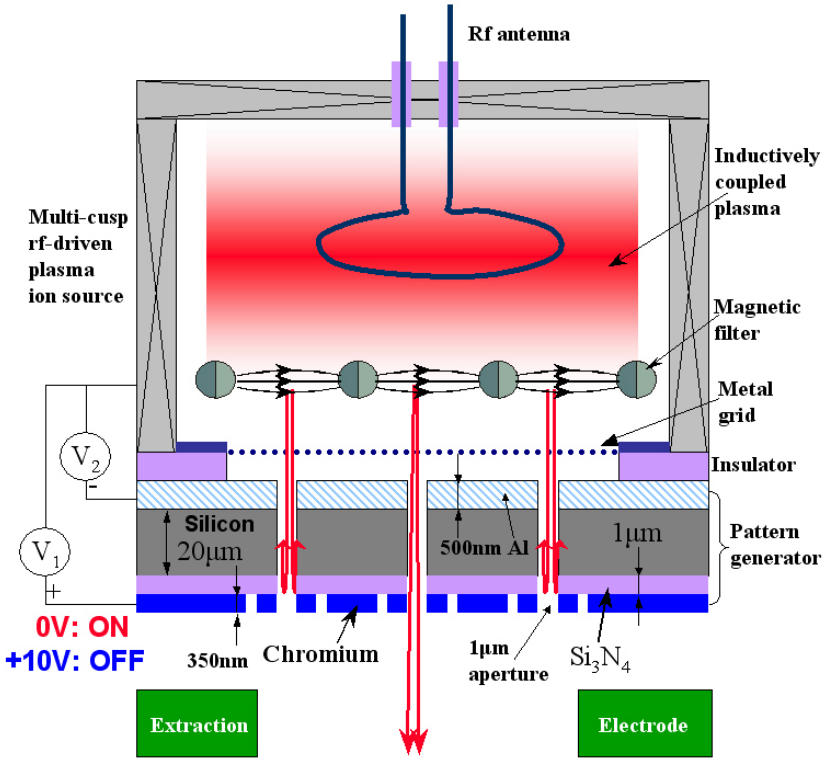

Figure 4.15. Structure of the microfabricated pattern generator and its operation scheme on MMRL ion source.

The cross-sectional view of the ion source is also shown in fig. 4.15. It's an rf-driven multi-cusp plasma ion source with magnetic filter. The ion source works in inductively coupled mode. The permanent magnets embedded in the source wall, the backplate and the magnetic filter are installed with alternative polarities, so that multi-cusp magnetic fields can be formed at the peripheral of the plasma to confine the plasma. This will substantially decrease the plasma potential.

The ion source and the patter generator are drawn together so that the operation scheme can be clearly shown (fig. 4.15). When the positive bias voltage is applied to the switching electrodes on the pattern generator, it will extract very high electron current and damage the switching pads and the connection wires, especially when the plasma density is high. In order to reduce the electron current, the aluminum layer on the pattern generator has been biased negatively with respect to the plasma ion source, e.g. V_2 in fig. 4.15. Very fine metal mesh has been placed between the pattern generator and the ion source to define a uniform plasma sheath boundary. Beamlet switching voltage (V_1) is applied to the chromium electrodes at the exit of the apertures. If the electron current is sufficiently suppressed by the negative bias voltage--V_2, the chromium wires won't collect much ion or electron current in both ON and OFF states. Ideally, the required switching voltage V_1 should be independent of V_2 and should only be determined by the plasma potential and the ion temperature.

4.5.2 Fabrication process for the 3rd version pattern generator

The 3rd version microfabricated pattern generator was fabricated in the Microfabrication Laboratory of UC-Berkeley. A self-aligned fabrication process flow is presented in fig. 4.16. First, 1.0 μm-thick low stress nitride was deposited on both sides of a bare silicon wafer in a low-pressure CVD furnace (step a). Then 350 nm-thick chromium was deposited through a plasma sputter deposition process. The chromium layer was then patterned into individually addressed electrodes by optical lithography and wet etching processes (step b). The layout of the patterned chromium wires is the same as the one shown in fig. 4.11.

After the switching electrodes and connection wires were patterned, 2.0 μm thick G-line resist was spin-coated on top of the wafer. Then apertures with diameter of 1.0 μm were patterned into the resist through a 10X reduction optical stepper. This is the only step that requires alignment. The 2.0 μm-thick G-line resist was used as the mask for the subsequent chromium wet etching, plasma dry etching of the LSN layer and the deep reactive ion etching (DRIE) into the silicon layer. The etch selectivity of LSN over resist is about 1.5. Fortunately, the etch selectivity of silicon to resist in DRIE process is as high as 100. As a result, it is still possible to etch apertures with depth over 10.0 μm into the silicon layer by using the 2.0 μm-thick resist as the mask. However, it's very challenging to obtain good uniformity in patterning and etching the high aspect ratio apertures with diameter of 1.0 μm in the Berkeley Microlab.

After step C, square windows were patterned in the backside LSN, which was used as a mask for the subsequent KOH wet-etch till the patterned apertures were exposed. Before KOH wet etching, a dual layer of G-line (2.0 μm thick) and SU-8 (50.0

μm) resists were coated on top of the wafer. Then the SU-8 resist will be cured at 180^0C for one hour to cross-link the polymer. This hard polymer layer is resistant to KOH wet etch, so that it will protect the patterned apertures in silicon from KOH. The G-line resist under the SU-8 resist is a cushion to protect the underlying features. Fully cured SU-8 resist is very difficult to be etched away. When the subsequent KOH wet-etching process was completed, the SU-8 resist was cut into many pieces by using a sharp razor blade. Then the whole wafer was immersed in a PRS-3000 bath to etch away the underlying G-line resist. After that, the hard-baked SU-8 resist can be easily peeled off.

a) Low stress nitride deposition on bare silicon

b) Deposit chromium on top of LSN and pattern the isolation trenches in chromium

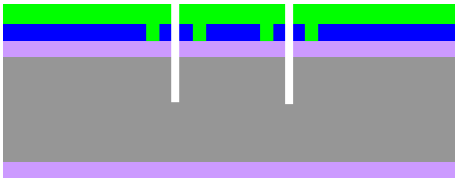

c) Pattern apertures through chromium, LSN and silicon by wet-etch, plasma etch, and STS DRIE

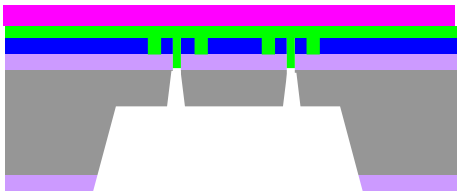

d) Pattern the backside LSN and KOH wet etch silicon till the apertures are open. The front side is protected by photoresist and 50μm cured SU-8.

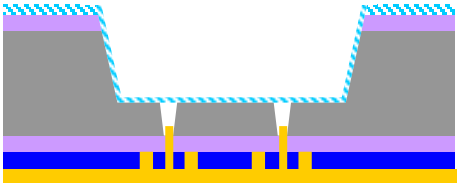

e) Deposit aluminum on the baskside using thermal evaporation while the switching apertures are partially protected by PR.

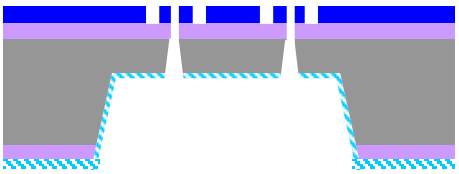

f) Clean the aluminum in apertures from the frontside using the apertures as mask.

Figure 4.16 Microfabrication process flow for the 3rd version pattern generator

The etching rate of silicon in a 1:3 KOH-DI bath at 85^0C is about 1.5 μm per minute. In order to protect the apertures patterned in the silicon layer, the silicon wafer was pulled out immediately after the apertures were exposed to the KOH solution. Due to the non-uniformity among the patterned apertures, some deeply etched apertures were exposed to the KOH solution earlier, so that their sidewalls were etched more than the others. One possible solution to this problem is to perform the KOH etching before patterning the apertures. But a 10~20 μm thick silicon membrane is usually too fragile under the vacuum chuck in the photoresist coaters and the photolithography steppers. If the process wafer is bonded onto a dummy wafer to protect the silicon membrane, it can not be processed by the 10X GCA wafer stepper in the Microfabrication Laboratory because of the increased total wafer thickness.

After the step (d), a layer of aluminum with thickness less than 100 nm will be coated on the backside of the wafer through a thermal evaporation process, which is a directional deposition process. The aspect ratio of the apertures in silicon is high. Consequently, there is not much aluminum deposited on the sidewall of the apertures. An additional aluminum wet etch and RIE plasma etch should be sufficient to clean the aluminum deposited on the sidewalls (step f). The finished pattern generator has the same layout as the one shown in fig. 4.11.

4.5.3 Experimental result and discussion

Because of the increased thickness and the decreased electric field strength in the insulating layer, no electrical breakdown was observed during the experiment, even though the high-energy electron radiation still existed. In order to prevent the positively biased switching electrodes from extracting very high electron current, a negative bias of –5 volt (V_2 in fig. 4.15) has been applied to the aluminum layer to repel the electrons back to the plasma. Because of the above improvements, ion beam switching on a microfabricated pattern generator was finally successfully demonstrated on MMRL for the first time. The plasma ion source in the current experiment worked in a high-density bright mode.

Ion beam switching experiments have been carried out when the ion source was operated at different rf power and different neutral gas pressures. In order to compare the switching voltages at different conditions, the measured ion current has been normalized to about the same magnitudes by multiplying different ratios listed in the inserted text label. The amplitude of the switching voltage is directly proportional to the plasma potential. High rf power can increase the electron temperature and the plasma density. As a result, the plasma potential tends to be higher with increased rf input power. Thus 12~13 volt is required to totally shut-off the ion current at an input rf power of 250 watt. High neutral gas pressure can reduce the electron temperature and lower the plasma potential. Consequently, the solid lines (58.5 mTorr pressure) are located at the left side of the dashed lines (27.6 mTorr) for the same rf powers.

In order to totally shut off the ion current, a bias voltage higher than 10 volt is required on the microfabricated pattern generator. But V. V. Ngo gave a result which

indicated that only 1.5 volt positive bias voltage can switch off the ion current upon using a mechanically drilled single-aperture ion beam switching device. It's hard to believe that the plasma potential can change 10 times under similar operation conditions in the same ion source. The difference in switching voltage could be attributed to the structure of the pattern generator.

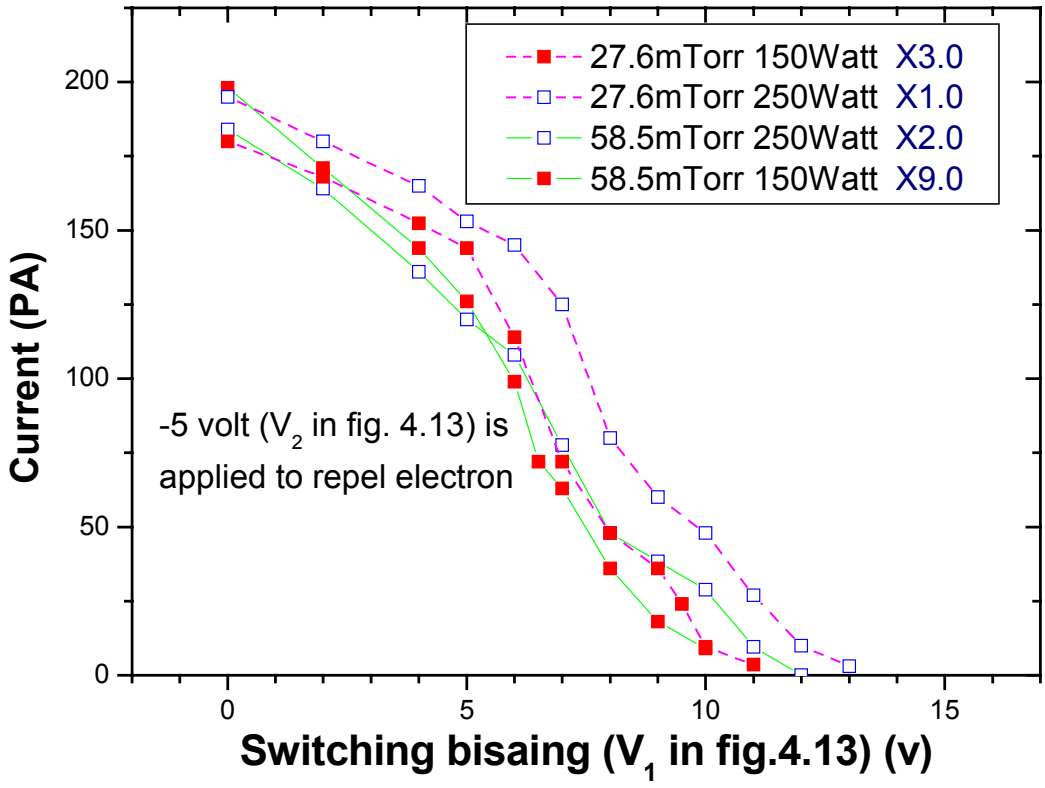

Figure 4.17 Ion beam switching results at different rf power and operation pressure

If electrons are totally blocked by the negative voltage applied on the aluminum layer, then the sidewall of the high-aspect-ratio apertures will be positively charged by the ions (fig. 4.18). The surface charge on the sidewall will create an energy barrier for the incoming ions. Whenever V_1 is zero (ON state) or +10 volt (OFF state), there always exists an electric field towards the aluminum layer because of the negative bias voltage—V_2. This will further increase the height of the energy barrier. Even though the incoming ions will be accelerated by 5 eV before entering the apertures, they will be decelerated inside the apertures. The energy barrier may block some of the low energy ions from passing through the apertures. This may generate four effects:

1) Since the low energy ions are blocked by the energy barrier (fig. 4.18 (b~d)), only the high-energy ions can pass through the apertures. Consequently, relatively high bias voltage (V_1) is required to totally shut off the ion current. This could be part of the reason for the high switching voltage observed in the experiment.
2) As shown in fig. 4.16 (d), the low-energy ions can't pass through the energy barrier. So the total ion current passing through insulating channels will be lower than the current passing through conductive channels. Lowering the negative bias voltage may let some electrons with relatively higher energy to neutralize the positive charge along the sidewall of the apertures.
3) The surface charge along the sidewall may trigger arcing between the two metal layers.
4) Surface charge will scatter the ions passing through the channels, thus increase the angle of the ion beams. It will decrease the amplitude of the current that can pass through the limiting aperture.

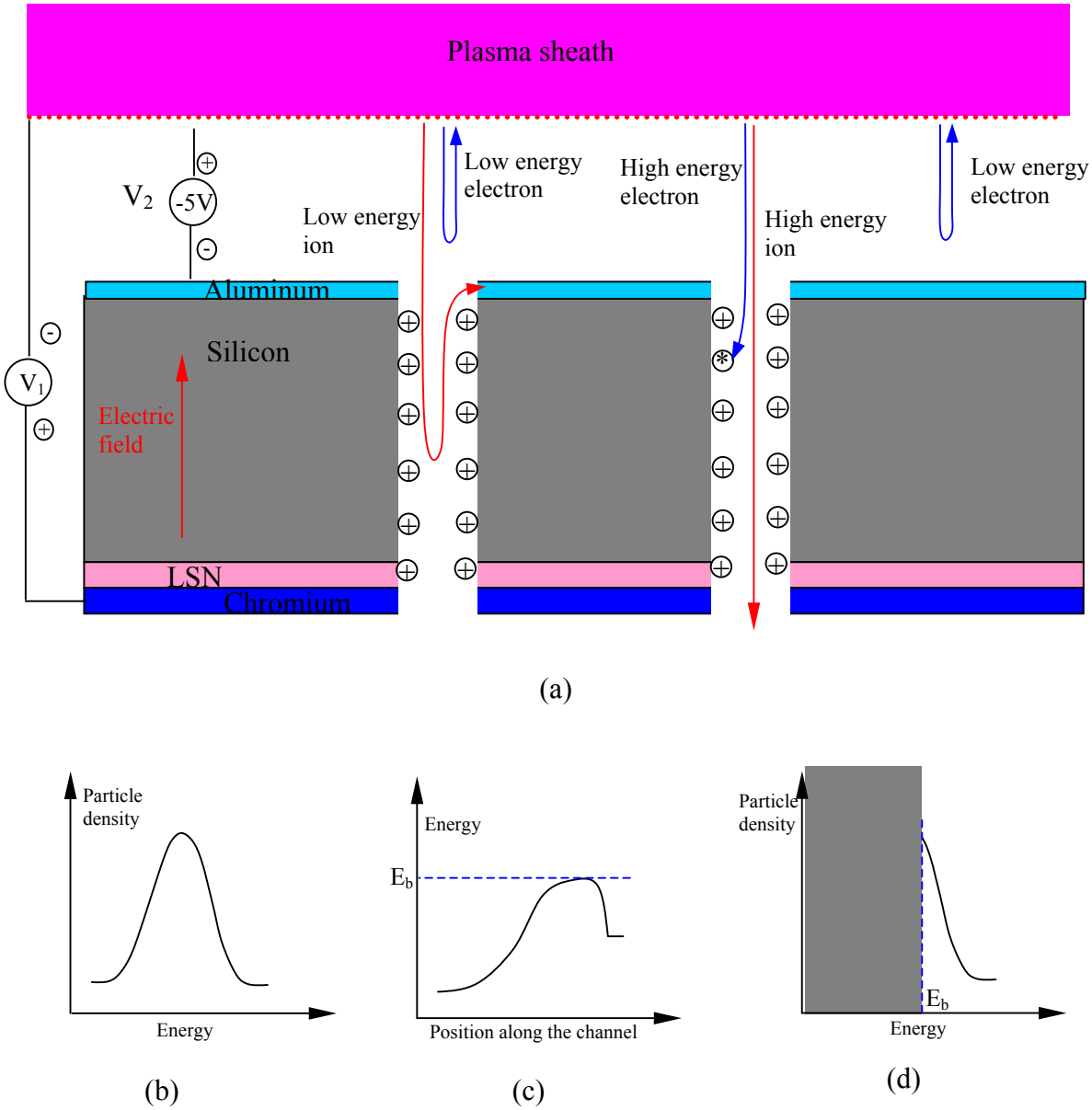

Figure 4.18 (a) Ion transportation through high aspect ratio apertures in the insulation layer of the pattern generator. (b) Initial ion energy distribution. (c) Energy barrier along the channel. (d) Final ion energy distribution after passing through energy barrier plotted in (c).

4.6 Problems observed during ion beam exposure with the microfabricated pattern generator

Since the 3rd version microfabricated pattern generator has successfully demonstrated ion beamlet switching on MMRL, it would be interesting to expose resist while switching ion beamlets ON and OFF. Due to the low ion current measured by the Faraday cup, the limiting aperture wasn't installed in the column for the first exposure test. Total current of 100 pA can be measured under this condition. No exposure image was observed even after 20~30 seconds ion beam exposure on the PMMA resist. Ignoring aberrations, the image should be 192 apertures with diameter of 100 nm in the resist. If an ordinary mask was used, an exposure time less than 0.5 second is enough to expose the PMMA resist even with a limiting aperture of 100 μm in diameter installed in the optics column (fig. 3.21). The possible explanations could be:

1) Ion optics might have been changed because of possible malfunctions on some high voltage power supplies.
2) The images of the apertures are too small to be found on a 4" wafer.
3) The aberrations of the image are too large. Thus the ion current was actually distributed over very large spots on the wafer. So the dose was still not enough even with 20~30 seconds exposure. If the required dose to expose a PMMA resist is 20 μC/cm^2, the total radiation dose with 100 pA ion current for 20 seconds will be sufficient to expose 192 apertures with diameter of 8 μm on the resist. If the reason is because of the large aberrations, the actual image size should be much larger than 8 μm.

4) The electric field distribution at the pattern generator plane could have been strongly disturbed. The pattern generator was bonded to a PCB (fig. 4.5). The substrate of the PCB board is insulative, which can't define a flat electric field around the pattern generator plane. Thus, the electric field distribution could deviate from the ideal case, which may cause out-of-focus problem to the image.

The first possible cause was eliminated by carefully calibrating the voltage on each electrode. Exposure test with an ordinary mask confirmed that the optics condition defined by the electrostatic electrodes is still functional as before.

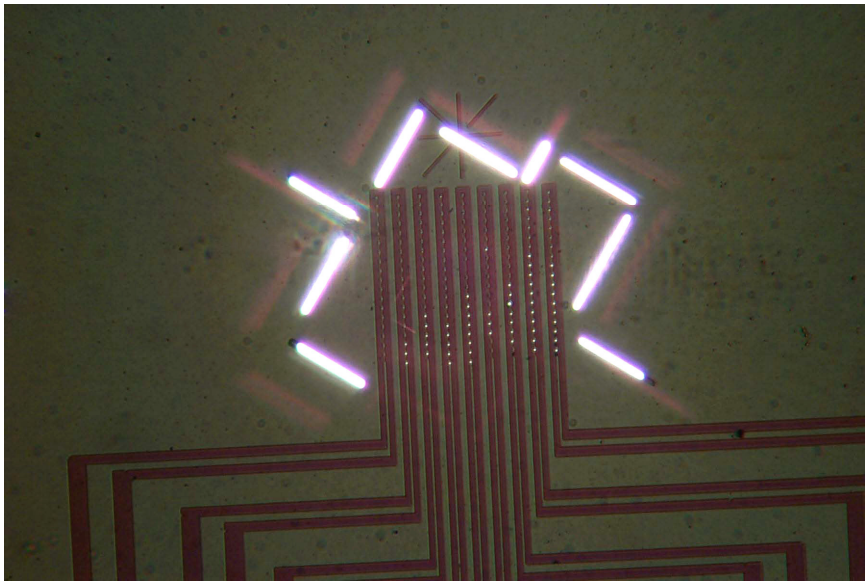

Fig. 4.19 Long trenches have been drilled into the pattern generator to produce observable marks on the resist in order to locate the small aperture images.

In order to make sure that the exposed image can be observed if it does exist, trenches of 100 μm long and 5 μm wide were drilled into the membrane of the pattern

generator (fig. 4.19). But there is still no exposed image observed on the resist after the modification. Then, the whole device area on the pattern generator (300×300 μm^2) was totally cut away. Ideally, the image should be a square with size of 30×30 μm^2 on the wafer. But the exposure result—without a limiting aperture in the column---showed that 2/3 of the whole 4" wafer was exposed. The above result indicated that the ion optics had changed a lot from the normal operation condition. Since the voltages on the electrostatic electrodes haven't been changed, the cause can only comes from the pattern generator plane.

Ion beam exposure experiments have successfully demonstrated 50 nm resolution using ordinary stencil masks made of conductive materials. Usually, the ordinary stencil masks and the supporting holders are all conductive materials. But the pattern generator was bonded onto a PCB board (fig. 4.5). Most of the areas on the PCB board are insulative. In order to obtain a similar optics condition as the ordinary masks, a layer of aluminum was evaporated onto the PCB board. But there must exist some exposed copper wires including the insulator between the wires on the PCB board, so that they can be bonded to the contact pads on the pattern generator. Besides the above change, 20 square patterns with size of 15×15 μm^2 have been drilled in the pattern generator membrane in order to increase the total current. After the above modifications, the new assembly was installed into the MMRL again. In the meantime, a limiting aperture with diameter of 100 μm was installed in the ion optics column to reduce the aberrations.

A strange phenomenon was observed during the ion current measurement experiment. The initial ion current collected by the Faraday cup was about 250 pA when

the plasma was just started. But the ion current will totally disappear within 1 or 2 seconds of operation if the voltage applied on the limiting aperture is 11,560 volt.

The above experimental observation is very similar with charging a capacitor. Actually, it is caused by charging on the insulating surface of the pattern generator. Secondary electrons emitted at the limiting aperture plane will hit at the pattern generator plane with energy of 65 keV. They can charge up the exposed insulator on the pattern generator chip and on the PCB board. Surface charging will change the electric field distribution around the pattern generator plane. The axial accelerating electric field generated by the ion optics column is only 50 volt/mm at the pattern generator plane. The energy of the ions coming out from the ion source could be lower than 10 eV in this region. Consequently, ion trajectories are very sensitive to the surface charging on the pattern generator plane. The imaging condition can be totally disturbed by the surface charging. It can also deflect the ion beams so that it can not pass through the limiting aperture on the cross-over plane.

The interaction between the surface charges and the low energy ions has been simulated on the EO3D code package from MEBS^{TM}. The result is plotted in fig. 4.20. The energy of the incoming ion is 10.0 eV. Assuming the surface charging generates an electrostatic potential of positive 1.0 volt at the exposed insulator surface, as indicated by the red area in fig. 4.20, the incoming ions can be deflected to an angle of 84 mrad. The deflected ion will be blocked by the limiting aperture installed at the cross-over position of the column. This explains why the current collected by the Faraday cup decreased so rapidly in the experiment.

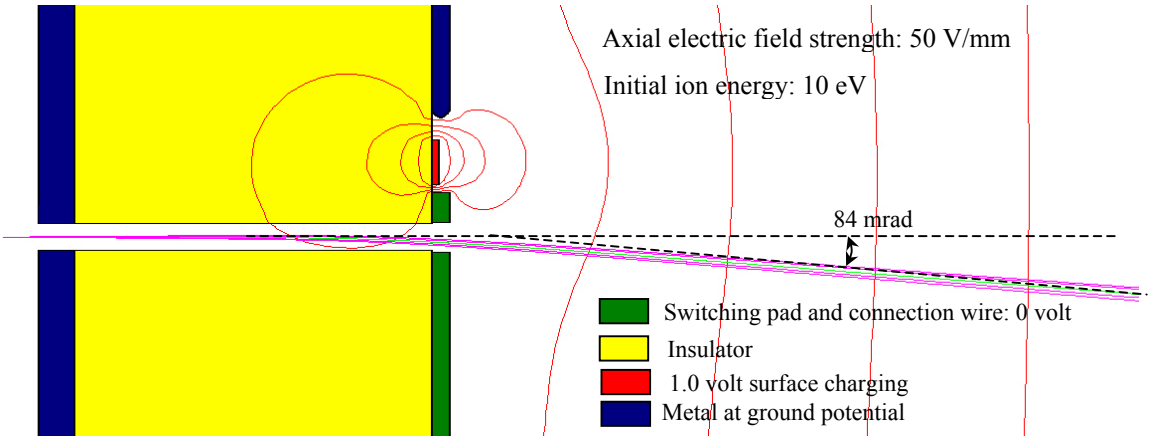

Figure 4.20. Surface charging generates an electrostatic potential of 1.0 volt at an exposed insulator surface, which will deflect the incoming ion beam with energy of 10.0 eV to an off-axis angle of 84 mrad.

4.6.1 Can secondary electrons be eliminated?

A lot of the secondary electrons (SE) are emitted from the limiting aperture plane because most of the ions are blocked by it. Simulation in fig. 4.21 shows that a SE trap can be created around the limiting aperture plane by increasing the voltage applied on it. If the voltage on the limiting aperture (V_a) is increased to 14,000 volt, SE with energy lower than 1.0 keV can be pulled back to the limiting aperture plate. The initial energy of most of the SEs should be lower than 30 eV.[10] Consequently, SE trap can effectively trap most of the SEs generated at the limiting aperture plane and prevent the high-energy electron from reaching the pattern generator. Unfortunately, if V_a deviates from 11,560 volt, the field-free region around the limiting aperture plane will be destroyed, which may generate additional aberrations as discussed in chapter 3.

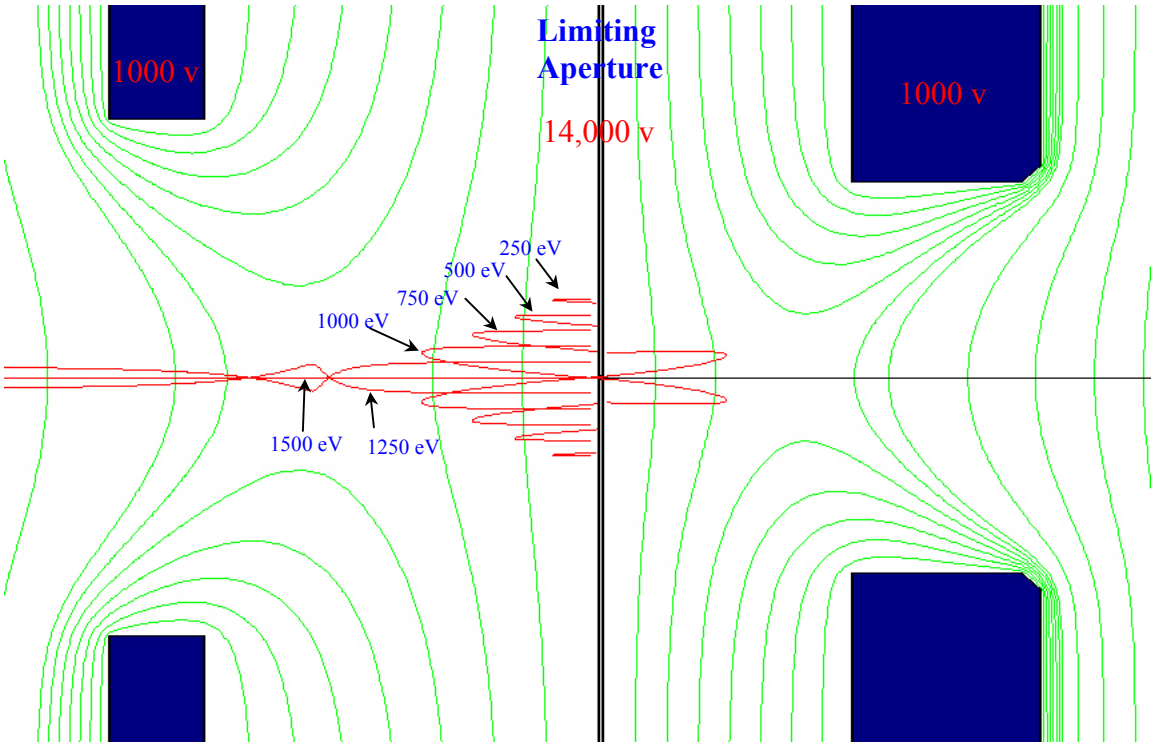

Figure 4.21. A secondary electron trap can be created around the limiting aperture plane by increasing the voltage applied on it.

The effectiveness of the SE trap has been experimentally observed. If there is no charging existing on the pattern generator plane, the ion current passing through the limiting aperture plane will be about 250 pA. The experiment was conducted by measuring the time for the ion current to decrease from 250 pA to 50 pA at different V_a. The charging on the pattern generator plane (including the PCB board) has to be completely neutralized before the next current measurement. This is accomplished by starting the plasma without applying any high voltages to the electrostatic column in MMRL. After ions and electrons drift out from the plasma source. They will only sense the electric field generated by the surface charges on the pattern generator plane. The surface charges attract ions or electrons with opposite charge, so that they will be

completely neutralized. The time for current to decrease from 250 pA to 50 pA has been measured at different V_a, as is listed in table 4-1.

Table 4-1. Time for ion current to decrease from 250 pA to 50 pA at different V_a.

Voltage applied on the limiting aperture (kV)	14	13.5	13	12.5	12.25	12	11.75	11.5	11.25	11.0	10.5
Time for current to decrease from 250 pA to 50 pA (second)	22.5	21.5	16	7	3	1.2	0.7	0.8	1.2	1.7	1.8

Based on the data listed in table 4-1, the current reduction rate has been plotted in fig. 4.22. It is closely correlated to the charge accumulation rate on the pattern generator plane. The charge accumulation rate has a peak at 11.75 kV. It decreases very fast till V_a is increased to 13.0 kV. But the charge accumulation rate can't decrease to zero even after V_a is increased to 14.0 kV. It means that high-energy electron radiation can't be totally eliminated. The remaining electrons could be the SEs generated at the wafer plane. Most of the SEs generated at the wafer plane are blocked by the limiting aperture. But if they can pass through the limiting aperture, the SE trap can't block them because they are generated at the ground potential. Actually, ion beam can ionize the background gas all along the column space if the pressure in the chamber is high. Based on the discussion above, the high-energy secondary electron radiation can be significantly reduced by setting up a trap around the limiting aperture plane, but it can not be totally eliminated.

It is interesting that the charge accumulation rate on the pattern generator plane will decrease when V_a is reduced from 11.75 kV. This is because the focusing condition for SEs is very sensitive to V_a due to the low initial ion energy. Further decreasing V_a will create an accelerating field for SEs generated at the limiting aperture plane.

Simulations show that SEs will be distributed over a larger area if V_a is further decreased from 11.5 kV. This explains why the charge accumulation rate decreases at lower V_a.

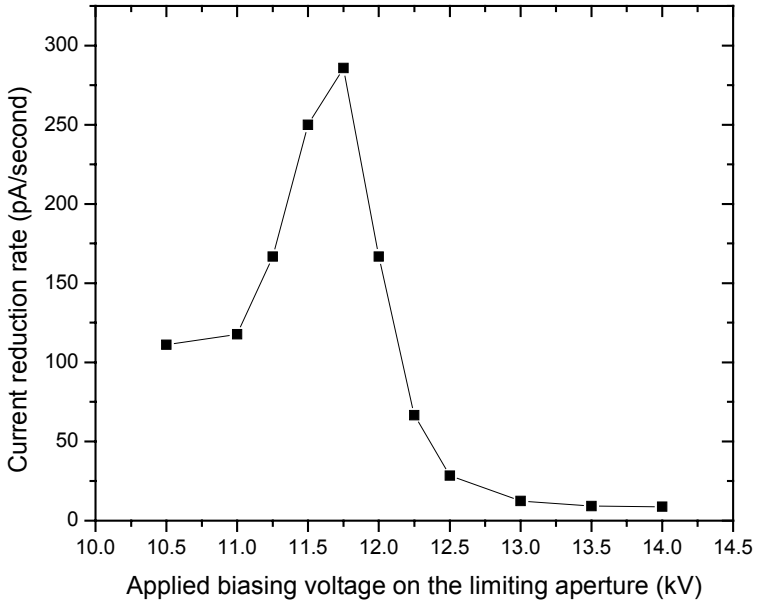

Figure 4.22 Current reduction rate at different voltage applied on the limiting aperture

4.6.2 Suggestions to eliminate surface charging effect

Because of the low accelerating electric field around the mask or the pattern generator plane, any perturbation to it will substantially change the ion beam trajectories and cause the optics to deviate from optimum performance. Thus, the surface of the whole pattern generator assembly should be a flat conductive surface without any exposed insulator. This requires significant changes to the pattern generator chip design and the packaging assembly design.

1) An extra insulating layer and a metal layer should be deposited on top of the pattern generator chip (fig. 4.23), so that all the insulating surfaces on the pattern generator are covered. Actually, the extra metal layer can also help to

reduce the cross-talking effect between the adjacent features, which will be discussed in section 4.8. In order to hold the voltage between the switching electrodes and the two outside metal layers, the thickness of the two insulator layers may both needs to be higher than 10 μm. It might be very challenging to pattern high-aspect-ratio switching apertures through so many layers of materials in the Berkeley Microfabrication laboratory. But it should be doable with the state-of-the-art semiconductor process equipment available nowadays.

2) The pattern generator chip needs to be bonded to the packaging assembly in a way that only conductive surface will be exposed. The metal surface on the packaging assembly should have about the same height as the metal surface on the pattern generator chip in order to form a flat electric field. There must be some insulators between the exposed bonding pads on the pattern generator and between the connections wires on the packaging assembly. All these insulators and the bonding wires must be shielded from the high-energy electrons. These requirements cause a lot of challenges to the pattern generator and the packaging assembly design.

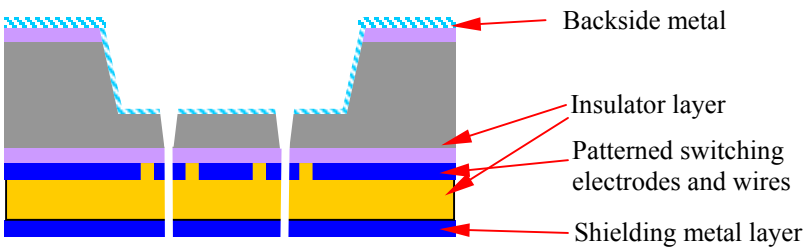

Figure 4.23. Microfabricated pattern generator with shielding metal layer.

4.7 Thermal and structural analysis to the pattern generator

The microfabricated pattern generator will be subjected to a high thermal load during high throughput operation on MMRL. Heat dissipation through the thin membrane of the pattern generator is a very important issue that needs to be addressed, because thermal expansion will cause spatial displacement of the switching apertures, which will result in overlay error on the wafer plane.

Thermal-mechanical simulation to a pattern generator with 40 μm-thick silicon membrane had been performed by Gary A. Frisque and coworkers.[11] Their result predicted very promising thermal-mechanical properties for the pattern generator because of the 40 μm-thick silicon layer, which is over 10 times thicker than the ordinary stencil masks for electron and ion beam projection lithography. The predicted maximum in-plane-distortion caused by fabrication, mounting and gravity is less than 80 nm after a stress-relief area is incorporated into the pattern generator design. With a 10X reduction, the displacement error is 8 nm on the wafer plane. A thermal-structural analysis had also been performed for the pattern generator with an energy density as low as 30 W/m^2. The maximum temperature difference on the pattern generator was predicted to be as low as 0.001 K, which is negligible.

The thickness of the silicon layer was 40 μm in their simulation. High aspect ratio insulating apertures may substantially decrease the extracted ion current. Thus, the thickness of the silicon layer may just be around 10~20 μm in the actual pattern generator design. In order to achieve high brightness ion beams, relatively higher input rf power is required in the MMRL ion source. The actual energy density deposited on the pattern generator will be much higher than 30 W/m^2. For the above reasons, the thermal-

structural properties will be re-evaluated on a pattern generator with a silicon layer of 10 μm thick under a much higher thermal load condition. Corresponding to the pattern generator shown in fig. 4.15, a finite-element model with four layers of materials (100 nm aluminum +10 μm silicon + 1.0 μm Si_3N_4 + 350 nm chromium) will be analyzed with the ANSYS program.

4.7.1 Boundary conditions and thermal load

The pattern generator was fabricated on a silicon wafer of 500 μm thick. The area of the silicon membrane was 2.5×2.5 mm^2. If the peripheral of the pattern generator is sufficiently cooled to maintain room temperature, the boundary conditions for the finite element mesh simulation will be:

1. The temperature at the four corners of the membrane is fixed at room temperature (298 K) because the thick silicon substrate can be treated as an infinitely large heat sink if it is sufficiently cooled.
2. Since the temperature of the silicon substrate will not change during exposure and it is much thicker than the membrane layer, the shape of the substrate should not change. Consequently, the displacements at the edges of the membrane are zero.

The thermal loads to the pattern generator come from three sources: direct thermal radiation from the plasma source, heat flux brought by the ions extracted from the plasma and the high-energy secondary electron radiation to the pattern generator. An rf power of 2000 watt and an ion current density of 100 mA/cm^2 will be used in the simulation. Then the thermal loads are estimated as below:

1. The diameter of the ion source is 26 cm. The length of the source chamber is 30 cm. Assuming that 2000 watt rf power is evenly radiated on all the inner surface of the ion source, the deposited power density will be:

   $2000/(2\cdot Pi\cdot 0.13^2+Pi\cdot 0.26\cdot 0.3)=5694$ watt/m^2

2. If the plasma potential is 10 volt, and a negative 5 volt bias voltage is applied to the plasma-side metal on the pattern generator, the ion energy at the surface of the pattern generator will be 15 eV. Then the energy density deposited by the ions with a current density of 100 mA/cm^2 will be:

   $1\cdot 10^4\cdot 15=15000$ watt/m^2

3. From the data reported by Shu Qin and coworkers,[12] the secondary electron yield induced by helium ion bombardments on a silicon surface is about 8 at an energy of 65 keV. If the ion current collected by the limiting aperture is 100 μA, and assume the secondary electron yield on an aluminum surface is close to that on the silicon surface, then 800 μA secondary electrons with an energy about 65 keV will hit the pattern generator plane. Ray-tracing simulation indicates that the secondary electrons might be distributed over an area with diameter of 10 cm on the pattern generator plane. Then the deposited energy density caused by the high-energy secondary electrons is about 6621 watt/m^2.

Since more than 99% of the secondary electrons have energy lower than 30 eV,[10] it's feasible to eliminate most of the secondary electrons by creating a secondary electron trap at the limiting aperture plane. Consequently, the energy density deposited by the secondary electrons can be reduced to negligibly small amount compared with the thermal load calculated in (1) and (2).

4. If the temperature does not change too much from 298 K, the radiation to the background can be ignored. So only the heat conduction through the edge of the membrane will be considered.

The calculations above are very rough estimations to the thermal load on the pattern generator when MMRL is operated in a high throughput condition. If only the deposited energy densities calculated in (1) and (2) are considered, the total thermal load on the pattern generator plane will be about 20,694 watt/m^2.

4.7.2 Finite element mesh analysis and result

A sequential method has been used for the coupled field (thermal to mechanical) analysis. First, a thermal analysis to the pattern generator was carried out with 20-node 3-D solid thermal elements (Solid90 in ANSYS), which bear a brick shape with 8 nodes on vertexes and 12 nodes in the middle of the edges. After the thermal analysis was finished, the thermal elements were replaced with the corresponding 20-node 3-D solid structure elements (Solid95 in ANSYS). Then the temperature distribution obtained in the first step will be used as the load for the subsequent structural analysis. The reason to choose solid elements instead of shell elements is because of the freedom to change thickness in the

solid elements. 50×50 elements were generated in each membrane layer. Four layers of materials (100 nm aluminum +10 μm silicon + 1.0 μm Si_3N_4 + 350 nm chromium) were built in the finite element model. The switching apertures in the membrane may change its thermal and mechanical properties. But this effect wasn't considered in the simulation because the patterned apertures only occupy a very small fraction of the total area.

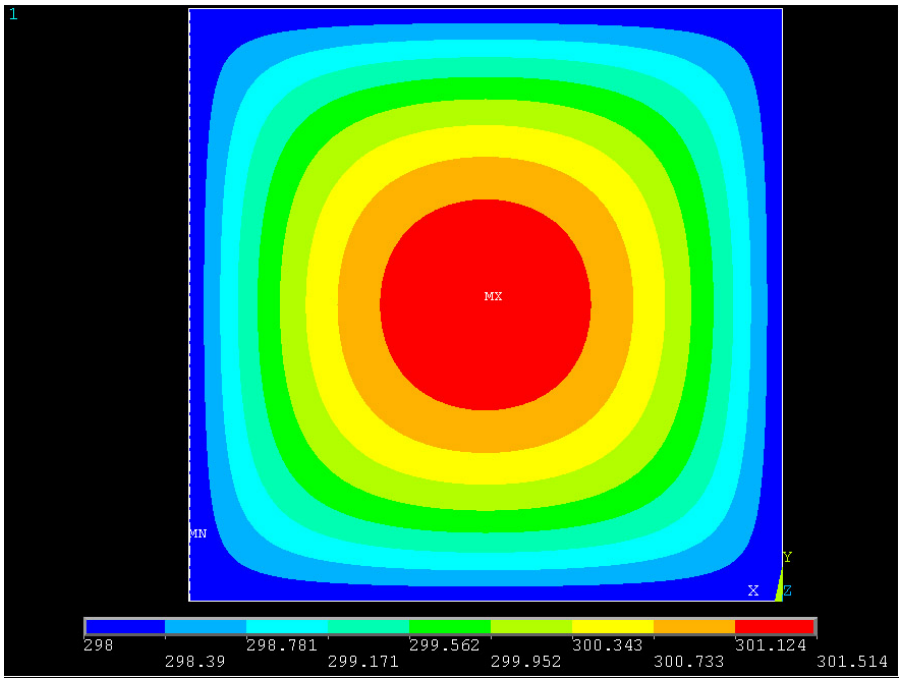

Figure 4.24. Temperature distribution across the surface of the pattern generator

Under a thermal load of 20,694 watt/m^2, the temperature in the center of the pattern generator can be 3.514 ^{0}C higher than that of the boundary, as shown in fig. 4.24. The raised temperature causes spatial displacements in both the X-Y plane and the Z direction, which are simulated in the subsequent structural analysis. The displacements in the X and Y directions are plotted in fig. 4.25 and 4.26. The highest magnitude is about 25 nm at a location close to the edge of the pattern generator. Because of the 10X

reduction on the ion optics column, the displacement on the wafer plane is about 2.5 nm. The required wafer overlay accuracy for the 25 nm lithography node suggested by ITRS is about 4.5 nm. The 3δ CD for 25 nm node is 2.6 nm. The in-plane spatial displacement obtained in the above calculation is acceptable for lithography nodes down to 25 nm. The displacement in the y direction is exactly the same as that in the x direction except being rotated by 90 degree. The displacement in the Z direction has also been calculated in fig. 4.27. The maximum z-axis displacement is about 640 nm at the center of the pattern generator towards to the silicon nitride and the chromium layer. Fortunately, the displacement in the z-axis won't affect the overlay accuracy.

The thermal-structural analysis confirmed that a pattern generator with a silicon membrane layer thicker than 10 μm can be operated reliably with a thermal load of 20,694 watt/m^2, as long as the substrate is sufficiently cooled.

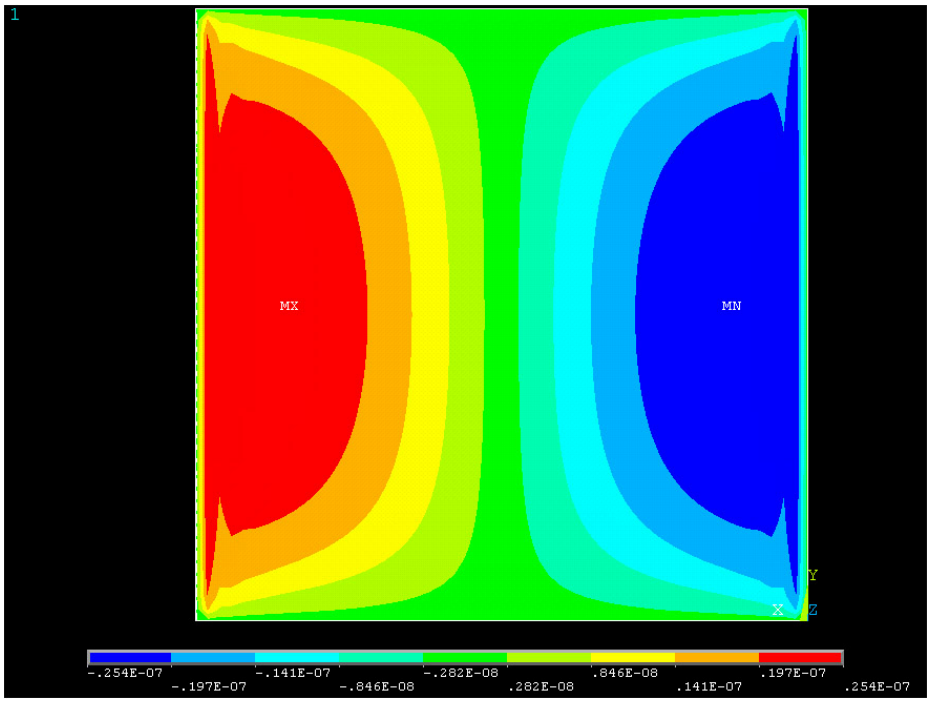

Figure 4.25. Spatial displacement in the X direction

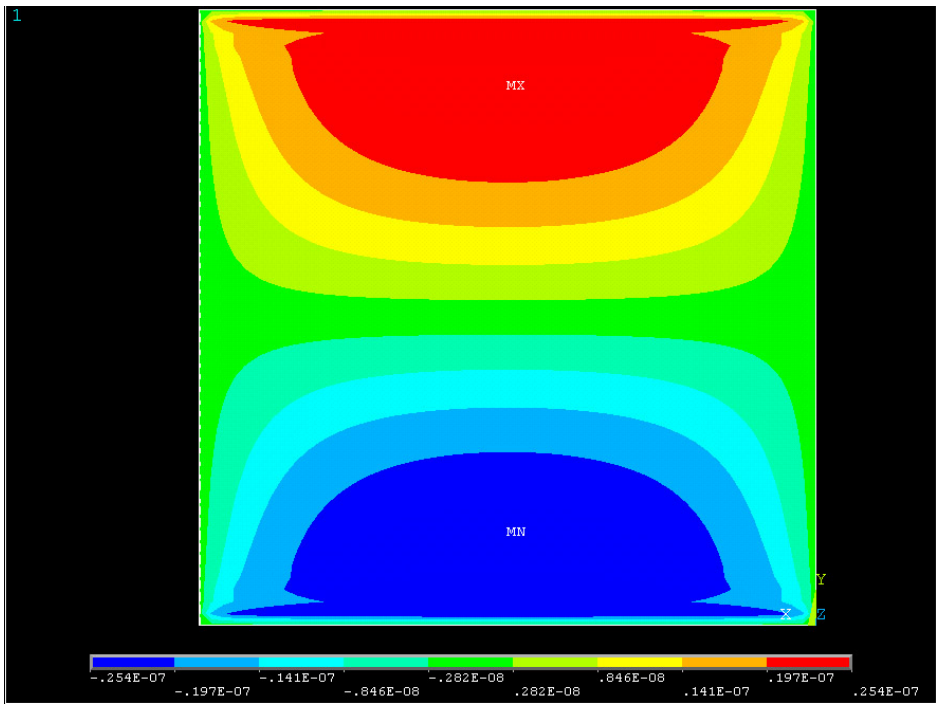

Figure 4.26. Spatial displacement in the Y direction

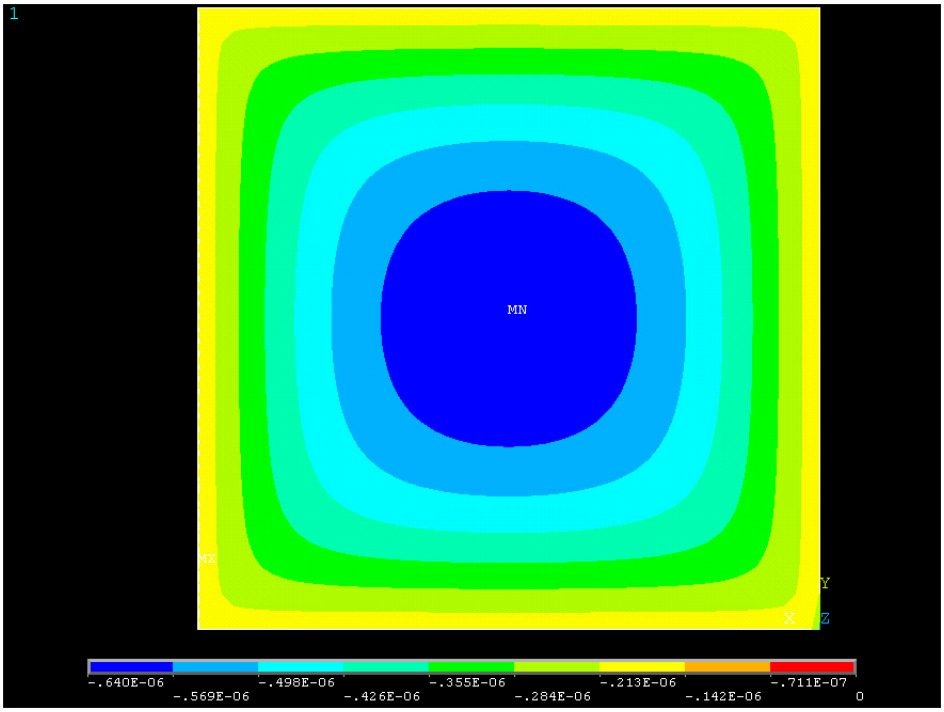

Figure 4.27. Spatial displacement in the Z direction

4.8 Cross-talking issue on microfabricated pattern generators

In order to obtain a high throughput, switching apertures need to be placed as dense as possible in the device layer of the pattern generator. It is predictable that the surface of the pattern generator will be densely packed with biasing pads and interconnecting wires. The incoming low energy ions can be deflected by the electric field generated by the adjacent interconnecting wires, as indicated in fig. 4.28. The simulation was performed with the EO3D package from MEBS^{TM}. It represents a scenario when all the interconnecting wires below the switching electrode are charged to 0 volt and all the wires above are charged to a positive 5 volt. The initial energy of the ions coming out from the plasma sheath is 10 volt. Because of the low initial ion energy and the low axial accelerating electric field (50 volt/mm), ions will be strongly deflected by the electric field generated by the red wires with +5 volt. Deflection happens both inside and outside the aperture. The deflection angle can be as high as 210 mrad even when the red wires are only charged to +5 volt.

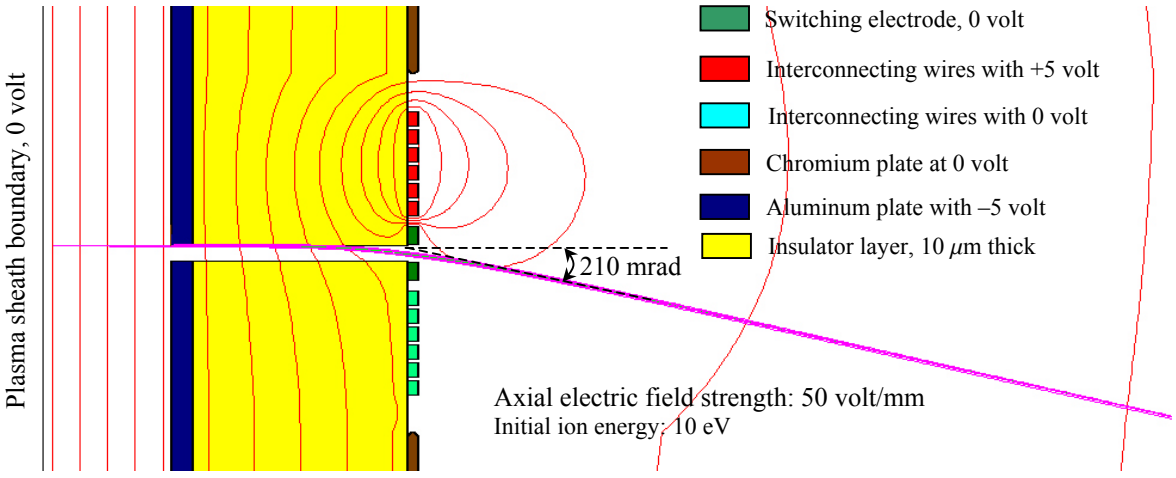

Figure 4.28. Ion beam deflection caused by the voltage applied on the adjacent connecting wires.

In order to reduce the cross-talking effect inside the switching aperture, a new pattern generator design has been proposed, as shown in fig. 4.29. The outer diameter of the switching electrode has been increased from 3.0 μm to 5.0 μm, and the edge has penetrated into the insulator layer by 3.5 μm. Even though the influence from the adjacent red interconnecting wires has been greatly reduced inside the switching aperture, the transverse electric field outside the switching aperture can still create considerable deflection force to the incoming low-energy ion beams.

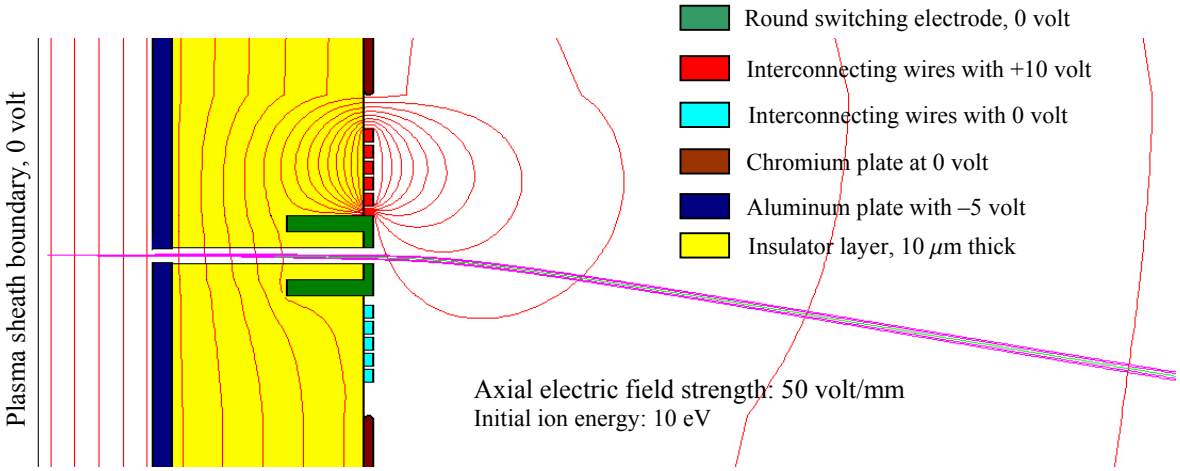

Figure 4.29. Cross-talking inside the aperture has been reduced by increasing the diameter of the biasing pad from 3.0 μm to 5.0 μm and extending it into the insulator layer.

In order to further reduce the influence of the transverse electric field outside the switching aperture, a shielding plate has been added to a pattern generator design shown in fig. 4.30. Actually, the metal shielding layer is also very useful to reduce the surface charging effect induced by the high-energy electron radiations, as has been discussed in section 4.6.2. In order to prevent the arcing between the shielding layer and the switching

layer, the thickness of the insulator layer should be higher than 10 μm. The edge of the switching electrode has been extended by 5.0 μm into the insulation layers on both sides to prevent the electric field generated by the red wires from penetrating into the aperture space. The total deflection angle has been reduced to less than 15 mrad with the new design. It is still possible to further reduce the cross-talking effect by decreasing the switching voltage. However, it will require extensive research on the plasma ion source to reduce the plasma potential.

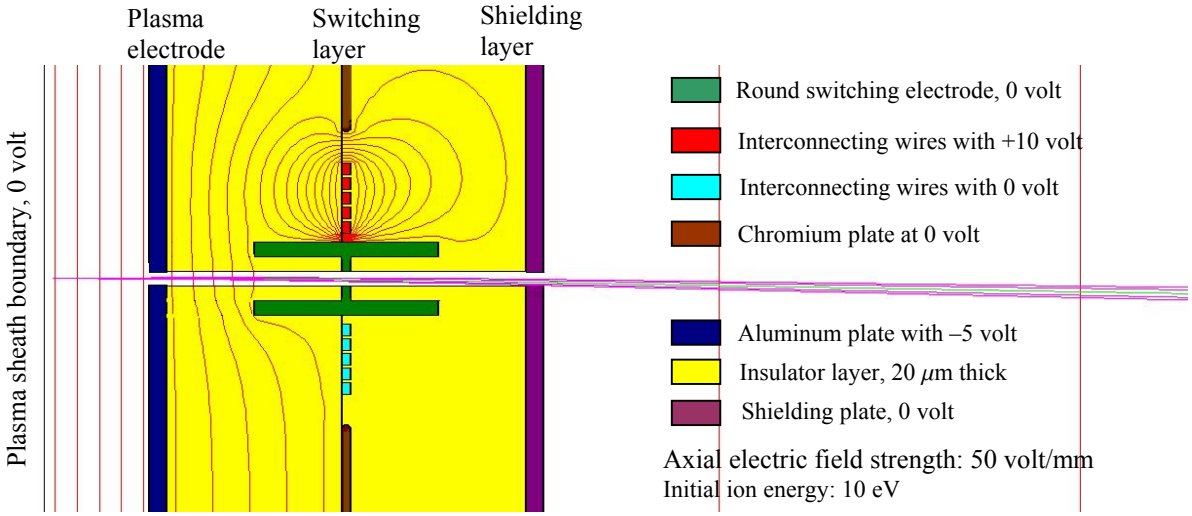

Figure 4.30. The cross-talking effect can be further reduced by adding a shielding metal plate to the pattern generator.

It will be very challenging to fabricate the pattern generator shown in fig. 4.30. The difficulty lies in the high-aspect-ratio metal trench-filling to fabricate the extrusion of the biasing pad and etching of the high-aspect-ratio apertures through the insulator. More simulation work is required to find a pattern generator design that does not only totally eliminate the cross-talking issue but also have a structure that can be feasibly fabricated.

4.9 A new beam-switching scheme to eliminate the surface charging effect

During the development of negative ion sources in the early 1980s, a method to suppress electrons has been developed in the Plasma and Ion Source Technology group of LBL.[13] It utilized a large positively biased electrode to absorb electrons from the plasma around the extraction region. Langmuir probe measurement revealed that the electron current collected by the probe in the extraction region was reduced to a negligible amount if a positive 5 volt is applied to the large aperture electrode. This is understandable because most of the electrons had been absorbed by the large aperture electrode. In the mean time, the positive ion current collected by the Langmuir probe also decreased to about half amount. This result indicated that the positive ion density decreased because of the positively biased aperture electrode. The reduction of the positive ion density was the result of the repulsive force generated by the positively biased aperture electrode and the space charge effect among ions when electrons were extracted out of the plasma. The above observation leads to a question----is it possible to totally shut off the positive ion current when the patterned electrodes around the openings of the apertures in a pattern generator are biased positively while facing a plasma?

As pointed out in section 4.6.2 and 4.8, an extra insulator and metal layer is required to eliminate the surface charging effect on the surface of the pattern generator that faces the ion optics column. But it is actually very difficult to fabricate a pattern generator with the structure shown in fig. 4.30. In order to resolve this problem, a new beam-switching scheme has been proposed, in which the ordinary three-layer pattern generator (fig. 4.3 (a)) is flipped over so that the switching electrodes directly face the

plasma. This idea comes from the experiment of electron suppression for negative ion sources, as discussed in the paragraph above. In order to test this concept as a beam-switching scheme, a mechanically drilled 4-aperture pattern generator (fig. 4.31) has been tested in MMRL.

4.9.1 Structure of the pattern generator and the experimental setup

The diameter of the four mechanically drilled apertures is about 300 μm. They are 9 mm apart from each other. The substrate for the pattern generator consists of two layers of copper (25 μm thick) coated on the both sides of a fiberglass insulator substrate (700 μm thick). The width of the patterned copper wires on the front side is 2 mm. In order to minimize the area of the interconnecting wires from exposing to the plasma, an aluminum cover plate has been placed on top of the pattern generator. There is an opening in the aluminum cover plate so that the apertures and the switching electrodes can be exposed to the plasma.

The switching experiment was performed on the MMRL platform with the setup shown in fig. 4.32. During the experiment, the switching electrodes were biased to a positive voltage. Without any electron confinement, the switching electrodes will extract a lot of electrons from a large plasma volume. In this case, one switching electrode may affect a lot of adjacent apertures. In order to minimize the "influence range" of each switching electrode and to reduce the absorbed electron current, a very strong magnetic field is generated along the surface of the pattern generator to restrain the movement of the electrons.

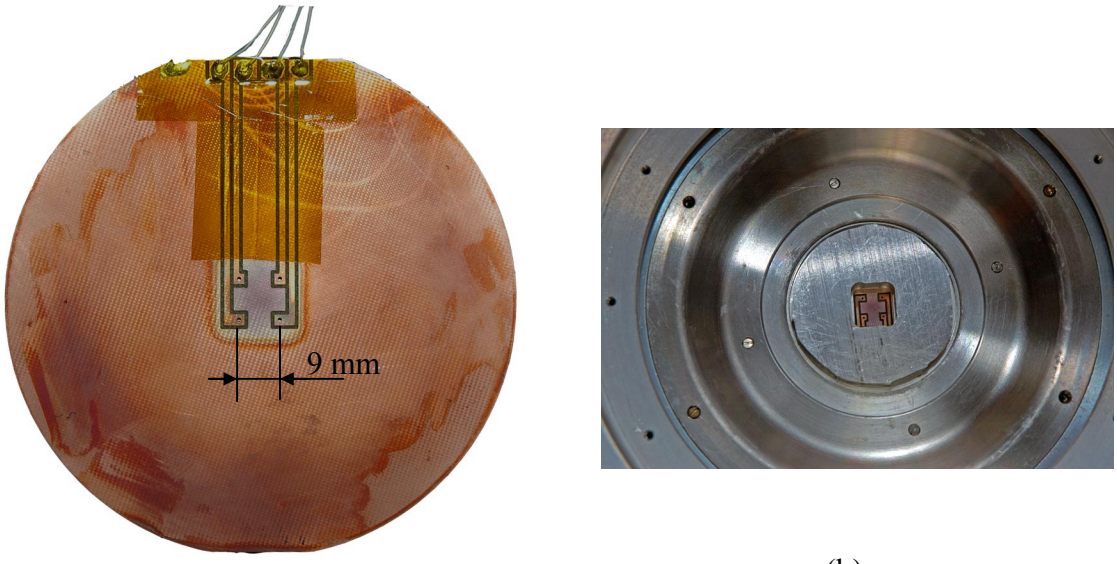

Figure 3.31. (a) Front-side (plasma side) view of the mechanically drilled pattern generator. (b) Only a small window on the pattern generator will be exposed to the plasma after it is installed on MMRL.

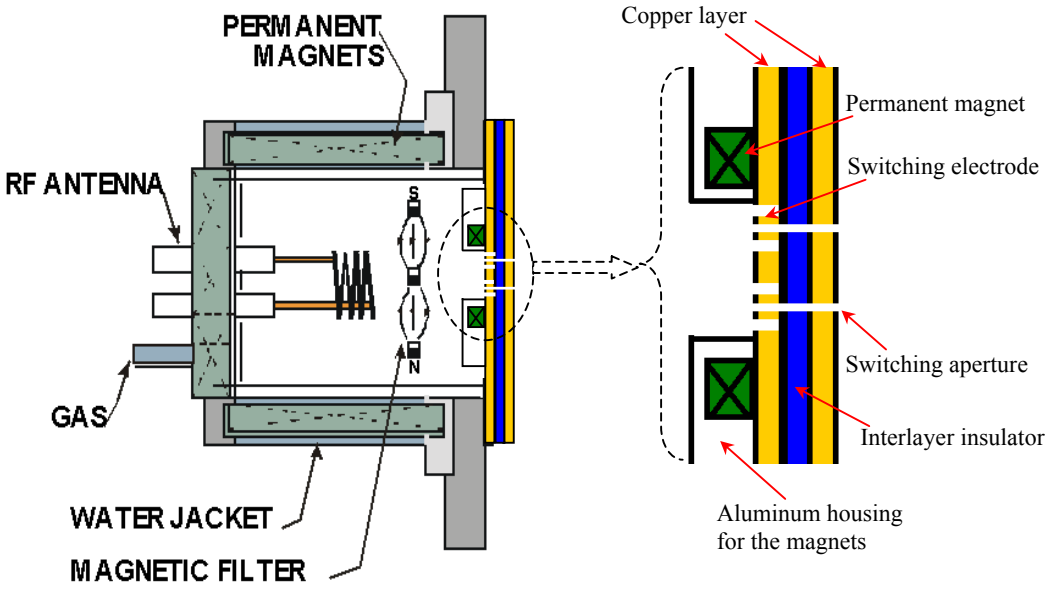

Figure 4.32. Experimental setup for the plasma-side beam switching experiment

4.9.2 Beam switching result obtained with the new operation scheme

Beam switching experiment has been performed with different operation gases. The result is shown in fig. 4.33. The ion currents collected by the Faraday cup have been normalized to the same initial value at zero bias voltage. The normalization ratios have been given in the inserted text label. Difference in the mass of the operation gases may result in different plasma densities and different plasma potentials. Usually, the extracted ion current decreases for ions with relatively high mass. The extracted ion current for krypton is about 5 times lower than that of helium under the same condition (fig. 4.33).

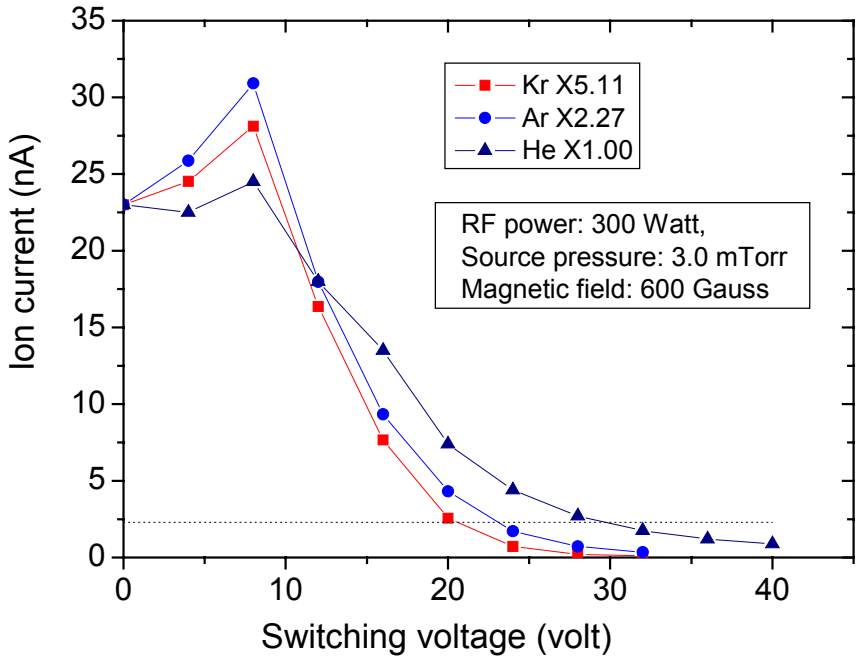

Figure 4.33. Ion current collected by the Faraday cup versus the switching voltage for different operation gases. Dashed line represents 10% of the initial ion current

Ion beam switching result in fig. 4.33 indicates that heavier ions can be switched off with a slightly lower bias voltage. In order to reduce the current to 10% of the initial value, a positive bias voltage of 20 volt is required for krypton, but that for argon is about 24 volt, and 31 volt is required for helium. The electron current collected by the switching electrodes in an argon or krypton plasma is also lower than a helium plasma (fig. 4.34). Due to the strong magnetic field around the surface of the pattern generator, the collected electron current will saturate at amount of 1~2 mA (fig. 4.34).

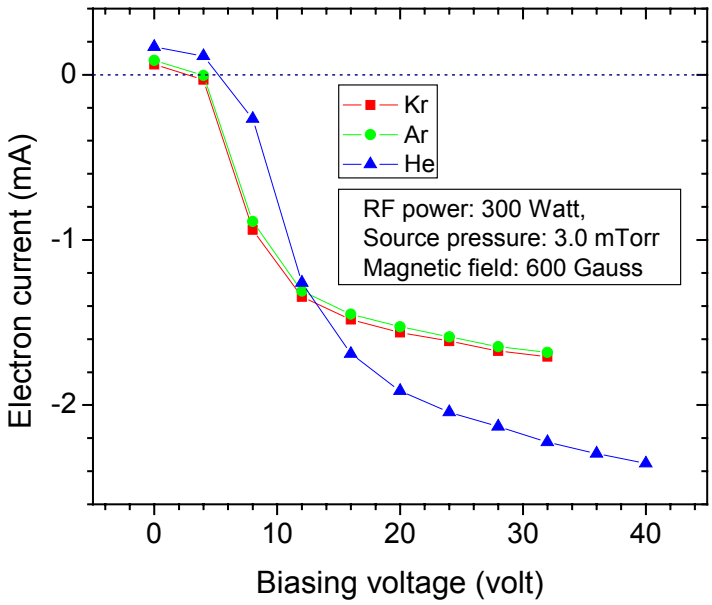

Figure 4.34. Electron current collected on all the switching electrodes.

It's easy to understand that the input rf power can affect the plasma density. The required switch-OFF voltage (reducing the current to 10%) can change from 22 volt to 32 volt when the rf power is increased from 100 watt to 500 watt (figure 4.35).

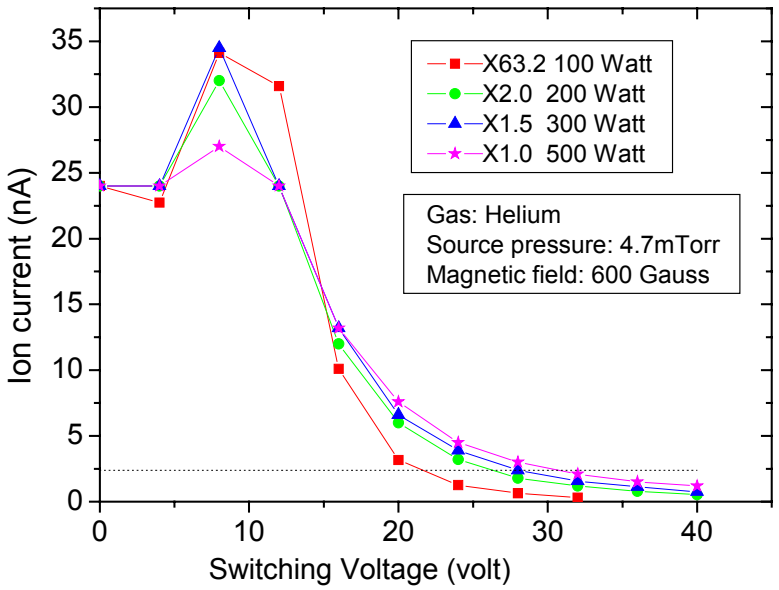

Figure 4.35. Ion current switching curves for different input rf power.

In order to successfully switch off the ion current, electron density around the aperture has to be sufficiently reduced. Without a strong magnetic field on the surface of the pattern generator, electrons far away from the apertures can be extracted toward the positively biased switching electrodes. Experimental result in fig. 4.36 shows that the electron current collected by the switching electrodes can be doubled when the magnetic field is decreased from 600 gauss to 300 gauss. It results in a high switching voltage at a low magnetic field, as shown in fig. 4.37. The switching voltage has increased from 29 volt to 37 volt when the magnetic field is decreased.

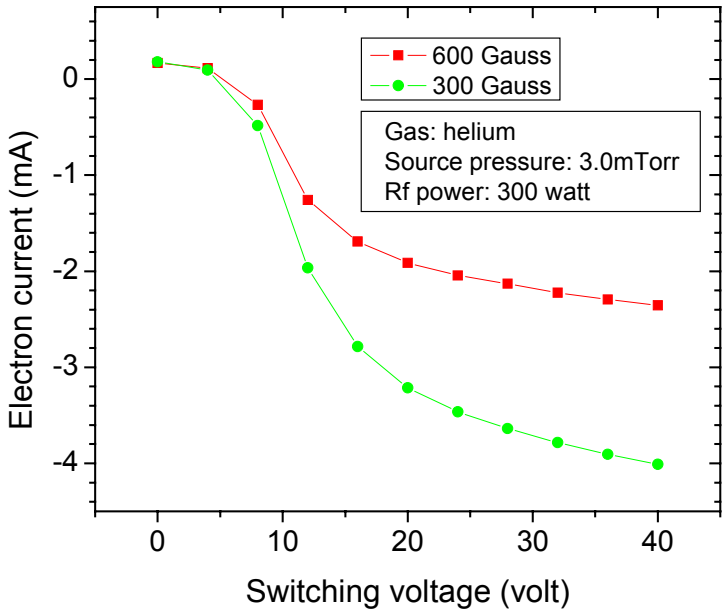

Figure 4.36. Electron current extracted by the switching electrodes under different magnetic field.

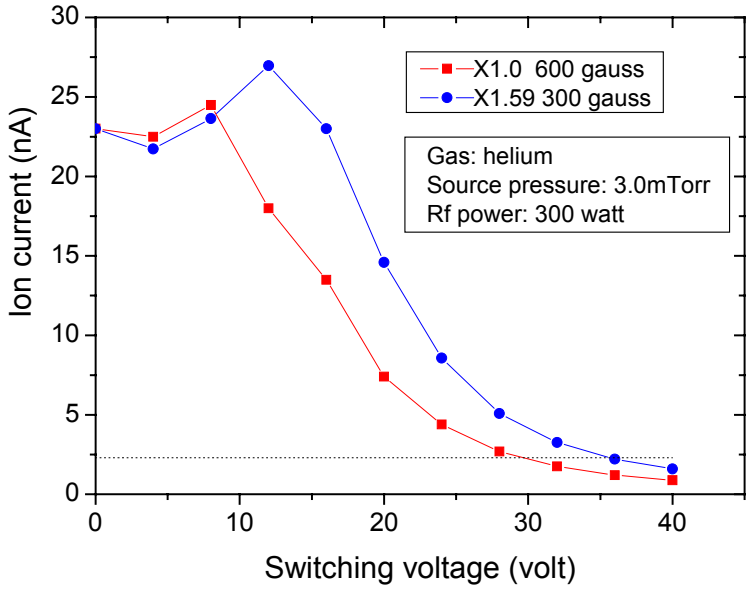

Figure 4.37. Ion current switching curves for different magnetic field.

The neutral gas pressure inside the ion source can change the plasma density, the plasma potential and the electron temperature. Experimental result in fig. 4.38 shows that

a high neutral gas pressure can effectively lower the switching voltage. When the pressure is increased from 3.0 mTorr to 11.7 mTorr, the switching voltage is decreased from 37 volt to 24 volt. In order to explain this result, we have to refer to one of the most important properties of plasma, Debye shielding, which states that plasma can shield out electric fields. The "screening distance", a distance where the electrostatic potential is decreased to e^{-1} due to Debye shielding compared with the potential when plasma does not exist, is measured by Debye length, which is defined as:

$$\lambda_D = \sqrt{\frac{\varepsilon_0 k T_e}{2 n_e e^2}} \tag{4-1}$$

It is very obvious that Debye length decreases with the electron temperature. A high gas pressure in the ion source can effectively cool down the electrons. The Debye length is smaller when the source pressure is increased. Therefore, the bias voltage on the switching electrodes can be screened within a relatively shorter range at higher source operation pressure. Then the required switching voltage will decrease.

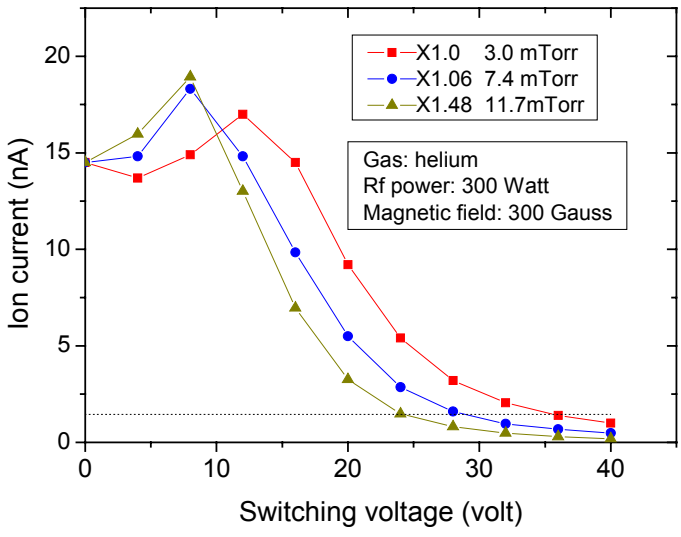

Figure 4.38. Ion current switching curves for different neutral gas pressure.

The pitch distance of the four apertures in the mechanically drilled pattern generator is about 9 mm. When two of the apertures are maintained at the ground potential, and the other two are charged to a positive bias voltage of 40 volt, the ion current decreases to half the value when all the apertures are ON. This means that the "influence range" of the switching electrodes is not long enough to affect the adjacent switching apertures in the present experiment due to the long pitch distance (9 mm) and the high magnetic field.

4.9.3 Discussion and conclusion on plasma-side ion beam switching design

Plasma-side ion beam switching has been successfully demonstrated with a mechanically drilled pattern generator shown in fig. 4.31. Ion current can be successfully decreased to 10% with a 20~30 volt positive bias voltage applied on the switching electrodes. The influence of rf power, ion mass, magnetic field strength and neutral gas pressure has been experimentally investigated. The experimental results show that each ion beamlet can be switched off independently when the pitch distance of the apertures is 9 mm.

The new operation scheme can eliminate the charging problem on the surface of the pattern generator facing the ion optics column. But there are several remaining issues that need to be investigated.

1. Cross-talking problem hasn't been resolved. Positively biased connection wires can still deflect ion beams at the plasma-side surface of the pattern generator and inside the aperture. Actually, the switching voltage in the new operation scheme is higher than that of the normal operation scheme, which will worsen the cross-

talking effect. The switching voltage must be lowered through more investigations.

2. The new operation scheme relies on positively biased electrodes to extract electrons out of the plasma. When the size of the switching electrode decreases, it may require even higher positive voltage to sufficiently decrease the density of the electrons. The switching voltage may increase when the switching electrodes are scaled down to microns range.
3. The influence range of a switching electrode might reach several adjacent densely packed apertures in a microfabricated pattern generator. As a result, a positively biased switching electrode may decrease or switch off the ion current of the neighboring apertures. The Lamor radius of a 5.0-eV electron in a 600-gauss magnetic field is about 125 μm. It indicates that a magnetic field with strength of 600 gauss is still not strong enough to confine electrons in a range of tens of micron. Thus, a positively biased electrode can extract electrons from the plasma volume of several hundred microns away.

   The influence range of the switching electrode can be decreased by adding an extra shielding electrode outside the switching electrode.[14] The shield electrode is patterned in the same metal layer as the switching electrode. It should be extended in the perpendicular direction, so that it is taller than the switching electrode in order to obtain a good shielding effect. The shielding electrode is maintained at ground potential.
4. The new operation scheme relies on a high magnetic field to confine the electrons. But a strong magnetic field will deflect the incoming low-energy ions. This will

cause a beam shift on the wafer plane and increase the image aberrations. The filter magnetic field should be optimized so that there is no much magnetic field existing on the ion optical column side of the pattern generator.[15]

Even though there may exist several potential problems for the new operation scheme, it can eliminate the surface charging effect. The successful demonstration of ion beam switching indicates that it is a very promising technique for the development of the future pattern generators.

Reference:

[1] T. H. P. Chang, "Instrumentation for electron-beam lithography", IEEE Transactions on Magnetics **MA10** (3), 883 (1974); H. C. Pfeiffer, "Variable spot shaping for electron-beam lithography", Journal of vacuum Science and Technology **15** (3), 887 (1978).

[2] Hans C Pfeiffer, "The history and potential of maskless e-beam lithography", Microlithography World **14** (1) (2005).

[3] Akio Yarnada, "Advantest's EBDW System; MCC System with CP" presented at the Proceeding of the maskless lithography workshop by SEMATECH international (January 17th~19th, 2005).

[4] Fabian Pease, Daniel Pickard, and Zhi Liu, "Charged particle maskless lithography (CPML2)" presented at the Proceeding of the maskless lithography workshop by SEMATECH international (January 17th~19th 2005).

[5] S. T. Coyle, B. Shamoun, M. Yu et al., "Progress toward a raster multibeam lithography tool", Journal of vacuum Science and Technology B **22** (2), 501 (2004).

[6] Bert Jan Kampherbeek and Guido de Boer,"MAPPER: High throughput maskless lithography" presented at the Proceeding of the maskless lithography workshop by SEMATECH international (January 17th~19th 2005).

[7] Christoph Brandstätter and Hans-Joachim Döring, "Projection Maskless Lithography (PML2) Technology - Results" presented at the Proceeding of the maskless lithography workshop by SEMATECH international (January 17th~19th, 2005).

[8] Y. Lee, W. A. Barletta, K. N. Leung et al., "Multi-aperture extraction system with micro-beamlet swtiching capability", Nuclear Instruments and Methods in Physics Research A **474**, 86 (2001).

[9] V.V. Ngo, "Experimental demonstration of a Prototype Maskless Micro-ion-beam Reduction Lithography System", Ph.D. Thesis, University of California 2005.

[10] S. Y. Lai, D. Briggs, A. Brown et al., "The relationship between electron and ion induced secondary electron imaging: A review with new experimental observations", Surface and interface analysis **8**, 93 (1985).

[11] Gary A. Frisque, Po-Tung Lee, Edward G. Lovell et al., "Thermalmechanical simulations for micro-beam reduction lithography" presented at the Emerging Lithographic Technologies IV, Proceedings of SPIE,3997,578(2000).

[12] Shu Qin, Michael P. Bradley, Peter L. Kellerman et al., "Measurements of secondary electron emission and plasma density enhancement for plasma exposed surfaces using an optically isolated Faraday cup", Review of Scientific Instruments **73** (3), 1153 (2002).

[13] K.W. Ehlers and K. N. Leung, "Electron suppression in a multicusp negative ion source", Applied Physics Letter **38** (4), 287 (1980).

[14] L. L. Ji, "The reduction of the influence range of switching electrodes on a one-layer pattern generator design", Private communication (2003).

[15] K.W. Ehlers and K. N. Leung, "Increasing the efficiency of a multicusp ion source", Review of Scientific Instruments **53** (9), 1429 (1982).

Chapter 5

Summary

The work described in this thesis can be classified into two major categories, as discussed in Chapter 3 and Chapter 4 respectively. Chapter 3 focused on optics analysis. Ion optics does not only determine the image resolution, but also limits the throughput. With the improvement of the ion optical system for MMRL, features as small as 50 nm have been resolved. In addition, challenges and possible solutions to improve the throughput of MMRL have been discussed.

Chapter 4 concentrated on the development of the micro-fabricated pattern generators. Ion beamlet switching has been successfully demonstrated on the MMRL system. But some unexpected issues were also discovered, such as the high-energy secondary electron radiations. Thermal and structural analysis to the pattern generator showed a very optimizing result. But the 3-D ray-tracing simulation around the pattern generator plane revealed that the cross-talking effect might be a very important issue that needs more investigations. In order to eliminate the surface charging effect caused by the secondary electrons, the concept of a new beam-switching scheme, in which the switching electrodes are immersed in the plasma, has been demonstrated on a mechanically fabricated pattern generator.

5.1 Achievements

5.1.1 Resolution improvement

The entire optical system on MMRL has been re-evaluated using the MEBS^{TM} optics design software. The discrepancy between the simulation and the experimental results obtained by Vinh V. Ngo has been successfully explained by the incorrect initial ion energy and the beam half angle used in his simulation. Based on the new simulation result, a limiting aperture has been incorporated into the ion optical column to reduce the beam half angle, which successfully improved the resolution to below 200 nm. The design of the limiting aperture was further optimized by creating a field-free region to reduce the aperture-induced aberrations. With the employment of the field-free limiting aperture, the reduction of the electromagnetic interference and cleaning of the ion source, features as small as 50 nm can be readily observed.

5.1.2 Throughput analysis

Ion optics does not only determine the image quality, but also affects the throughput. Based on the new simulation result, optimum operation parameters such as the field size and the beam half angle have been determined to attain the highest throughput on the current MMRL system. In addition, the spatial displacement effect caused by ion-ion interactions has been studied based on a simple physics model. The equation obtained in the present work agrees surprisingly well with the results published by other research groups. Based on these studies, the maximum allowable current on MMRL has been evaluated. Suggestions to reduce the charge interactions have also been

presented. Besides the ion optics, the mechanical stage can also limit the throughput. The requirement of the high precision mechanical stage has been briefly studied for different maskless lithography modes. It shows that the exposure field size and the ion current must be increased in order to obtain a throughput higher than 10 wafers per hour on the MMRL tool.

5.1.3 Demonstration of ion beamlet switching on the MMRL tool with micro-fabricated pattern generators

In order to perform maskless lithography, a micro-fabricated pattern generator is required. Three versions of micro-fabricated pattern generators have been developed in the current thesis work. Each new version was improved based on the experimental observations on the previous one. Ion-beamlet switching has been successfully demonstrated on the MMRL ion source with 10~13 volts of positive bias voltage on the third version of micro-fabricated pattern generator. Some unexpected problems have also been discovered during the experiments, such as the high-energy electron radiation and the surface charging issue on the insulating surfaces.

5.1.4 Thermal and structural analysis for the pattern generator

During the high throughput operation on MMRL, a lot of energy will be deposited on the micro-fabricated pattern generator. A finite-element-mesh simulation has been carried out in ANSYS to investigate the deformation of the pattern generator under a thermal load of 20,694 watt/m^2. The simulation result indicated that the aperture

displacement errors induced by the thermal expansion satisfy the overlay accuracy and the 3δ CD suggested by the ITRS 2005 for lithography nodes down to 25 nm.

5.1.5 Analysis of the cross-talking issue on the pattern generator

The development of the pattern generator will eventually face another problem---the cross-talking issue along the surface and inside the apertures of the micro-fabricated pattern generator. Cross-talking is generated because the bias voltage applied on the connection wires can affect the trajectory of the adjacent ion beamlets. Besides the closely packed connection wires and the thick insulating layer in the pattern generator, the high switching voltage, the low initial ion energy and the low axial accelerating electric field also contribute to the cross-talking problem. This issue has been studied with simulations performed on a 3-D ray-tracing simulation software. Improvement to the pattern generator design has been discussed in order to reduce the cross-talking effect.

5.1.6 Demonstration of the plasma-side beam-switching concept with a mechanically fabricated pattern generator

In order to eliminate the surface charging effect on the surface of the pattern generator facing the ion optical column, a plasma-side beam-switching scheme has been investigated on the MMRL tool with a mechanically fabricated pattern generator. The new scheme has been successfully tested under different operation conditions. Usually, a switching voltage of higher than 20 volts is required in the experimental setups that have

been investigated. Even though there may exist other possible problems in this kind of operation scheme, it does provide a possible solution for the development of future pattern generators.

5.2 Suggestions to the next phase development of MMRL

Since ITRS has lower the insertion point of the maskless lithography to below 45 nm, it is still requisite to continuously improve the resolution of the MMRL. Further improvement can be achieved by lowering the ripple of the high voltage supplies, decreasing the energy spread of the ion beams, reducing the rf interference and shielding the AC/DC magnetic field. Besides the resolution, the throughput must be increased by raising the maximum allowable ion current and adopting a large-field ion optical column.

Based on the discovered concerns during the development of micro-fabricated pattern generators, more experimental and simulation work is required to find a pattern generator design that can survive high-energy electron radiations, eliminate the surface charging effect and totally resolve the cross-talking problem. In addition, the micro-fabrication process has to be compatible with the fabrication equipments available nowadays. Because of the tight requirement on the data rate, the switching speed has to be investigated. Closely packed long connection wires in the micro-fabricated pattern generator might be a hurdle to achieve a high switching speed. Ion beam transportation through the high-aspect-ratio apertures is also an important topic that needs to be addressed with more experimental research.